

RESONANT AND CONTINUUM PRODUCTION  
OF MASSIVE MUON PAIRS  
IN 400 GeV PROTON-NUCLEUS COLLISIONS

A Dissertation Presented

by

Daniel Moshe Kaplan

to

The Graduate School

in Partial Fulfillment of the Requirements

for the Degree of

Doctor of Philosophy

in

Physics

State University of New York

at

Stony Brook

May, 1979

STATE UNIVERSITY OF NEW YORK

AT STONY BROOK


THE GRADUATE SCHOOL


DANIEL MOSHE KAPLAN

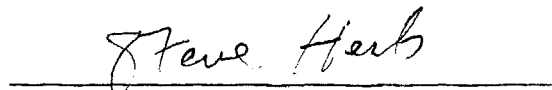
---


We, the dissertation committee for the above candidate for the PhD degree, hereby recommend acceptance of the dissertation.

  
J. Doll

  
M. Dresden

  
A. Goldhaber

  
S. Herb

  
H. Jöstlein

The dissertation is accepted by the Graduate School.

---

J. Bigeleisen, Dean

December, 1978

## ABSTRACT

An experiment to measure the yield of muon pairs above 5 GeV mass in 400 GeV proton-nucleus collisions is described in detail. Apparatus used, running conditions, backgrounds and corrections to the data are discussed. Results are presented and interpreted in terms of the quark-parton model and quantum chromodynamics (QCD). The production of a new family of narrow  $\mu^+ \mu^-$  resonances, dubbed T, is observed. Dependence of the muon-pair cross-section on nucleon number, mass, transverse momentum, and rapidity is presented, and differences in the production dynamics of the resonances and the continuum are emphasized. Various possible interpretations of the T are discussed, and the most likely one - that the T's are bound states of a new, heavy, charge - 1/3 quark with its antiquark - is elucidated. The continuum is interpreted in terms of the parton annihilation model of Drell and Yan modified by QCD corrections. Momentum distributions of antiquarks in the nucleon are extracted. The problem of large muon pair transverse momentum is discussed. The spectrum of single muons arising from massive muon-pair production is computed.

"The road to Hell wasn't built in a day."

(From the Collected Wisdom of Harvey Nanosecond)

## Table of Contents

	Page
Abstract . . . . .	iii
Dedication Page . . . . .	iv
Table of Contents . . . . .	v
List of Figures . . . . .	viii
List of Tables . . . . .	x
Acknowledgements . . . . .	xi
I. Introduction . . . . .	1
A. Continuum . . . . .	1
B. Resonances . . . . .	11
II. Experimental Apparatus . . . . .	13
A. Design Criteria . . . . .	13
B. Apparatus Overview . . . . .	15
C. Detailed Description . . . . .	19
1. Beam line . . . . .	19
2. Target box . . . . .	20
3. Targets . . . . .	20
4. Beam dump . . . . .	22
5. Targeting monitors . . . . .	22
6. Hadron absorber . . . . .	24
7. Shielding wall . . . . .	25
8. Air gap magnets . . . . .	25
9. Detectors . . . . .	27
10. Steel magnets . . . . .	29
11. More detectors . . . . .	32
D. Resolution . . . . .	33
1. Multiple scattering momentum error . . . . .	35
2. MWPC momentum error . . . . .	37
3. Multiple scattering horizontal angle error . . . . .	41

4. MWPC horizontal angle error . . . . .	41
5. Constrained fit to horizontal angle . . . . .	42
6. Calculated mass resolution . . . . .	45
7. Mass resolution from data . . . . .	46
III. Data Acquisition . . . . .	50
A. Fast Trigger Logic . . . . .	50
B. DC Logic . . . . .	53
C. Readout System . . . . .	58
D. Computer and On-Line Program . . . . .	60
E. Data Taking . . . . .	62
IV. Data Reduction . . . . .	65
V. Results . . . . .	71
A. Backgrounds . . . . .	71
B. Normalization . . . . .	83
1. SEM calibration . . . . .	85
2. A-dependence . . . . .	85
3. Efficiency . . . . .	93
4. Acceptance . . . . .	108
C. Mass Spectra and Resonant Structure . . . . .	118
D. Transverse Momentum and Rapidity Spectra . . . . .	127
E. Further Corrections to the Cross-section . . . . .	130
1. Nucleon motion . . . . .	130
2. Radiative corrections . . . . .	135
3. T acceptance . . . . .	135
F. Estimate of Systematic Errors . . . . .	138
VI. Discussion and Conclusions . . . . .	145
A. Nature of the T's . . . . .	145
1. Are they conventional vector mesons? . . . . .	145
2. Is it the Z? . . . . .	145
3. Is it the Higgs? . . . . .	146
4. Quarkonium . . . . .	148
B. Nature of the Continuum: The Parton Model . . . . .	155

1. The naive parton model . . . . .	155
2. QCD corrections . . . . .	157
3. Extraction of sea x distributions . . . . .	159
4. Rapidity slopes . . . . .	161
5. Transverse momentum . . . . .	162
6. Quark-meson scattering . . . . .	163
C. Lepton Pairs and Single Leptons . . . . .	163
D. Summary of Conclusions . . . . .	164
Appendix: Mass Calibration	
A. Alignment . . . . .	167
B. Magnet Calibration . . . . .	167
C. Energy Loss . . . . .	168
D. Observed Masses and Calibration Adjustment . . . . .	169
References . . . . .	170

## List of Figures

Figure	Page
1    Lepton pair production . . . . .	2
2    Deep inelastic lepton-nucleon scattering . . . . .	4
3    Parton model of deep inelastic scattering . . . . .	5
4    Parton-antiparton annihilation . . . . .	6
5    One-gluon processes . . . . .	9
6    Meson-quark scattering . . . . .	10
7    Plan view of apparatus . . . . .	16
8    Target box plan and elevation . . . . .	21
9    Steel magnet . . . . .	30
10   Effect of scattering in $dz$ of absorber . . . . .	36
11   Mass resolution and its components vs. mass . . . . .	47
12   Mass distributions from low current runs . . . . .	48
13   Block diagram of data acquisition system . . . . .	51
14   Fast trigger logic . . . . .	52
15   DC logic . . . . .	54
16   Muon criteria confidence level - $5 \text{ GeV} < m < 7 \text{ GeV}$ . . .	72
17   Muon criteria confidence level - $7 \text{ GeV} < m < 9 \text{ GeV}$ . . .	73
18   Muon criteria confidence level - $m > 9 \text{ GeV}$ . . . . .	74
19   Confidence level vs. MM deviation . . . . .	77
20   Mass distributions at 1500A . . . . .	80
21   Effect of reflection on mass and $p_t$ distributions . . . .	84
22   Target scans . . . . .	90
23   Platinum target scan and estimated bead contribution . .	92
24a   The power $\alpha$ of the A-dependence vs. mass . . . . .	96
24b   The power $\alpha$ of the A-dependence vs. $p_t$ . . . . .	97
25 $90^\circ$ monitor/SEM ratio during the A-dependence running . .	98
26   Horizontal angle distributions in the two arms . . . . .	106
27   Acceptance vs. mass . . . . .	109
28   Acceptance vs. $p_t$ . . . . .	110
29   Acceptance vs. rapidity . . . . .	111



30	Acceptance vs. beam axis decay cosine . . . . .	112
31	Definition of the decay angle $\theta^*$ . . . . .	115
32	Ratios of data event distributions to Monte Carlo event distributions . . . . .	117
33	Differential cross-section per nucleus vs. mass . . . . .	119
34	Differential cross-section per nucleon vs. mass . . . . .	121
35	Continuum-subtracted cross-section in the enhancement region and two- and three-resonance fits . . . . .	123
36	Mass resolution shape without and with radiative correction . . . . .	124
37	Invariant cross-section vs. $p_t$ . . . . .	128
38	$\langle p_t \rangle$ and $\langle p_t^2 \rangle$ vs. mass . . . . .	129
39	Differential cross-section vs. rapidity . . . . .	131
40	Relative rapidity slope vs. mass . . . . .	132
41	Continuum-subtracted cross-section in the enhancement region vs. $p_t$ . . . . .	137
42	Differential cross-section per nucleon vs. mass . . . . .	139
43	Asymmetry vs. mass . . . . .	147
44	Examples of quarkonium decays . . . . .	149
45	Quark-quark scattering . . . . .	158
46	Direct leptons from lepton pairs . . . . .	165

# List of Tables

Table		Page
I	Target Properties . . . . .	23
II	Detectors . . . . .	28
III	Hadron Absorber Configuration . . . . .	38
IV	Effective Chamber Configuration . . . . .	40
V	$J/\psi$ Resolution . . . . .	49
VI	1500A Data Sets . . . . .	64
VII	Fiducial Cuts . . . . .	67
VIII	Sample Selection Requirements . . . . .	69
IX	Levels of Compression . . . . .	70
X	Effect of Successive Cuts on Number of Events . . . . .	76
XI	A-dependence Flux Calculation . . . . .	89
XIIa	A-dependence vs. mass . . . . .	94
XIIb	A-dependence vs. $p_t$ . . . . .	95
XIII	Trigger Efficiencies . . . . .	100
XIV	Compression Efficiencies . . . . .	101
XV	Reconstruction Efficiencies . . . . .	102
XVI	Muon Cut Efficiencies . . . . .	103
XVII	Efficiency Summary . . . . .	105
XVIII	Hodoscope Efficiency Corrections . . . . .	107
XIX	Resonance Plus Continuum Fits . . . . .	126
XX	Nucleon Motion Correction Parameters . . . . .	134
XXI	Differential Cross-section vs. Mass . . . . .	140
XXII	Resonance Plus Continuum Fits . . . . .	143

## ACKNOWLEDGEMENTS

A modern high energy physics experiment is such a complex undertaking that no one person can take responsibility for its success. Every member of the Columbia-Fermilab-Stony Brook Collaboration made his own important contribution, as did also the many engineers and technicians who participated. I want to thank in particular Drs. Steve Herb, Dave Hom, Walt Innes, and Al Ito for very many useful discussions and because they were friends and companions as well as colleagues. My advisor, Professor Hans Jöstlein, made many helpful comments and suggestions. The accidentals reflection procedure of Section V.A is due to Dr. John Rutherford of the University of Washington. And, of course, the whole idea for the experiment is due to Professor Leon Lederman.

I must also thank Emilie Luisada and Charles Wrigley who executed the figures and Jo Ann Acevedo who typed the final draft and took a considerable load off my mind by seeing to the many details involved in attending a university from a distance of 900 miles.

I want to thank my parents and my teachers, who encouraged me in the study of science.

And finally, I thank Gene Lloyd, Nancy Roth, and Suzanne Gronemeyer, who helped me to partake of the joy and the solace of chamber music.



## I. INTRODUCTION

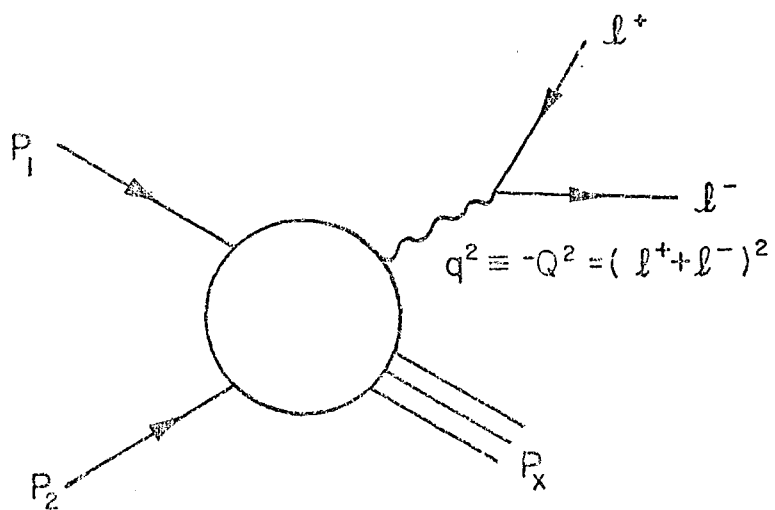
This thesis describes an experiment performed in Fermilab's Proton Center laboratory to measure the inclusive production of massive muon pairs in 400 GeV proton-nucleus collisions:

$$p + N \rightarrow \mu^+ + \mu^- + \text{anything.}$$

The experiment was carried out in 1977 by a Columbia-Fermilab-Stony Brook (CFS) collaboration<sup>1</sup>. The first such muon-pair experiment, done in 1969 at Brookhaven, revealed a continuous spectrum of muon pairs falling off rapidly with increasing mass<sup>2</sup>, and led Drell and Yan to propose their parton-antiparton annihilation model<sup>3</sup>. A subsequent electron-pair experiment at Brookhaven discovered the  $J/\psi$  resonance<sup>4</sup>, which was observed simultaneously in electron-positron annihilation at SLAC<sup>5</sup>, and a hint of which had been evident in the 1969 muon-pair data. At Fermilab, experiments by the CFS group<sup>6,7</sup>, by two Chicago-Princeton groups<sup>8,9</sup> and by a Columbia-Cornell-Hawaii-Illinois-Fermilab group<sup>10</sup> carried continuum and resonance measurements to higher masses and beam-energies, using incident pions<sup>9</sup> and neutrons and photons<sup>10</sup> as well as protons.

### A. Continuum

The idea behind these experiments was to probe the internal structure of the nucleon using the well-understood electromagnetic interaction. The graph for this process is shown in Figure 1. A

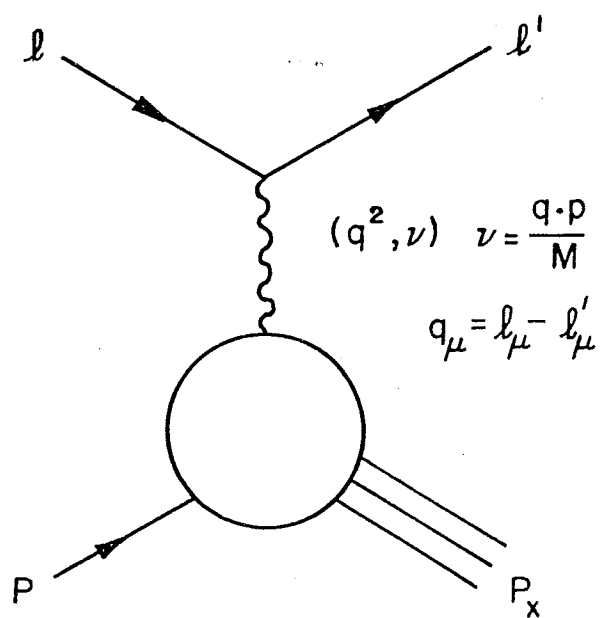


LEPTON PAIR PRODUCTION

FIGURE 1

similar process is deep inelastic lepton-hadron scattering, shown in Figure 2. Evidently a model for what goes on in the hadronic blob should relate the two processes. Drell and Yan devised such a model in 1970<sup>3</sup> using the parton idea of Feynman<sup>11</sup>. Assume the nucleon to be made of pointlike constituents called partons. These partons are very tightly bound to one another by the strong interaction. Nevertheless an electromagnetic interaction of sufficiently short duration might see a free parton ("between" strong interactions). Deep inelastic scattering is such an interaction if  $-q^2$ , the virtual photon mass-squared, and  $\nu$ , the laboratory-frame energy transfer, both become large while their ratio remains finite. In this case the cross-section, which is in general a function of  $q^2$  and  $\nu$ , becomes a function of  $q^2/\nu$  only (when expressed in dimensionless form), a result known as Bjorken scaling<sup>12</sup>. Such scaling was observed at SLAC<sup>13</sup>.

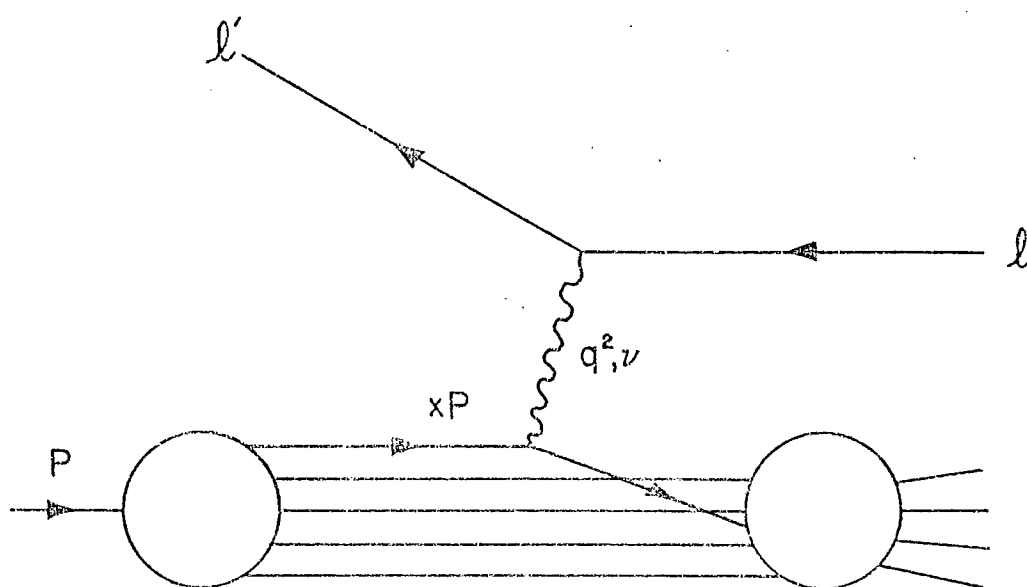
The underlying process is interaction of two partons and two leptons via a virtual photon. This is deep inelastic scattering if the photon is spacelike (Figure 3), while for a timelike photon it is parton-antiparton annihilation into a lepton pair (Figure 4). The amplitude for the annihilation process is the same as for electron-positron annihilation into muon-antimuon and can be calculated in quantum electrodynamics. To calculate it one must know the electric charges of the partons and the probability distribution for finding each kind of parton and antiparton in the



DEEP INELASTIC  
LEPTON-NUCLEON SCATTERING

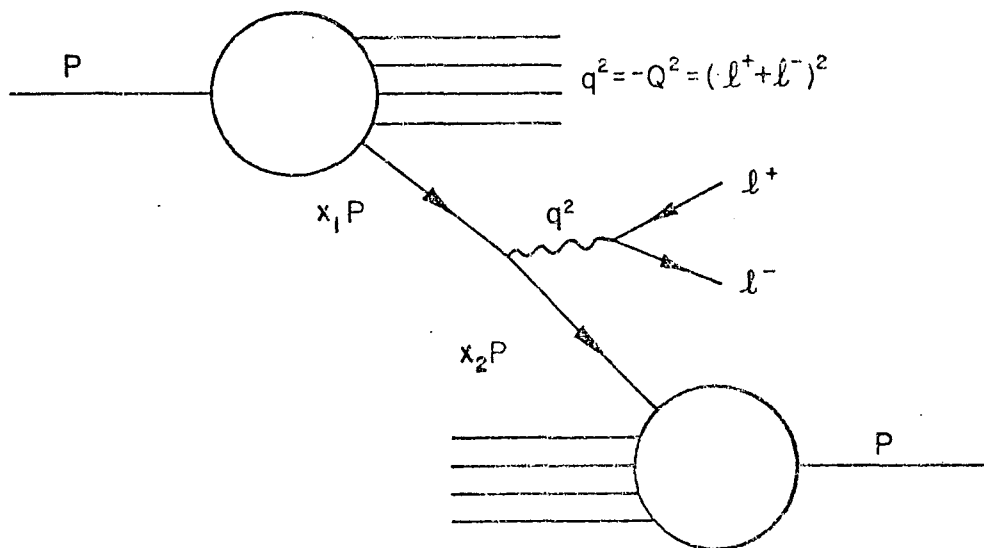
FIGURE 2





PARTON MODEL OF  
DEEP INELASTIC SCATTERING

FIGURE 3



PARTON-ANTIPARTON ANNIHILATION

FIGURE 4

colliding hadrons. If the masses and transverse momenta of the partons can be neglected (i.e. at high energy and large mass), the cross-section is given by

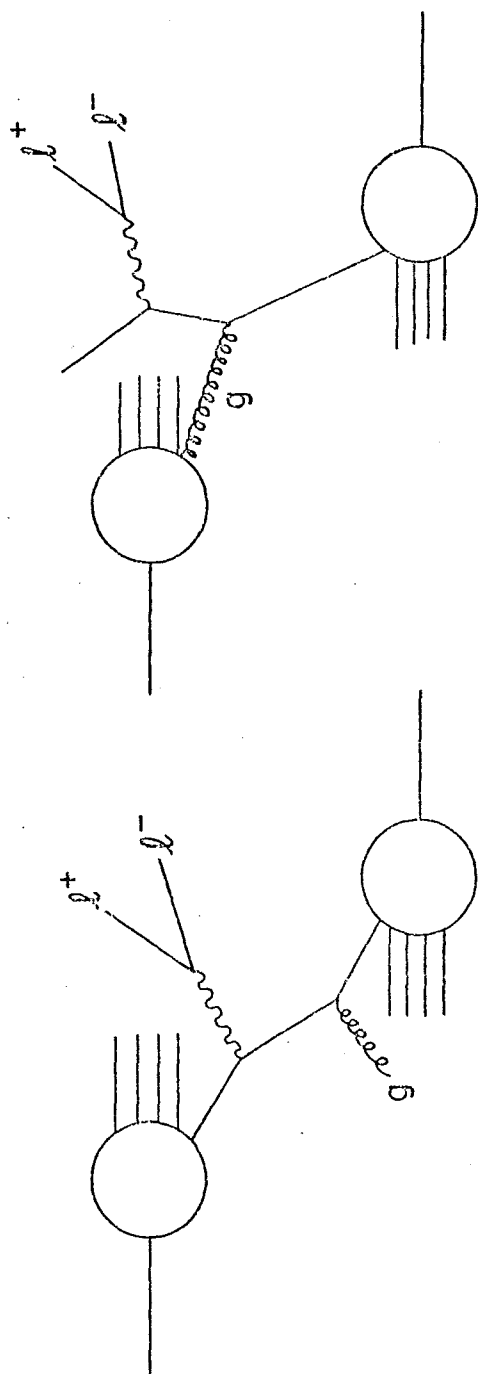
$$\frac{d\sigma}{dQ^2} = \frac{4\pi\alpha^2}{3Q^2} \frac{1}{Q^2} \int_0^1 dx_1 \int_0^1 dx_2 \delta \left( 1 - \frac{x_1 x_2}{\tau} \right) \sum_i \lambda_i^2 f_i^{h_1}(x_1) f_i^{h_2}(x_2)$$

where  $x_1$  and  $x_2$  are the fractions of the longitudinal momenta of the colliding hadrons borne by the partons,  $\tau \equiv Q^2/s = x_1 x_2$  is the mass-squared of the lepton pair over the center-of-mass energy squared,  $\lambda_i$  is the charge of the  $i^{\text{th}}$  kind of parton,  $f_i^h(x) dx$  is the probability of finding the  $i^{\text{th}}$  kind of parton in hadron  $h$  in the range  $dx$  about  $x$ , and  $i$  runs over all kinds of parton and antiparton. This cross-section also exhibits a scaling property: the integral is not a function of  $Q^2$  or  $s$  separately but only of their ratio.

The parton distribution functions are measured in deep inelastic scattering, and so in principle the Drell-Yan cross-section can be computed and compared with experiment to verify or disprove the parton model. In practice, theoretical input is needed in the kinematic regions where measurement is difficult. Many authors<sup>14</sup> have tried to extract parton distributions from the deep inelastic data under various assumptions and theoretical prejudices. It is customary in these endeavors to identify the

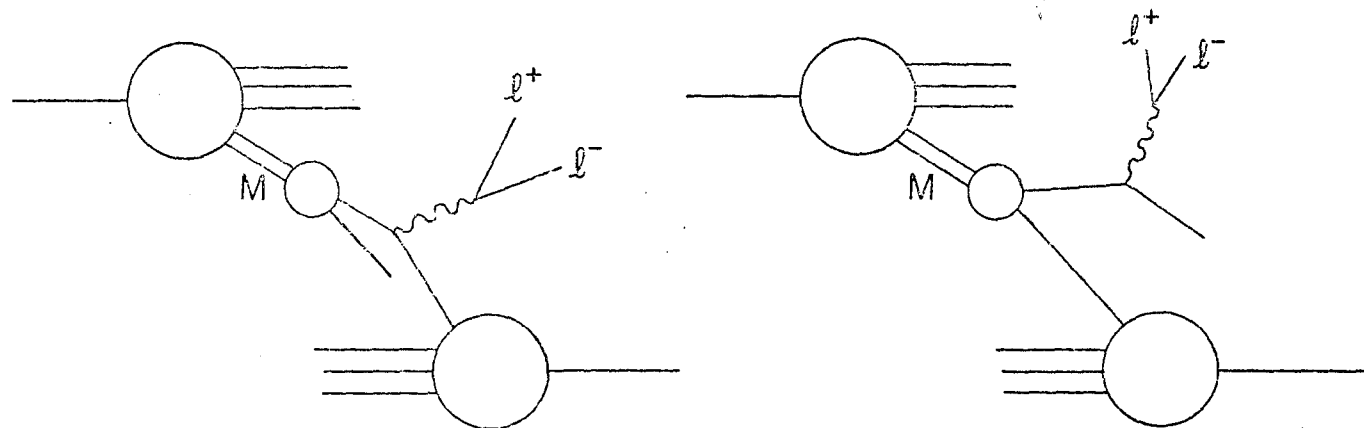
partons with the quarks and gluons of quantum chromodynamics (QCD), bolstered by the experimental observations that partons observed in deep inelastic scattering experiments seem to have spin  $1/2$  and non-integral charge<sup>15</sup>. (Deep inelastic experiments are not sensitive to the gluons, which interact only strongly.) The quarks are commonly divided into "valence" (which carry the quantum numbers of the hadron) and a "sea" of quark-antiquark pairs. Since an antiparton is required for parton-antiparton annihilation, massive lepton pair production is highly sensitive to the sea distribution at large  $x$ , which is not well measured in deep inelastic scattering. Thus clear cut confrontation with the model is difficult, but in so far as experimental results are consistent with the parton model, the two kinds of experiment taken together measure the quark and antiquark distributions over a wide range of  $x$ .

The parton picture is complicated by the observation of scaling violations in deep inelastic scattering<sup>16</sup> and large transverse momentum in lepton pair production<sup>7-10</sup>. In QCD both these effects can arise from corrections to the basic process involving the radiation and absorption of gluons<sup>17</sup> (see Figure 5). Another viewpoint<sup>18</sup> is that the basic lepton pair production process is meson-quark scattering (Figure 6). The two viewpoints may be ultimately equivalent, since the binding of two quarks into a meson is in principle explained by QCD. However, the meson-quark scattering approach, if correct, offers calculational advantages



ONE GLUON PROCESSES

FIGURE 5



# MESON-QUARK SCATTERING

FIGURE 6

in that the complicated high order processes of the binding do not appear explicitly. These issues will be discussed in more detail in Section VI.

## B. Resonances

A considerable number of hypothetical particles decay into lepton pairs: the neutral intermediate vector boson  $Z^0$ <sup>19</sup>, the Lee-Wick heavy photon  $B^0$ <sup>20</sup>, Higgs mesons<sup>21</sup>, positronium-like bound states of new quarks. The discovery of the  $J/\psi$  at Brookhaven<sup>4</sup> and SLAC<sup>5</sup> in 1974 led to many and various speculations as to their nature, but the gradual unearthing of a large family of narrow states and the transitions between them has established the "charmonium" hypothesis<sup>22</sup> quite firmly: these states can all be understood as bound states of the charmed quark proposed by Bjorken and Glashow in 1964<sup>23</sup>. Originally proposed merely to increase the number of quarks to four so that there would be as many quarks as leptons, the charmed quark was given a more solid theoretical basis when Glashow, Iliopoulos, and Maiani<sup>24</sup> found that it could suppress the strangeness-changing weak neutral currents which plagued the theory but were not observed in experiment. The subsequent discovery of the  $J/\psi$  family was striking evidence that the theory was on the right track.

More quarks have been proposed. The widely accepted Weinberg-Salam theory of weak interactions lacks a CP violation if there are only four quarks, in disagreement with experiment<sup>25</sup>.

The addition of two more quarks allows incorporation of a CP violation into the theory. Theories with still more quarks have also been considered<sup>26</sup>.

So the experimental observation of new massive muon-antimuon resonances was not totally unpredicted. The attitude of the experimenters was well summarized by our group leader, Prof. Lederman, in the original experimental proposal<sup>27</sup>. He listed the following goals (among others):

1. Observe and measure the spectrum of virtual photons emitted in p-nucleon collisions via the mass distribution of  $e^+e^-$  pairs:  $p + p \rightarrow e^+e^- + \text{anything} \dots$
2. Search for structures in the above spectrum, publish these and become famous  $\dots$



## II. EXPERIMENTAL APPARATUS

### A. Design Criteria

We wish to measure the lepton pair continuum out to the highest possible masses, and also to be sensitive to any massive resonances which may exist. To improve on previous continuum measurements we need to be sensitive to less than  $10^{-11}$  of the total proton-nucleon cross-section, thus we must be able to take large incident beam flux and high counting rates in the apparatus. Good resolution is also important. Good mass resolution is particularly important for the resonance search; good resolution in other variables as well minimizes corrections to the observed data. Since massive objects will tend to be produced at rest or moving slowly in the collision rest frame, we choose to view the collision at  $90^\circ$ , thus avoiding the huge hadronic flux at  $0^\circ$  and  $180^\circ$ .

We have the choice of detecting muons or electrons. Muons can be distinguished from the copiously produced hadrons by their highly penetrating character; electrons, by their electromagnetic showering properties. The main background in a muon experiment is muons from the decay of pions and kaons produced in the target. To suppress this it is necessary to put material immediately downstream of the target, to absorb these particles before they can decay. The advantage over electrons is that counting rates are lowered by a factor of  $10^4$ , allowing a corresponding increase in beam intensity. The disadvantage is that scattering of the muons in the hadron

absorber degrades knowledge of their production angles, thus worsening resolution. Having already done an electron experiment<sup>6</sup>, we chose to do muons in order to extend the measurement to higher mass. A preliminary muon experiment was performed in 1976<sup>7</sup> using an apparatus configuration very similar to that of the electron experiment; the experience thereby gained allowed us to optimize the design of the present experiment and improve both sensitivity and resolution.

The basic scheme is to measure the trajectories of the muons after deflecting them with a magnetic field. The momentum of each muon is determined by the amount of its deflection according to the relation

$$p = \frac{p_t}{\sin \theta_2 - \sin \theta_1}$$

where  $p_t$  is the "transverse momentum kick" of the magnet

$$p_t = e \int \vec{B} \cdot d\vec{l}$$

and  $\theta_1$  and  $\theta_2$  are the angles of the muon trajectory before and after deflection, measured in the plane of deflection.  $e$  is the charge of the muon and  $\int \vec{B} \cdot d\vec{l}$  is the line integral of the magnetic field along the muon trajectory. Below some momentum the muons will be deflected entirely out of the spectrometer. This

threshold momentum should be high if we are to achieve good sensitivity at high mass, since the rates in the spectrometer will be dominated by the lowest momentum muons which traverse it.

To achieve good resolution the apparatus must be able to measure angles to high precision. To do this with scintillation counters is very expensive, since very many of them are required if large acceptance is to be maintained. Alternatively, multiwire proportional chambers (MWPC's) or drift chambers can be used. However, to keep trigger rates down the detectors should also have good time resolution so that coincidence windows can be short. Since the Fermilab beam comes in bursts (called RF buckets) of about 1 nsec duration separated by 18.9 nsec, extremely good resolution is not required. It is not difficult to achieve resolution of less than an RF bucket with scintillation counters, but proportional chambers typically integrate over two or three buckets, and drift chambers over many more. We used proportional chambers in combination with scintillation counters. Our chambers were sensitive to three RF buckets, but scintillation counter hodoscopes were used to eliminate out-of-time chamber hits.

#### B. Apparatus Overview

The apparatus (shown in Figure 7) was a two arm magnetic spectrometer viewing the proton-nucleus collision from opposite sides at  $90^\circ$  in the proton-nucleon center-of-momentum system (CMS). Each arm covered a solid angle of 0.2 sr in the CMS and consisted of hadron absorber, two magnets, and scintillation counters and

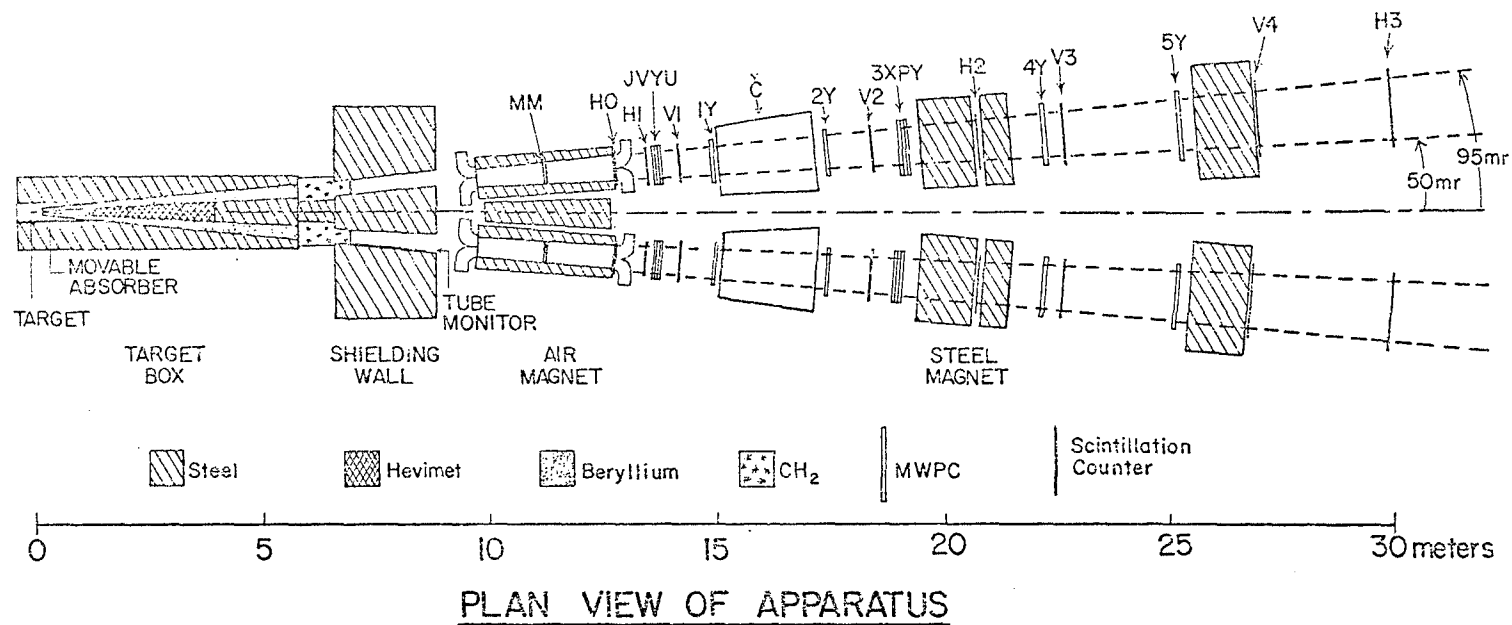


FIGURE 7

MWPC's. The magnets deflected charged particles vertically and in opposite directions, so that if the first (air gap) magnet deflected positive muons up, say, the second (solid steel) magnet deflected them down. Each arm was up/down symmetric and accepted both positive and negative muons. The two arms were alike, but we called one the up arm and the other the down arm in accordance with the coordinate system used to describe each arm, defined as follows: let the z-axis point downstream from the target along the center of the arm and the x-axis horizontally outward from the z-axis (i.e. away from the other arm). Then if each arm has a right-handed coordinate system, one y-axis points up and the other points down. This definition of coordinate systems was chosen for its pleasing symmetry properties and because it simplified the coding of the analysis program, in which the same code was used for each arm in turn.

To maximize the amount of beam we could accept, we placed no detectors upstream of the air gap magnet, where counting rates were an order of magnitude higher than downstream. The momentum was computed from the measured trajectory downstream of the air magnet assuming that the undeflected track pointed back to the target. The inaccuracy of this assumption due to multiple scattering in the hadron absorber resulted in an r.m.s. momentum resolution of 2%, illustrating the trade-off between resolution and rate capability.

The spectrometer apertures were wide horizontally and short vertically. The fields in the two air gap magnets were oriented along the long dimension of the gaps. The muon production angles were thus measured primarily perpendicularly to the plane of magnetic deflection. This decoupling of the production angle measurement from the momentum measurement had important advantages over the more usual magnet design in which the field is oriented along the short dimension. First, the copious low momentum muons were swept out of the spectrometer, rather than being swept across the aperture into the other arm. Second, events originating not in the target but in upstream vacuum windows or downstream in the beam dump could be rejected by projection of the track back to the target in the horizontal plane.

In order to suppress possible backgrounds, the apparatus was designed with a considerable amount of redundancy. The momentum of the muon was remeasured to  $\pm 15\%$  by the steel magnet, to reject low energy muons simulating high momentum by traversing the air magnet along strange trajectories involving scattering from pole pieces, being deflected back into the aperture by the field in the coils, etc. Another handle on this background was provided by the mid-magnet (MM) MWPC which could be used to verify the muon position in the middle of the air magnet. A gas Cerenkov counter filled with nitrogen provided a 4 GeV muon energy threshold, as did the energy loss in the 6' of steel magnet and 41" of steel

further downstream. At full current the magnets provided a 15 GeV threshold, but the Cerenkov counter and additional steel were probably still useful in eliminating certain classes of "junk" triggers such as accidental coincidences of low energy muons upstream and downstream of the steel magnet.

### C. Detailed Description

The apparatus is here described in detail proceeding from upstream to downstream.

#### 1. Beam line

The experiment was performed in the Proton Center pit of the Fermi National Accelerator Laboratory. A small fraction of the extracted primary proton beam was brought to the Proton Center pre-target area by Switchyard and Proton Area magnets mostly not under our control. It was steered and focused onto our target by two dipole and three quadrupole magnets of the standard FNAL beam line types, which we could control using the MAC beam line computer system. We were able to focus the beam to a spot 0.03 cm wide by 0.08 cm high (as measured during the CFS hadron pair experiment<sup>28</sup>). The horizontal and vertical beam profiles just upstream of these magnets and just downstream (2' upstream of our target) were measured by 0.5 mm spacing separated-wire ionization chambers provided by FNAL Research Services, who also provided a secondary emission monitor (SEM) which measured beam intensity.

## 2. Target box

The target box (Figure 8) was a large helium-filled enclosure containing ten drawers, on which were mounted the target holder, beam dump, and part of the hadron absorber. The drawers were 1' square in cross-section and were arrayed five across and two deep; they slid in and out on rails. Surrounding the target box was a 16"-thick layer of steel to shield against radioactivity.

## 3. Targets

Three different targets were used. Each was a rectangle of thin sheet metal standing on its long edge, with the beam impinging on the short edge. Most of the data were obtained using a 1"-long platinum target, chosen in order to maximize the ratio of signal to single count rates, since the massive lepton pair signal had been measured<sup>7</sup> to have an approximately linear nucleon number ( $A$ ) dependence while the singles rate presumably goes as  $A^{2/3}$  (see Section V.B.1 below). We also did some running aimed at measuring the  $A$  dependence, during which we alternated between the platinum target and a 4" beryllium target. After the run we discovered that the last 17/64" of the platinum target had melted; the consequences of this are discussed in Section V.B. The third target was the 3" copper target, which was used during a fraction of the run. The targets were mounted in a holder which could be translated horizontally (transversely to the beam direction) by means of a stepping motor under control of the MAC



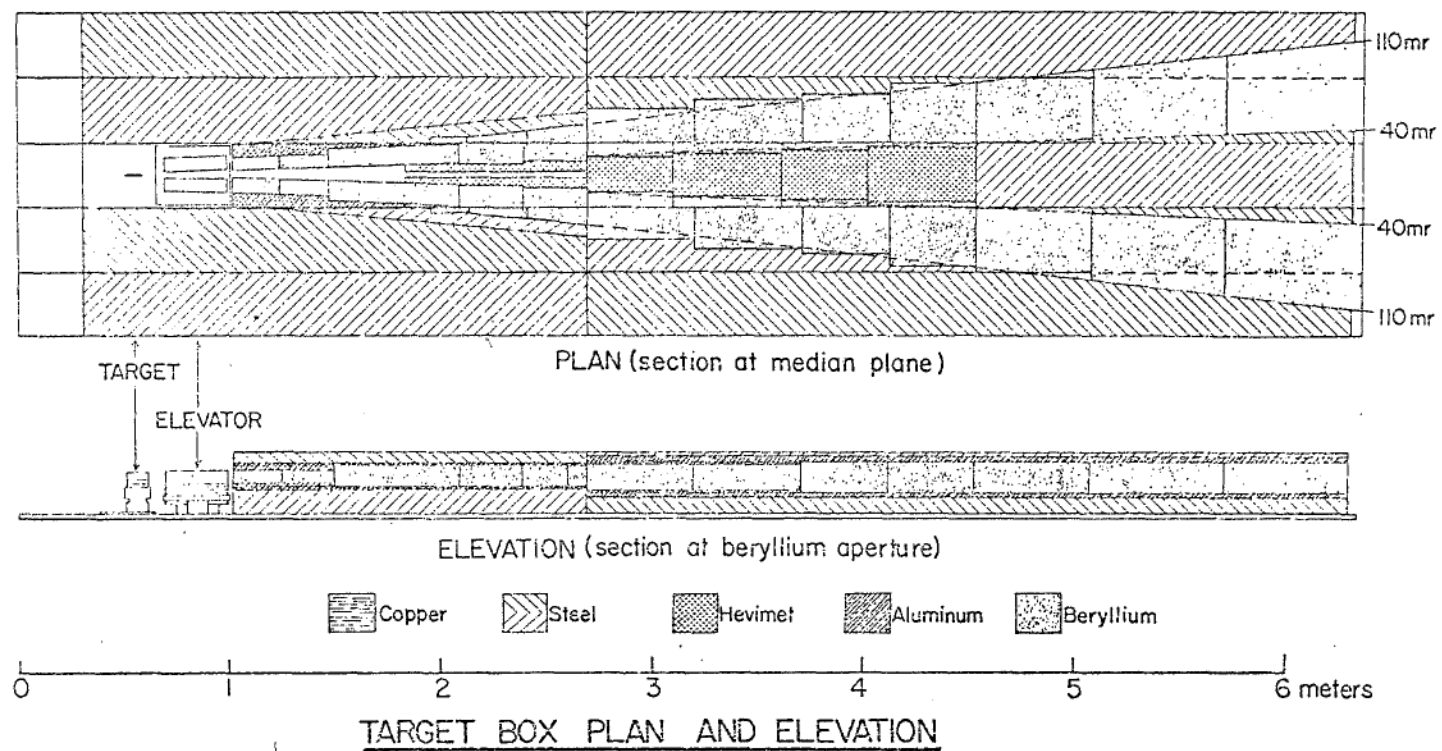


FIGURE 8

computer system. They were narrow transversely in order to minimize the scattering of outgoing muons. Target parameters are given in Table I.

#### 4. Beam dump

Typically 30% of the beam interacted in the target; the rest was absorbed in a water-cooled beam dump. The dump began 7' downstream of the center of the target. It consisted of 6' of Mallory 1000 Hevimet (90% tungsten, 6% nickel, 4% copper) followed by 6' of steel. A cone of Hevimet extended 3' upstream to reduce the decay path for hadrons produced at small angles, but it had a 1"-square hole in its center to allow the unscattered beam to pass through. Hevimet was used for its short hadronic absorption length (11 cm), which minimizes decay of pions and kaons and also minimizes transverse spread of the hadronic shower and hence leakage of particles out of the dump into the aperture.

#### 5. Targeting monitors

The fraction of the beam intercepted by the target (targeting fraction) was monitored using two different methods. A 1"-diameter hole in the steel shielding directly above the target provided a decay space for hadrons emitted upwards, and the resulting muon flux was viewed (after penetration of the concrete pre-target area roof and some dirt) by a four-element scintillation counter telescope called the  $90^\circ$  monitor. This was our main targeting fraction monitor. The  $90^\circ$  monitor was somewhat sensitive to

TABLE I

## Target Properties

Material	Length (cm)	Width (mm)	A	Density (g/cm <sup>3</sup> )	# Abs. Lengths	Effective Length (cm)
Pt	1.87±.04	.660±.013	195.09	20.65±.40	.2	1.70±.04
Be	10.38±.10	1.65±.013	9.01	1.835±.014	.28	9.04±.09
Cu	7.62	.889	63.54	8.96	.52	5.94

## NOTE

Length of Pt target is given as measured after run. Widths and densities of Pt and Be were measured using leftover pieces from the same sheet metal stock.

interactions in the dump; typically the ratio of its "target in" to "target out" counting rates was about 4. A second targeting monitor was a single-wire proportional tube counter called the tube monitor; it viewed the target from the large angle side of the down arm aperture and had a target in/target out ratio similar to that of the  $90^\circ$  monitor.

#### 6. Hadron absorber

In the laboratory rest frame each spectrometer arm covered  $\pm 10$  mrad vertically and 45 mrad horizontally. The two arms were centered horizontally on the angles  $\pm(\arctan 0.0725)$ , which correspond to  $\pm 90^\circ$  in the CMS at 400 GeV beam energy. Within the target box the spectrometer apertures were filled with hadron absorber, the first foot of which sat on a remotely controlled elevator platform which could be raised or lowered to bring copper, beryllium, or helium (i.e. no absorber) into the aperture. Almost all of our data was taken with the copper absorber, as we found that rates in some of the detectors increased by as much as a factor of three with beryllium; the small improvement in resolution with beryllium (see Section D below) was deemed to be not worth the accompanying beam intensity limitation. The rest of the absorber consisted of 210" of beryllium in the target box and 60" of  $\text{CH}_2$  downstream of the target box.

The beryllium was oversized, its coverage being nowhere less than 70 mrad horizontally nor  $\pm 20$  mrad vertically. It was

carefully fit into the target box in large pieces in order to minimize cracks and gaps. It was sandwiched with steel and Hevimet in the horizontal direction and with aluminum plates which were in turn sandwiched with steel in the vertical direction. This configuration was chosen to maximize the amount of material of short hadronic absorption length outside the aperture while minimizing the scattering of particles out of the steel and Hevimet into the aperture. Its design benefited from our previous experience<sup>7</sup> in the detection of massive muon pairs and from a detailed Monte Carlo study.

The  $\text{CH}_2$  was included because of the worry that slow neutrons might be able to penetrate the beryllium in significant numbers and contribute to counting rates. Evidence failed to support this view however, and after run 1016 all but 6" of the  $\text{CH}_2$  was removed and 55" of beryllium installed in its place.

#### 7. Shielding wall

Three feet downstream of the end of the target box was a 7'-thick steel shielding wall. The apertures were made slightly oversized. They were tapered horizontally but not vertically. The tube monitor was placed in the downstream end of the down arm shielding wall aperture in the lower large-angle corner.

#### 8. Air gap magnets

Next came the air gap analyzing magnets. They were 10'-long dipole magnets centered at  $z=440''$  from the center of the

target. The field was horizontal (deflecting charged particles vertically), and, due to tapering of the gaps, it decreased in magnitude with increasing  $z$ . The pole pieces were located at 49 and 97 mrad. At maximum current (1500 amperes) the mean value of the field was 13 kg, giving a transverse momentum kick of 1.2 GeV. The two magnets were wired in series. Their fields pointed in the same direction, so that if positive particles were deflected up in one arm, negative particles were deflected down in the other; this configuration favors pairs produced at small transverse momentum and thus has larger acceptance than the configuration in which the fields are directed oppositely.

The field integral of each magnet as a function of  $x$  and  $y$  was mapped at several currents using a 15'-long flip coil connected to a current integrator, and the magnitude of the field at the upstream end near the 49 mrad pole piece was measured constantly to 0.2% by a Hall Effect probe. The magnet current was monitored using a precision shunt which was sensitive to 0.1% current variations. A second current monitor was the value read back from the power supply via the MAC computer system. A further check on the shape and magnitude of the field was the observed mass of the  $J/\psi$  resonance as a function of current and position in the magnet; we used it to measure the field near the pole pieces where flip coil measurements were difficult.

## 9. Detectors

Table II lists the detectors, in order as encountered by a muon. The first detector in each arm was an MWPC with horizontal wires spaced 2 mm apart, located in the center of the air magnet. These mid-magnet (MM) chambers were designed to operate efficiently at the high counting rates (typically 10 MHz) encountered in that location. Their narrow gaps (1/8") and the use of 0.1% freon in the gas mixture reduced the maximum duration of the ion cascade to about 50 nsec, and special deadtimeless amplifier/discriminator cards were used.

Between the air magnet and the steel magnet were four stations of detectors. The first station consisted of a plane of horizontal scintillation counters designated H1, an MWPC containing three planes of wires of 2 mm spacing (borrowed from the MIT group of Prof. Ting and hence called the J chambers), and a vertical scintillation counter hodoscope known as V1. H1 was used in the trigger. The three J chambers (JY, JU, and JV) measured in the y direction and along two axes at  $60^\circ$  and  $120^\circ$  from the y axis. V1 consisted of 18 1.4"-wide scintillation counters. It supplemented the MWPC's in measuring x, and its good time resolution (one accelerator RF bucket) allowed elimination of out-of-time MWPC hits. A second plane of horizontal scintillation counters called H0 was added upstream of H1 after run 838. It consisted of five 2"-wide strips fit snugly against the downstream face of the magnet iron,

TABLE II  
Detectors

Name	Type	z position (inches)	
		Up Arm	Down Arm
MM	MWPC	440.0	440.0
HO	hodoscope	500.0	500.0
HL	hodoscope	529.0	529.0
JV	MWPC	537.6	537.9
JY	MWPC	538.6	538.9
JU	MWPC	539.6	539.9
V1	hodoscope	558.8	555.6
1Y	MWPC	588.1	588.1
C	cerenkov		
2Y	MWPC	688.0	688.0
V2	hodoscope	724.0	724.0
3X	MWPC	745.1	745.2
3P	MWPC	750.6	750.7
3Y	MWPC	756.1	756.2
H2	hodoscope	817.0	817.0
4Y	MWPC	875.0	875.0
V3	hodoscope	893.0	893.0
5Y	MWPC	990.6	990.6
V4	hodoscope	1056.5	1053.0
H3	hodoscope	1173.0	1173.0



restricting the trigger to muons emerging from the magnet aperture and eliminating the roughly 30% of pair triggers due to muons emerging through the coils.

The next station consisted of a single 2 mm spacing MWPC measuring  $y$  and called 1Y. Between it and the third station was a 7'-long nitrogen-filled Cerenkov counter. It was the "head" section of a nitrogen Cerenkov counter used in the CFS hadron pair experiment and is described in detail in R. J. Fisk's Ph.D. thesis<sup>28</sup>. It was used in the muon experiment primarily for its good time resolution (1 nsec r.m.s.) and also for its insensitivity to slow particles.

The third station was a 3 mm spacing MWPC measuring  $y$  and called 2Y. The fourth station consisted of a vertical hodoscope of 24 1.4"-wide scintillation counters, called V2, and three 3 mm MWPC's (3Y, 3X, and 3P) measuring  $y$ ,  $x$ , and a coordinate ( $p$ ) rotated by ( $\arctan 1/8$ ) with respect to  $y$ . The preponderance of chambers measuring  $y$  (and  $p$ , which is highly correlated with  $y$ ) was intended to provide accurate measurement of the magnetic deflection angle even if one or two chambers should be missing due to inefficiency.

#### 10. Steel magnets

Figure 9 shows a steel magnet in detail. Each steel magnet was made of nine 8"-thick steel slabs welded together into a 4' section followed by a 2' section, separated by a 6" gap. The

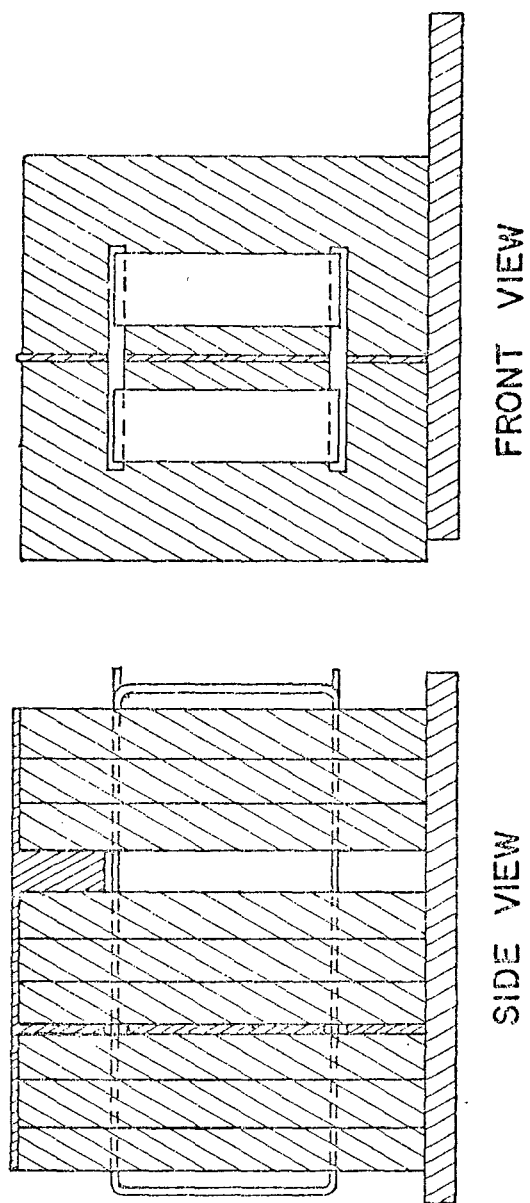


FIGURE 9

coil consisted of hollow 0.825" by 0.625" water-cooled copper. The magnet was run at a current of 1000 A, which was sufficient to saturate the steel and provide a fairly uniform dipole field. The field integral was measured using the muons themselves, studying the distribution in deflection angle as a function of momentum measured by the air magnet. The transverse momentum kick  $p_t$  was thus measured to be 1.14 GeV. The two magnets were wired in series and the current monitored to 0.1% by a precision shunt. Their fields were equal and oriented in the same direction, opposite to the direction of the fields in the air magnets. Muons were thus partially refocused by the steel magnets, allowing downstream detectors to be reduced in size.

The momentum resolution of such a magnet is limited by multiple scattering of the muons as they traverse the steel. The r.m.s. scattering angle is given by<sup>29</sup>

$$\theta_{\text{rms}} = \frac{.014 \text{ GeV}}{p} \sqrt{\frac{L}{R}} \left[ 1 + \frac{1}{9} \log_{10} \left( \frac{L}{R} \right) \right]$$

where  $p$  is the muon momentum,  $L$  is the length of the magnet, and  $R = 1.77 \text{ cm}$  is the radiation length of steel<sup>30</sup>. The magnetic deflection angle  $\theta_{\text{bend}}$  also depends inversely on the momentum and is given in the small angle approximation by

$$\theta_{\text{bend}} = p_t / p = 1.14 \text{ GeV}/p.$$

Thus the r.m.s. momentum resolution is given by

$$\frac{\sigma_p}{p} = \frac{\theta_{rms}}{\theta_{bend}}$$

$$= 0.15.$$

This was entirely adequate for the task of rejecting background events (see section V.A).

#### 11. More detectors

In the gap between the two sections of each steel magnet was a plane of horizontal scintillation counters (H2) used in the trigger. It consisted of four counters each 8" wide, with the upper and lower of the four angled so that the vertical aperture was larger at large horizontal angles than at small ones. Since low momentum muons were deflected through large angles in the air magnet, they tended to be at large positive or negative y at H2, so the tapering of H2 provided some rejection of low transverse momentum muons (and hence of low mass pairs).

Following the steel magnet were two 3 mm MWPC's with horizontal wires designated 4Y and 5Y, and a vertical scintillation hodoscope (V3) made of 9 5"-wide strips. Following 41" of steel (further to "harden" the trigger) were a vertical hodoscope (V4) made of 13 6"-wide strips overlapped to give 2" resolution, and

the final trigger plane, H3, consisting of four 8"-wide horizontal scintillation counters.

#### D. Resolution

Each spectrometer arm measured angles to a precision limited by chamber wire spacings and by multiple scattering in the hadron absorber. The contribution of wire spacing to angle measurement error is straightforward. The multiple scattering contribution can be computed from

$$\theta_{\text{rms}}^2 = \left( \frac{0.016 \text{ GeV}}{p} \right)^2 \frac{L}{R} \equiv C \frac{L}{R} \quad (1)$$

where  $\theta_{\text{rms}}^2$  = projected mean square scattering angle

$p$  = muon momentum

$L$  = length of absorber

$R$  = radiation length of absorber material.

(This formula differs from the formula of section C.10 above in that this is the appropriate form for very thin absorber, for which the logarithmic correction term is negligible. Since, however, it is to be integrated over thick absorbers, the constant has been increased appropriately.) Calculation of the resolution in variables of physical interest is complicated because integrations must be done over the actual event distribution in the other variables and also because the resolution varies from event to event depending on which chambers participate in the reconstructed track. For

illustrative purposes I here compute the mass resolution under some simplifying assumptions. The actual resolution can be studied using the events themselves; this will be discussed below. For simplicity I use the small angle approximation throughout, which is accurate to better than 0.5% for our apparatus. I also assume that all chambers are 100% efficient, and I neglect vertical production angles compared to horizontal (accurate to better than 2%). The mass can then be approximated by

$$m = \sqrt{p_1 p_2} \left( \theta_1 + \theta_2 \right)$$

where  $p_i$ ,  $\theta_i$  = momentum and horizontal angle of muon  $i$ . Thus the mean square mass resolution is approximately

$$\left( \frac{\sigma_m}{m} \right)^2 = \frac{1}{4} \left( \frac{\sigma_{p_1}}{p_1} \right)^2 + \frac{1}{4} \left( \frac{\sigma_{p_2}}{p_2} \right)^2 + \frac{\sigma_{\theta_1}^2 + \sigma_{\theta_2}^2}{\left( \theta_1 + \theta_2 \right)^2} .$$

For symmetric events ( $p_1 = p_2 \equiv p$ ,  $\theta_1 = \theta_2 \equiv \theta$ ) this becomes

$$\left( \frac{\sigma_m}{m} \right)^2 = \frac{1}{2} \left( \frac{\sigma_p}{p} \right)^2 + \frac{1}{2} \left( \frac{\sigma_\theta}{\theta} \right)^2 .$$

Each term contains a contribution due to multiple scattering and a contribution due to MWPC measuring error:

$$\left(\frac{\sigma_m}{m}\right)^2 = \frac{1}{2} \left(\frac{\sigma_p}{p}\right)_{\text{scat}}^2 + \frac{1}{2} \left(\frac{\sigma_p}{p}\right)_{\text{meas}}^2 + \frac{1}{2} \left(\frac{\sigma_\theta}{\theta}\right)_{\text{scat}}^2 + \frac{1}{2} \left(\frac{\sigma_\theta}{\theta}\right)_{\text{meas}}^2.$$

I now discuss each term in turn.

### 1. Multiple Scattering Momentum Error

Figure 10a illustrates the effect of scattering in an infinitesimal slice  $dz$  of the absorber on the measured momentum. Calling the transverse momentum kick of the magnet  $A$ , the true momentum is

$$p = A/\theta_{\text{bend}},$$

but the spectrometer measures

$$p_{\text{meas}} = A/(\theta_{\text{bend}} + \Delta\theta).$$

The momentum error is

$$\begin{aligned} \Delta p &= p_{\text{meas}} - p \\ &\approx -\frac{A\Delta\theta}{\theta_{\text{bend}}^2} = -\frac{A}{\theta_{\text{bend}}^2} \frac{z}{z_{\text{mag}}} \theta_{\text{scat}}. \end{aligned}$$





Squaring and averaging, and substituting from Equation (1) above,

$$d\sigma_p^2 = \left( \frac{.016 \text{ GeV}}{A} \frac{z}{z_{\text{mag}}} p \right)^2 \frac{dz}{R} .$$

Integrating over the whole absorber,

$$\begin{aligned} \left( \frac{\sigma_p}{p} \right)_{\text{scat}}^2 &= \left( \frac{.016 \text{ GeV}}{A z_{\text{mag}}} \right)^2 \frac{1}{R} \int_{z_A}^{z_B} z^2 dz \\ &= \left( \frac{.016 \text{ GeV}}{A z_{\text{mag}}} \right)^2 \frac{1}{3R} \left( z_B^3 - z_A^3 \right) . \end{aligned}$$

For our absorber configuration (specified in Table III), this gives

$$\left( \frac{\sigma_p}{p} \right)_{\text{scat}} = 2.14 \times 10^{-2}$$

independent of momentum. This is affected negligibly if beryllium is used as the first foot of absorber.

## 2. MWPC Momentum Error

The vertical angle after the magnet is measured by the four stations of MWPC's JYU, 1Y, 2Y, and 3XPY. The resolution is most easily calculated by representing JYU and 3XPY

TABLE III

Hadron Absorber Configuration  
(Before run 1017)

Material	z pos.	Length	Rad. Length	# Rad. Lengths
Cu	5"	12"	1.43 cm	21.31
Be	18"	210"	35.3 cm	15.11
CH <sub>2</sub>	228"	60"	48 cm	3.17

each by a single chamber measuring  $y$  with reduced wire spacing. The 2 mm wire spacing at the J station is then multiplied by  $\sqrt{2/3}$  and the 2 mm spacing at the 3 station by  $1/\sqrt{2}$  to give the effective chamber configuration of Table IVa. The vertical angle is determined by a linear least squares fit to the points  $(y_i, z_i)$  measured by the four effective chambers. Multiple scattering in the counters and chambers of the spectrometer may be neglected compared to scattering in the hadron absorber. The errors at the four effective chambers are then uncorrelated. Each chamber has an r.m.s. measuring error  $\sigma_i$  given by

$$\sigma_i = w_i / \sqrt{12}$$

where  $w_i$  is the wire spacing; this is the r.m.s. value of a rectangular distribution of width  $w_i$ . Applying standard least squares fit formulae, the mean squared error on the vertical angle is

$$\sigma_\theta^2 = \frac{1}{\sum_i \frac{z_i^2}{\sigma_i^2} - \langle z \rangle^2 \sum_i \frac{1}{\sigma_i^2}}$$

where  $\langle z \rangle$  is the weighted average of  $z_i$

TABLE IV

## Effective Chamber Configuration

## a. y chambers

z	wire spacing	r.m.s. measuring error
539"	1.633 mm	0.471 mm
588"	2 mm	0.577 mm
688"	3 mm	0.866 mm
753"	2.121 mm	0.612 mm

## b. x chambers

539"	1.826 mm	0.537 mm
745"	3 mm	0.866 mm

$$\langle z \rangle = \frac{\sum_i \frac{z_i}{\sigma_i^2}}{\sum_i \frac{1}{\sigma_i^2}} .$$

For the effective chamber configuration of Table IVa this error is  $\sigma_\theta = 1.33 \times 10^{-4}$ . This translates into a momentum error

$$\left( \frac{\sigma_p}{p} \right)_{\text{meas}} = \frac{\sigma_\theta}{\theta} = 1.11 \times 10^{-4} p$$

increasing linearly with momentum.

### 3. Multiple Scattering Horizontal Angle Error

The horizontal angle  $\theta$  is measured by JYU and 3X.

If they are used simply to determine the horizontal angle after the absorber, the angle error due to multiple scattering is the full  $\theta_{\text{rms}}$  of Equation (1). For the absorber configuration of Table III, this gives

$$(\sigma_\theta)_{\text{scat}} = 0.10/p .$$

It is possible to do better than this as discussed in Section 5 below.

### 4. MWPC Horizontal Angle Error

The MWPC measuring error is most easily calculated

by representing JYU as a single chamber measuring  $x$  with 1.826 mm wire spacing (Table IVb). The r.m.s. horizontal angle error of JYU and 3X is then

$$(\sigma_{\theta})_{\text{meas}} = 1.94 \times 10^{-4}$$

which is negligible compared with  $(\sigma_{\theta})_{\text{scat.}}$

#### 5. Constrained Fit to Horizontal Angle

The simple horizontal angle calculation above can be improved on by using the fact that the track originated in the target and performing a linear least squares fit to the positions at the target and at JYU and 3X. The fit function is

$$x = \theta z + x_t = \frac{x_2 - x_1}{z_2 - z_1} z + x_t$$

and the parameters to be determined are  $x_t$ ,  $x_1$ , and  $x_2$  = positions at target, JYU, and 3X. Multiple scattering in the absorber introduces correlations which are represented by the variance matrix

$$S = \begin{pmatrix} S_1^2 & S_{12} \\ S_{12} & S_2^2 \end{pmatrix}$$

where  $S_1^2$  is the mean squared error at the J station due to scattering in the absorber,  $S_2^2$  the mean squared error at the 3

station, and  $S_{12}$  the correlation. Figure 10b illustrates the contribution from each  $dz$  of absorber:

$$dS_1^2 = (z_1 - z)^2 \theta_{\text{rms}}^2 = C (z_1 - z)^2 dz/R$$

$$dS_2^2 = (z_2 - z)^2 \theta_{\text{rms}}^2 = C (z_2 - z)^2 dz/R$$

$$\begin{aligned} dS_{12} &= (z_1 - z) (z_2 - z) \theta_{\text{rms}}^2 \\ &= C (z_1 - z) (z_2 - z) dz/R \end{aligned}$$

The last follows since the errors at  $z_1$  and  $z_2$  from each  $dz$  of absorber are 100% correlated, i.e.  $S_{12}^2 = S_1^2 S_2^2$ . Integrating over the whole absorber,

$$S_1^2 = C \left[ (z_1 - z_A)^3 - (z_1 - z_B)^3 \right] / 3R$$

$$S_2^2 = C \left[ (z_2 - z_A)^3 - (z_2 - z_B)^3 \right] / 3R$$

$$S_{12} = C \left[ z_1 z_2 (z_B - z_A) + \frac{1}{2} (z_1 + z_2) (z_B^2 - z_A^2) + \frac{1}{3} (z_B^3 - z_A^3) \right]$$

There is also a contribution due to the finite length of the target. This can be treated as errors at  $z_1$  and  $z_2$  by translating coordinates so that  $x_t = 0$ . Since this causes errors at  $z_1$  and  $z_2$  which are 100% correlated, the resulting variance matrix

is

$$T = \begin{pmatrix} T^2 & T^2 \\ T^2 & T^2 \end{pmatrix}$$

where  $T^2 = L_T^2 \tan^2 \theta / 12$  and  $L_T$  = length of target.

The third contribution to the variance matrix is the measuring errors of the chambers, which are obviously uncorrelated and thus represented by

$$M = \begin{pmatrix} M_1^2 & 0 \\ 0 & M_2^2 \end{pmatrix}$$

Thus the complete variance matrix is

$$V = S + T + M$$

$$\equiv \begin{pmatrix} \sigma_1^2 & \sigma_{12} \\ \sigma_{12} & \sigma_2^2 \end{pmatrix}$$

Applying standard linear least squares formulae, the mean squared error of  $\theta$  is then given by



$$\sigma_{\theta}^2 = \frac{\sigma_1^2 \sigma_2^2 - \sigma_{12}^2}{z_1^2 \sigma_2^2 - 2z_1 z_2 \sigma_{12} + z_2^2 \sigma_1^2}$$

For the absorber configuration of Table III, and neglecting a slight additional  $\theta$  dependence, this gives

$$\frac{\sigma_{\theta}}{\theta} \approx \frac{.15}{m} \sqrt{\frac{1 + 1.48 \times 10^{-4} p^2}{1 + 1.06 \times 10^{-4} p^2}}$$

for symmetric events. If the first foot of absorber is beryllium, this becomes

$$\frac{\sigma_{\theta}}{\theta} \approx \frac{.07}{m} \sqrt{\frac{1 + 2.71 \times 10^{-4} p^2}{1 + 1.07 \times 10^{-4} p^2}}$$

which is better by a factor of 2 at 50 GeV momentum than the error with copper.

## 6. Calculated Mass Resolution

Combining the above contributions

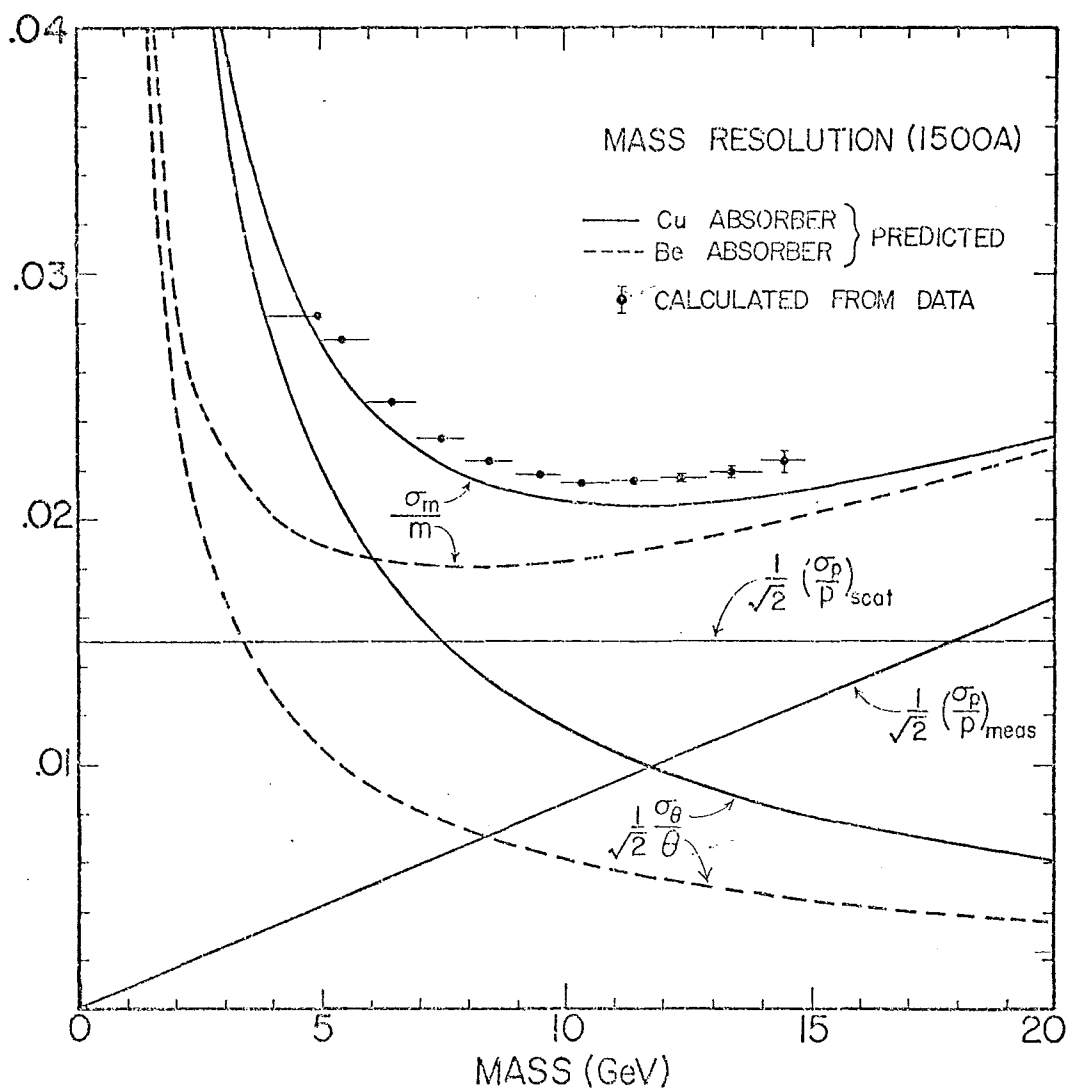
$$\left(\frac{\sigma_m}{m}\right)^2 = .0151^2 + \left(\frac{5.54 \times 10^{-5} m}{\theta}\right)^2 + \left(\frac{.108}{m} \sqrt{\frac{1 + 3.69 \times 10^{-5} m^2/\theta^2}{1 + 2.66 \times 10^{-5} m^2/\theta^2}}\right)^2$$

Figure 11 graphs  $\frac{\sigma_m}{m}$  and each of its components evaluated for  $\theta = 0.066$  (the mean horizontal angle of the data) and 1500A current in the air magnet.

#### 7. Mass Resolution From Data

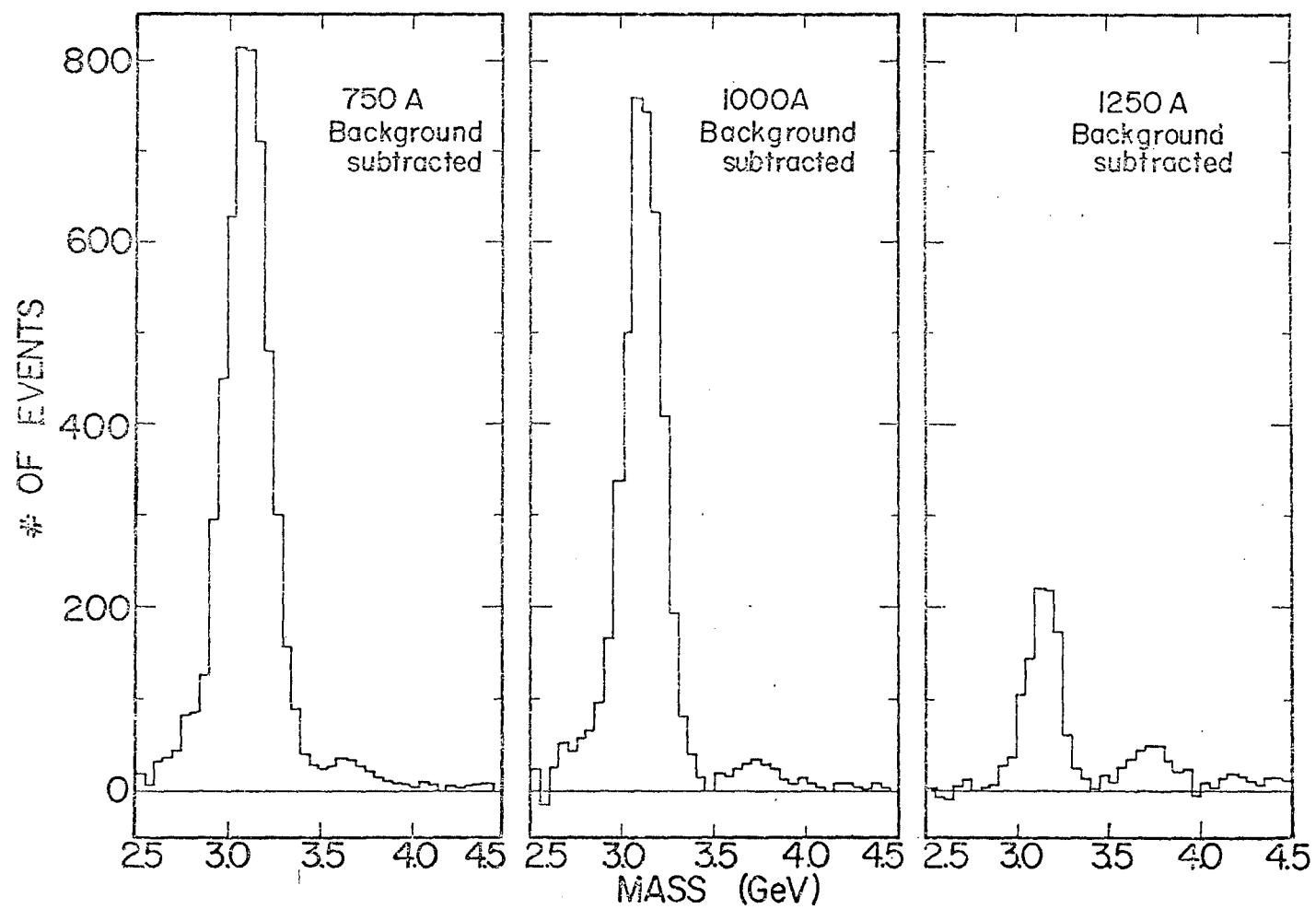
The expected mass resolution can be computed more exactly using the events themselves, since then the distribution of events in the apparatus and the chamber inefficiencies are taken correctly into account. The analysis program propagates errors through the track reconstruction and mass calculation, yielding the expected mass error for each event. The points shown in Figure 11 represent the 1500A mass resolution thus computed averaged over 1 GeV mass intervals. It is seen to agree with the analytic calculation given above within 5%.

We verify that these resolution calculations are correct using the  $J/\psi$ . For this purpose, we took special runs at air magnet currents of 750, 1000, and 1250A, since the  $J/\psi$  has too low a mass to be accepted significantly into the spectrometer at a current of 1500A. These runs used beryllium as the first foot of absorber. The mass distributions are shown in Figure 12. Table V compares the calculated mass resolution with the observed width of the  $J/\psi$ . The agreement is good at all three currents.



MASS RESOLUTION AND ITS COMPONENTS VS. MASS

FIGURE 11



MASS DISTRIBUTIONS FROM LOW CURRENT RUNS

FIGURE 12

TABLE V  
J/ $\psi$  Resolution

Current (A)	Predicted (GeV, FWHM)	Observed
750	0.275	0.277
1000	0.227	0.251
1250	0.195	0.204

### III. DATA ACQUISITION

Figure 13 is a block diagram of the data acquisition system. I now describe each component of the system in turn.

#### A. Fast Trigger Logic

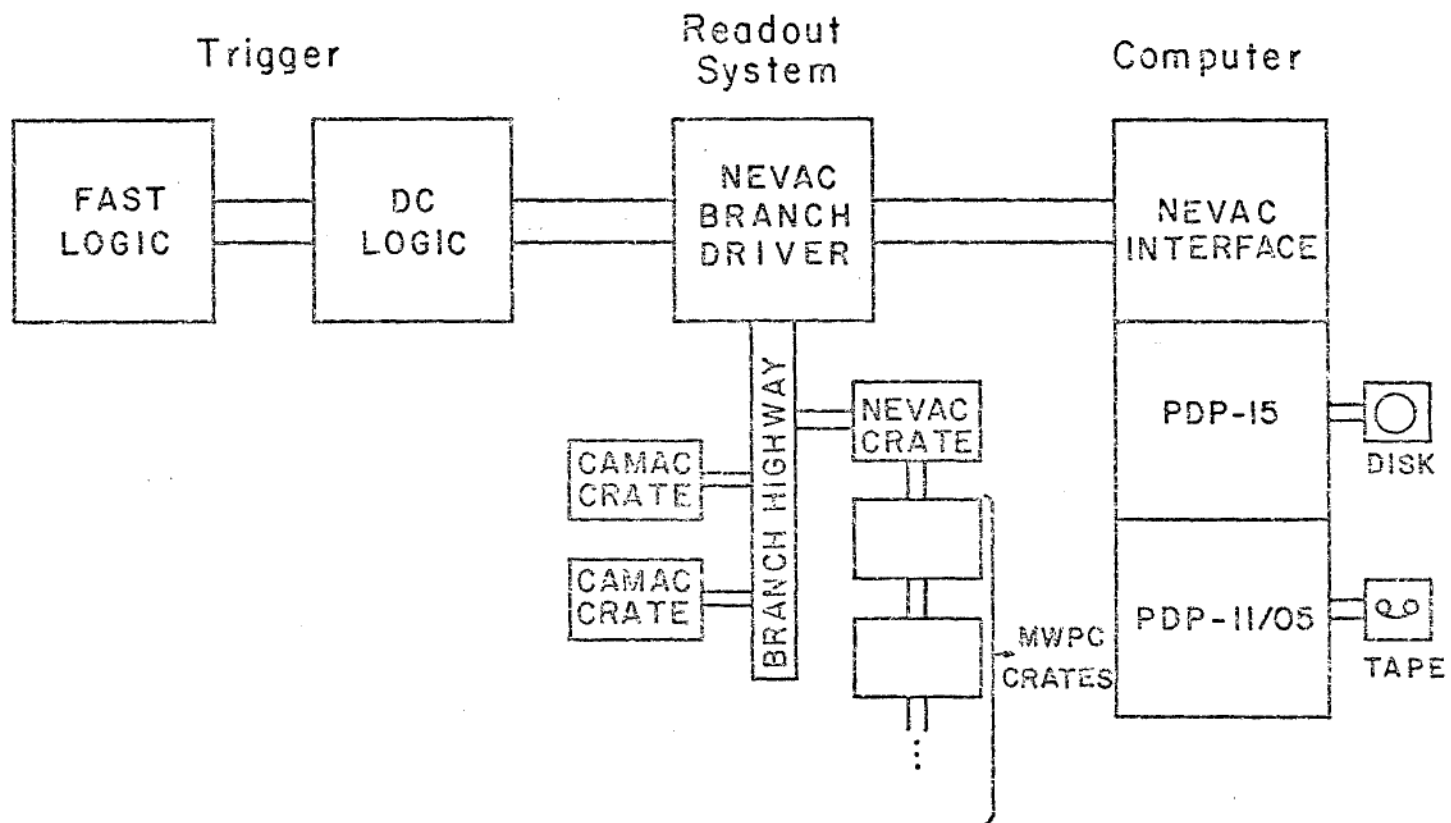
Figure 14 is a diagram of the fast logic. The first stage triggering decision was made by a LeCroy model 380 Multiplicity Logic Unit for each arm, set to require four out of five of H1, C, H2, H3, and V4. This crudely defines a track traversing the entire length of the arm. This signal was called T:

$$T = (H1, C, H2, H3, V4) \text{ 4/5}$$

We used a multiplicity trigger rather than a coincidence of all five counters so that events could be recorded in which one of the counters failed to fire, allowing us to monitor the efficiencies of the trigger counters. The LeCroy 380 can operate at input rates of 100 MHz and output rates up to about 50 MHz, hence the name fast logic. Typical T rates were 100 kHz; individual trigger counter rates ranged from 0.5 to 5 MHz.

The loose muon pair trigger was formed from the T signals of both arms by a LeCroy 364 Majority Logic Unit (which is capable of 150 MHz operation) set to two-fold coincidence:

$$TUD = TU \cdot TD$$



BLOCK DIAGRAM OF DATA ACQUISITION SYSTEM

FIGURE 13

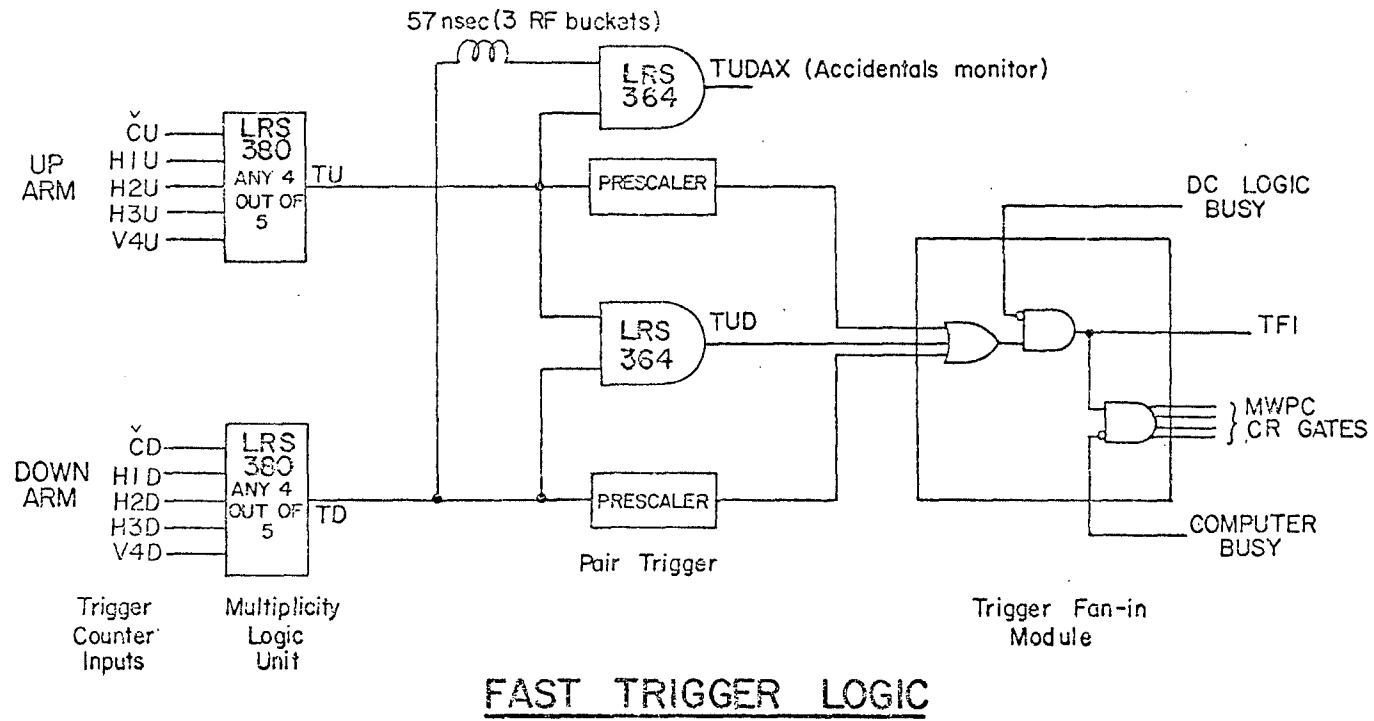


FIGURE 14



Also formed was the out-of-time coincidence

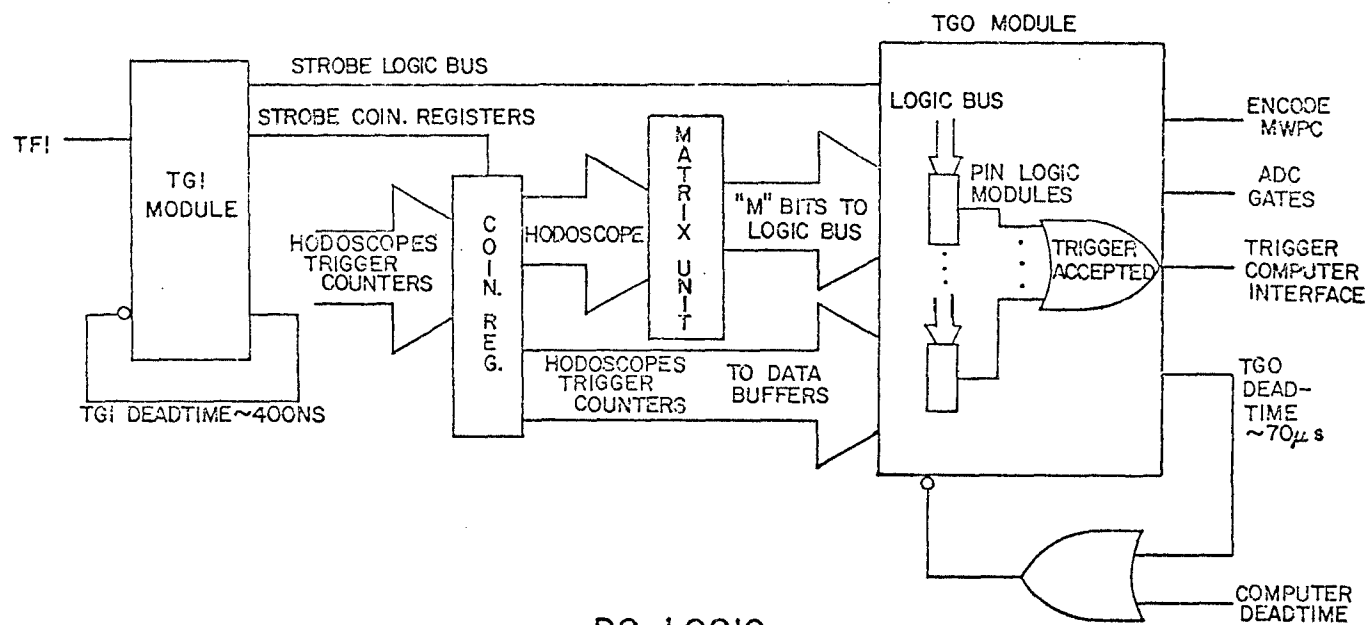
$$\text{TUDAX} = \text{TU} \cdot \text{TD delayed}$$

used to monitor accidental coincidence rates; TD delayed was delayed by 57 nsec (three accelerator RF buckets) relative to TU by the insertion of extra cable. The TUD rate was about 1 kHz, the TUDAX rate roughly half that. The TUD rate was dominated by accidental two-arm coincidences. It counted more than TUDAX because the RF buckets did not all contain the same number of protons; rather, occasional buckets containing several times more than the average made the probability of generating a TUD higher than the probability of generating a TUDAX. TUD and TUDAX together enabled us to monitor the RF structure of the beam, and TUDAX together with TU and TD enabled monitoring of beam structure on a slower time scale. We used this information to pester the accelerator operations crew whenever beam structure became unusually uneven, since uneven beam structure increased our trigger rate and deadtime drastically and tended to cause spurious hits in the chambers and hodoscopes. —

The TU and TD signals prescaled by 128 and the TUD signal went to the Trigger Fan In (TFI) module, which generated gates for the MWPC coincidence registers (CR's) and triggered the DC logic.

#### B. DC Logic

The DC logic (Figure 15) was a sophisticated and flexible



## DC LOGIC

FIGURE 15

general-purpose triggering system designed by H. Cunitz and W. Sippach at Columbia University's Nevis Laboratories. Input signals were strobed by the TFI signal and latched, so that further processing could be done with DC levels without worrying about timing. Two 16-bit "logic bus" crates containing logic modules had these DC signals bussed along their backplanes and available to every module. Each module formed the "and" of any of the 16 bus signals or their complements (selectable by the insertion of jumpers) as well as an optional input signal from some other module. The outputs included a "trigger" signal and complementary logic signals which could be connected to other logic module inputs, as well as an "inhibit" input for prescaling and scaler outputs with and without deadtime. The DC logic could be run with as little as 100 nsec deadtime per TFI, but since our TFI rate was so low we set it to 400 nsec to simplify timing and to cover deadtimes in the readout system.

The TFI signal from the fast logic came to the Trigger Generator Input (TGI) module which strobed the logic bus and hodoscope CR's and started the DC logic decision cycle. A "matrix unit" for each arm was used to discriminate against tracks originating upstream of the target in vacuum windows etc. or downstream in the shielding. It looked for pairs of hodoscope elements of the form  $(V1_i, V4_j)$  which lay near the diagonal of the  $V1-V4$  matrix (if no such pair of elements fired the

the track did not point back to the target) and set a logic bus bit (called M) if one was found. 250 nsec after TFI (to allow time for the hodoscope signals to arrive and the matrix unit to process them) the TFI module strobed the logic modules and the final trigger decision was made. If the DC logic criteria were not met, the MWPC CR's were reset and at the end of the 400 nsec DC logic deadtime another TFI could be accepted. If some logic module's criteria were satisfied, it sent a signal to the Trigger Store module (which recorded which triggers fired) and the Trigger Generator Output (TGO) module which did several things: it sent a READ pulse to the MWPC readout system to block the reset pulse and hold the MWPC data in the CR's, strobed the hodoscope, logic bus, and other data buffers, gated the ADC's (analog to digital converters), and, after a 50  $\mu$ sec deadtime to cover the ADC conversion time, triggered the branch driver to read out the event and interrupt the computer. There ensued a 20  $\mu$ sec deadtime to ensure that no additional TGO's could be generated before the readout process began. During the readout process the DC logic continued to cycle, allowing events satisfying DC logic requirements to be scaled independently of readout deadtime and providing a monitor of the number of triggers missed during the readout process.

We used the DC logic to implement one main muon pair trigger (called SINK) and four study triggers, two pair and two single-arm, defined as follows (U stands for up arm, D for down

arm, UD for the two-arm coincidence):

$$\text{SINK} = (\text{T} \cdot \text{H1} \cdot \text{H2} \cdot \text{H3} \cdot \text{V2} \cdot \text{M}) \text{UD}$$

$$\text{THUD} = (\text{T} \cdot \text{H1} \cdot \text{H2}) \text{UD}$$

$$\text{TUD} = \text{TU} \cdot \text{TD}$$

$$\text{STU} = (\text{T} \cdot \text{H1} \cdot \text{H2} \cdot \text{H3} \cdot \text{V2} \cdot \text{M}) \text{U}$$

$$\text{STD} = (\text{T} \cdot \text{H1} \cdot \text{H2} \cdot \text{H3} \cdot \text{V2} \cdot \text{M}) \text{D}$$

After much of the data had been taken (after run 838) a fifth study trigger (TVUD) was implemented and the other triggers were modified to include the newly installed H0:

$$\text{TVUD} = (\text{T} \cdot \text{H0} \cdot \text{V2} \cdot \text{V3} \cdot \text{C} \cdot \text{M}) \text{UD}$$

$$\text{SINK} = (\text{T} \cdot \text{H0} \cdot \text{H1} \cdot \text{H2} \cdot \text{H3} \cdot \text{V2} \cdot \text{M}) \text{UD}$$

$$\text{THUD} = (\text{T} \cdot \text{H1} \cdot \text{H2} \cdot \text{V3} \cdot \text{C}) \text{UD}$$

$$\text{STU} = (\text{T} \cdot \text{H0} \cdot \text{H1} \cdot \text{H2} \cdot \text{H3} \cdot \text{V2} \cdot \text{M}) \text{U}$$

$$\text{STD} = (\text{T} \cdot \text{H0} \cdot \text{H1} \cdot \text{H2} \cdot \text{H3} \cdot \text{V2} \cdot \text{M}) \text{D}$$

All the triggers but SINK were prescaled by factors ranging from 4 to 128 so that SINK represented roughly half of the triggers recorded on tape. The three pair triggers SINK, THUD, and TVUD (along with the "4/5" T trigger) allowed efficiency monitoring of every trigger counter; no counter was required by all three. The looser TUD trigger turned out not to be as useful because it had to be prescaled by 128 and so relatively few good TUD events were

recorded.

### C. Readout System

Like the DC logic, most of our readout system was designed by H. Cunitz and W. Sippach. It utilized the Nevis Labs version of CAMAC<sup>31</sup>, called NEVAC. NEVAC is capable of 2 MHz operation but in our system was limited to one word transferred per three  $\mu$ sec, corresponding to one out of every three computer memory cycles.

Our system consisted of a NEVAC branch driver, one NEVAC crate, two standard CAMAC crates, and nine MWPC crates. The NEVAC crate contained five 16-bit data buffers, the MWPC and hodoscope interfaces, a computer-controlled pulse generator, and a diagnostic display module. The data buffers were used to record the logic bus (32 bits) and Trigger Store module (8 bits), with the remaining 40 bits available for miscellaneous information. The MWPC interface read out wire addresses from the nine MWPC crates and the hodoscope interface read out hodoscope addresses from the hodoscope data buffers in the DC logic rack.

Of the two CAMAC crates, one contained 19 Jorway model 84 and 85 quad 125 MHz blind scalars, a diagnostic display module, and a Jorway model J001 Manual Input-Output module (switch register) used diagnostically. The other contained a LeCroy 2249A 12-fold ADC, an FNAL REsearch Services DVM (digital voltmeter) control module, and a Jorway 72A Visual Display module used to display the

blind scalers on a television monitor. The blind scalers were read out at the end of each accelerator pulse and contained information for beam flux, efficiency, and accidentals rate monitoring. The 12-fold ADC was read out for each event; it digitized the Cerenkov counter pulse heights. The DVM control unit was used sporadically to monitor the high voltage power supplies for the hodoscope and trigger counters.

The NEVAC branch driver performed the readout operation without computer intervention under control of a RAM (random-access memory) program preset by the computer. It was capable of handling up to four different types of triggers, performing a different readout sequence for each type; we used two types of triggers, one (the event trigger) generated by the DC logic for each event, the other (the scaler trigger) generated after the beam spill by a timing module. On receipt of a trigger, the branch driver would execute the appropriate section of its RAM program, writing data directly to the computer's core memory using cycle-stealing memory access, then interrupt the computer. Deadtime lasted from the receipt of the trigger until the computer finished processing the event and re-enabled the branch driver. The basic NEVAC word length is 16 bits, however the branch driver could also read out 8-bit or 24-bit data, packing it into 16-bit words before transferring it to the computer. In addition to the triggered pre-programmed readout mode, the branch driver could be operated under direct computer control or manually using front-panel

switches and push-buttons. It could also be cycled or "single-cycled" off line from the computer for debugging.

#### D. Computer and On-Line Program

Our on-line computer was a Digital Equipment Corporation Unichannel 15, consisting of a PDP-15 with a small PDP-11/05 used as a peripheral device controller. The PDP-15 had 32k words of core memory, floating point and automatic priority interrupt hardware, three DECtape drives, a storage scope display, an RF15 256k-word fixed-head disk, and an interface to the NEVAC branch driver. The PDP-11/05 had 8k words of core memory (and could access 16k of PDP-15 memory), an RK05 1.2M-word floating-head disk, a line printer and a TU10 magnetic tape drive.

During the beam spill, events were written into three 1500-word PDP-15 core buffers by the branch driver, whence the on-line program copied them onto the RF15 disk whenever a buffer was filled. Advantage was taken of the priority interrupt hardware to minimize the software event processing time. Multiple core buffers were used to allow simultaneous input from the branch driver and output to the disk, thus disk writing deadtime was negligible at low to moderate trigger rates (say  $< 50$  events/sec). However, this led to our restricting the branch driver's access to memory to at most one out of every three memory cycles, to prevent the branch driver from blocking memory access by the disk controller. At our typical trigger rate of 100 Hz, disk writing



was nevertheless the dominant source of deadtime.

Between beam spills the on-line program copied events from the disk to magnetic tape and (in a second pass through the disk) performed a rough analysis of as many events as the accelerator's cycle time permitted. The primary purpose of this analysis was to ensure the proper functioning of the apparatus, including the trigger, readout system, trigger counters, hodoscopes, and MWPC's. Tallies were kept of the blind scalers, which were read out and reset at the end of each spill; certain scaled rates allowed monitoring of the quality of the beam (RF spill structure, slow spill structure, and proximity of amount of beam received to amount requested), and quality parameters for each beam spill were computed and displayed on Nixie-tube scalers via the NEVAC pulse generator module. At the end of each data run, a summary, including blind scaler totals, selected ratios of scaler totals to each other, efficiency summaries for all parts of the apparatus, and other miscellaneous information, was printed on the line printer. The program could also perform other services, such as measuring counter high voltages and ADC pedestals (at the user's option) at the start of each run, monitoring the current in the analyzing magnets, and, in response to user requests, defining histograms of various quantities (read out or computed), displaying histograms or run status information on the scope display or line printer, and changing the list of scaler ratios to be output in the end-of-run summary.

### E. Data Taking

Runs were generally one to two hours long. The proper functioning of the apparatus was monitored run by run by careful checking of the end-of-run summaries, and during the run aural and visual feedback were provided pulse by pulse: Nixie-tube scalers and the blind scaler TV monitor displayed various counting rates, TV monitors showed horizontal and vertical beam profiles upstream and downstream of our steering and focusing magnets, the on-line program displayed beam quality, and audible tones were sounded for each trigger and for each buffer written to magnetic tape. More sophisticated and complete apparatus monitoring was performed approximately daily by off-line analysis on the CDC 6600 of several data runs.

At intervals of several weeks, or whenever the position of the detectors might have been disturbed by work in the pit, we took special alignment runs for which the air magnets were turned off but the steel magnets operated at full current. We thus recorded large numbers of high momentum tracks passing straight through the apparatus, allowing the MWPC's to be aligned with each other and with the target. To cover the entire detector area with adequate statistics, roughly half of the events were taken with the (high-rate) small-angle V4 hodoscopes turned off. These runs allowed relative alignment of the chambers to 0.01".

Approximately 1000 hours of data were taken, at air

magnet currents of 750, 1000, 1250, and 1500A. The 1500A sample constituted the bulk of the data, and it is with it that this thesis is mainly concerned. Table VI describes the various 1500A data sets.

Table VI

## 1500A Data Sets

Target	Movable absorber	# incident protons	# hours
Pt	Cu	$4.57 \times 10^{16}$	450
Pt	Be	$5.77 \times 10^{15}$	60
Cu	Cu	$8.93 \times 10^{15}$	145
Cu	Be	$7.18 \times 10^{14}$	15
Be	Cu	$2.38 \times 10^{15}$	20

#### IV. DATA REDUCTION

The first stage of the analysis was known as compression. Its aim was to reduce some 300 data tapes to a manageable number in a reasonable amount of computer time. There were four levels of compression, called, A, C, D, and E. In the A level, a simple track finding algorithm was used to compute the invariant mass of the muon pair. Events failing this algorithm were eliminated, and events with reconstructed mass less than 3.8 GeV were prescaled. The number of events was thus reduced by a factor of 3.5. An additional factor of two in the number of tapes was gained by the use of the 1600 byte per inch recording density which was available on the CDC 6600 but not on our Unichannel 15. All subsequent analysis used the more complicated "standard" track reconstruction algorithm. To optimize the resolution, it included a least squares fit of the track to the measured points.

Subsequent levels of compression eliminated events failing the standard reconstruction algorithm or failing a progressively more stringent series of requirements which were intended to eliminate background events while retaining good efficiency for genuine massive muon pairs. These requirements fell into three categories: track quality cuts, fiducial cuts, and muon cuts.

Since the MWPC's were not expected to be 100% efficient, the reconstruction algorithm was designed to find tracks even if

some chambers were missing. The track quality cuts were then applied to weed out tracks resulting from the accidental lining up of unrelated chamber hits. They included requirements on the confidence level of the least squares fit and on the number of chambers participating in the track.

The fiducial cuts defined the sensitive volume of the experiment; since the trigger might accept muons not coming through the apertures of the shielding wall or air gap magnet, not originating in the target, or not traversing some of the detectors, such software definition of the sensitive volume was necessary. Cuts were made on the reconstructed positions at the target, shielding wall, air magnet, and at each detector plane. The fiducial cuts are listed in Table VII.

The muon cuts used information from the detectors behind the steel magnet to confirm the muon momentum as measured by the air magnet; non-muons having been suppressed by a factor of over  $10^8$  by the 18.5 hadronic absorption lengths of material in the target box, the major remaining background was low momentum muons appearing to have high momentum due to traversal of the air magnet along unorthodox paths. The reconstructed track was extrapolated through the steel magnet using the momentum measured in the air magnet. At each of 4Y, 5Y, H2, H3, V3, and V4, the distance of the extrapolated track from the nearest active hodoscope element or MWPC wire was computed and compared with the expected r.m.s.

Table VII

## Fiducial Cuts

Position	x limits (inches)		y limits (inches)	
Mag. entr.	-8.80	8.80	-5.00	5.00
Mag. exit	-11.80	11.80	-5.00	5.00
H1	-12.50	12.50	-5.90	5.90
JY	-12.25	12.25	-6.30	6.30
V1	-13.15	14.05	-7.50	7.50
Y1	-14.00	14.00	-7.56	7.56
Y2	-16.00	16.00	-11.34	11.34
V2	-18.63	19.13	-16.50	16.50
3Y	-18.00	18.00	-14.17	14.17
H2	-19.00	19.00	-17.00	17.00
Y4	-22.50	22.50	-16.54	16.54
V3	-24.13	24.13	-16.50	16.50
Y5	-27.00	27.00	-17.00	17.00
V4	-27.00	27.00	-16.50	16.50
H3	-28.00	28.00	-17.00	17.00

deviation due to multiple scattering in the steel (and MWPC measuring error in the case of 4Y and 5Y). If the distance was less than three standard deviations the cut was passed. Events were required to pass five out of the six muon cuts. The complete set of cuts as applied to the final sample of events is listed in Table VIII. The cuts applied and the resulting compression factor at each level of compression are given in Table IX.

The final stage of compression was the writing of a "data summary tape" (DST) of events from the E level compressed tape. On the DST only those events were kept which satisfied fairly stringent cuts, and a great saving of computer time and of event size was engendered by writing the results of the reconstruction instead of the "raw" event information. The DST was thus small enough to be stored as a disk file. This was a great convenience, as disk jobs had much better turnaround on the CDC 6600 than tape jobs. In addition to the variables of physical interest (mass, transverse momentum, rapidity, production and decay angles) and the track parameters in each arm, logical flags were recorded which indicated the charge of each muon, which detector planes participated in the track, which muon cuts were satisfied, and which trigger bits were set. The final event sample included events missing up to two chambers and failing any one muon cut, so the efficiency of each chamber and each muon cut could be determined. Events satisfying the study triggers but failing the SINK trigger allowed determination of the trigger efficiency.



Table VIII

## Sample Selection Requirements

1. 1 track found in each arm
2.  $\geq 6$  chambers participating in each track
3. Track confidence level cut:
  - If 6 chamber track C.L.  $\geq 0.021$
  - If 7 chamber track C.L.  $\geq 0.011$
  - If 8 chamber track C.L.  $\geq 0.001$
4. Fiducial cuts
5. Muon cuts:  $\geq 5$  out of (4Y, 5Y, H2, H3, V3, V4)  
within  $3\sigma$  of extrapolated track
6. Target cut: projected horizontal position at target  
 $\leq 0.3" + 20 / p$

TABLE IX

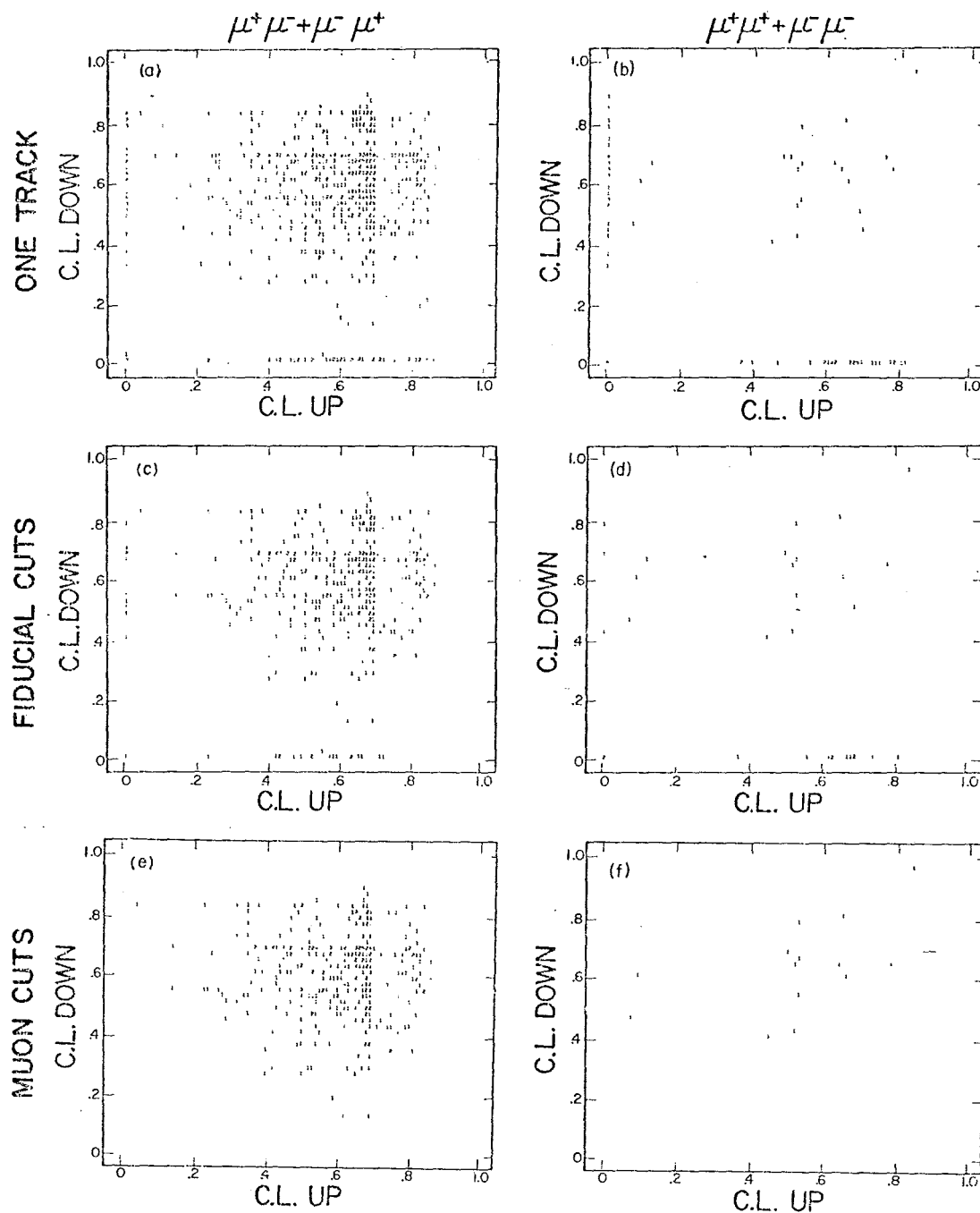
## LEVELS OF COMPRESSION

LEVEL	REQUIREMENTS	COMMENTS	COMPR. FACTOR
A	Crude Reconstr. prescale $m < 3.8$	800 BPI to 1600 BPI	7
C	Standard reconstr. # chamb. $> 6$ $y_{\max} < 5.4$		5
D	$m > 4.8$ , $CL > 10^{-5}$ if 6 chamb.	Scalers to 25 words	3
E	$y_{\max} < 5.2''$ , 4Y or 5Y within $3\sigma$	Scalers to 7 words	3

## V. RESULTS

### A. Backgrounds

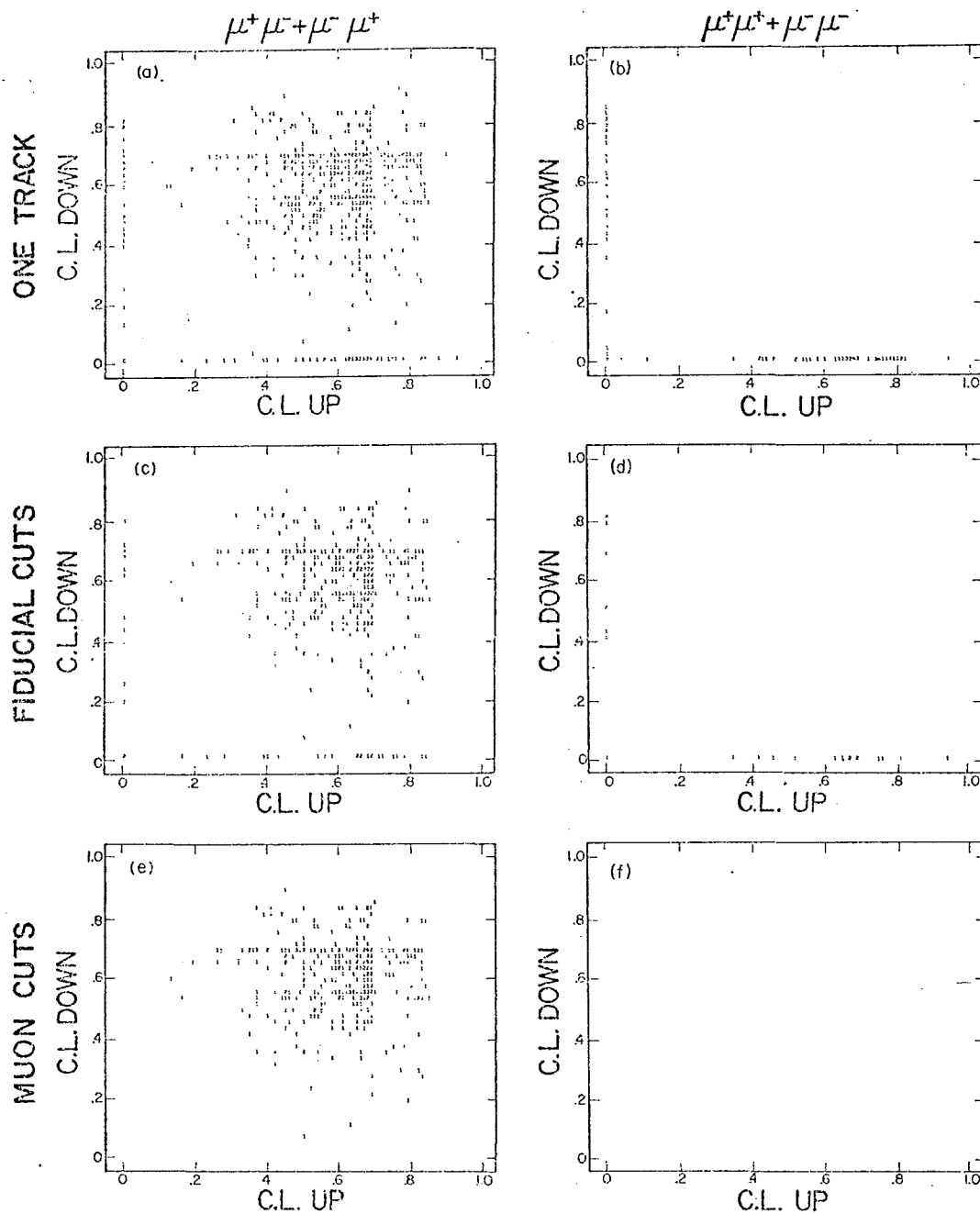
Observed muons are of two types: scattered low momentum muons emerging from the air magnet along trajectories appropriate to high momentum ("mismeasured" muons) and correctly measured high momentum muons. To study backgrounds due to mismeasured muons, a confidence level was computed for the muon criteria in each arm as follows: the deviations (normalized to the expected standard deviation) at each of 4Y, 5Y, H2, H3, V3, and V4 were summed in quadrature to form a  $\chi^2$ . Since only five out of six of the muon cuts were required, if all six detectors fired the worst one was omitted from the sum. For 4Y and 5Y the standard deviation included the measuring error. For H2, H3, V3, and V4, if the extrapolated track intersected an active hodoscope element, the sum was incremented by one, while if the track did not intersect an active hodoscope element, the squared deviation from the edge of the nearest active element was used. This distorts the resulting confidence level distribution so that it is not uniformly distributed, but it is still useful for the background study, Figures 16, 17 and 18 display distributions of events from a C level compressed tape in three mass regions versus the muon criteria confidence levels in the two arms. Shown are neutral and doubly charged events satisfying three successive levels of cuts. In each figure, a and b show events having one reconstructed track in each



MUON CRITERIA CONFIDENCE LEVEL

$$5\text{GeV} \leq M_{\mu\mu} \leq 7\text{GeV}$$

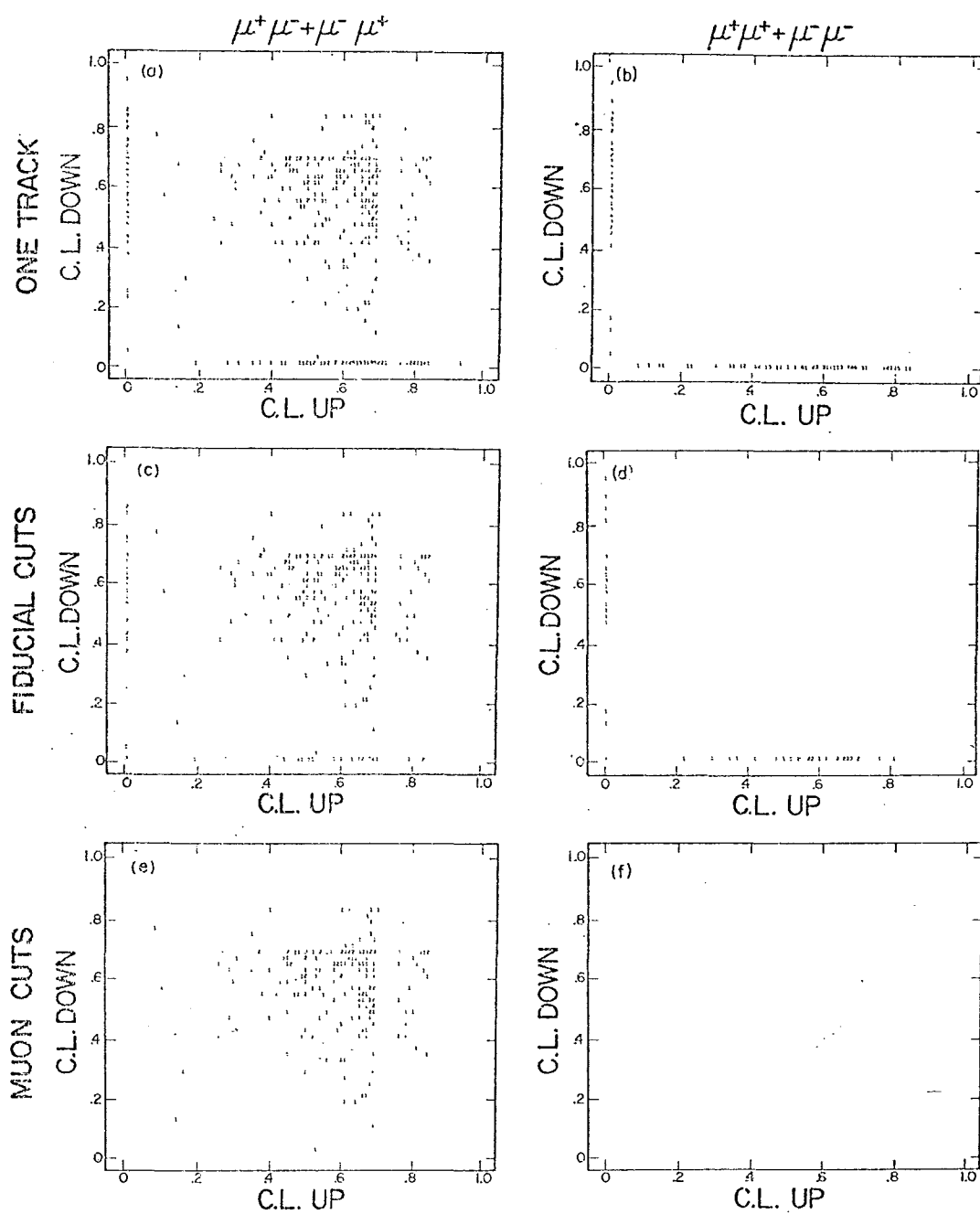
FIGURE 16



MUON CRITERIA CONFIDENCE LEVEL

$$7\text{GeV} \leq M_{\mu\mu} \leq 9\text{GeV}$$

FIGURE 17



MUON CRITERIA CONFIDENCE LEVEL

$$M_{\mu\mu} > 9\text{GeV}$$

FIGURE 18

arm, c and d show events also passing fiducial cuts, and e and f show events passing the standard analysis cuts of Table VIII. The mismeasured muon background is evident along the left and lower edges of the plots and is seen to be well separated from the bulk of events and to be entirely eliminated by the standard cuts. These results are summarized more quantitatively in Table X. Note that at high mass the doubly charged events all turn out to be mismeasured.

That the events having small muon criteria confidence levels are indeed scattered low momentum events can be seen using the MM chambers. The measured muon trajectory after the air magnet determines the momentum and the extrapolated position half way through the magnet. A low momentum muon which scatters off the magnet steel or penetrates the coils and emerges along a high momentum trajectory will usually be at the wrong place half way through the magnet. The vertical distance of the extrapolated position from the nearest active MM wire is thus an indication whether or not the muon momentum was correctly measured.

Figure 19 shows distributions of events from a C level compressed tape on a plot of MM miss distance versus muon criteria confidence level, for each arm and for three mass bins. At small confidence level the distribution of miss distances is quite broad, as expected.

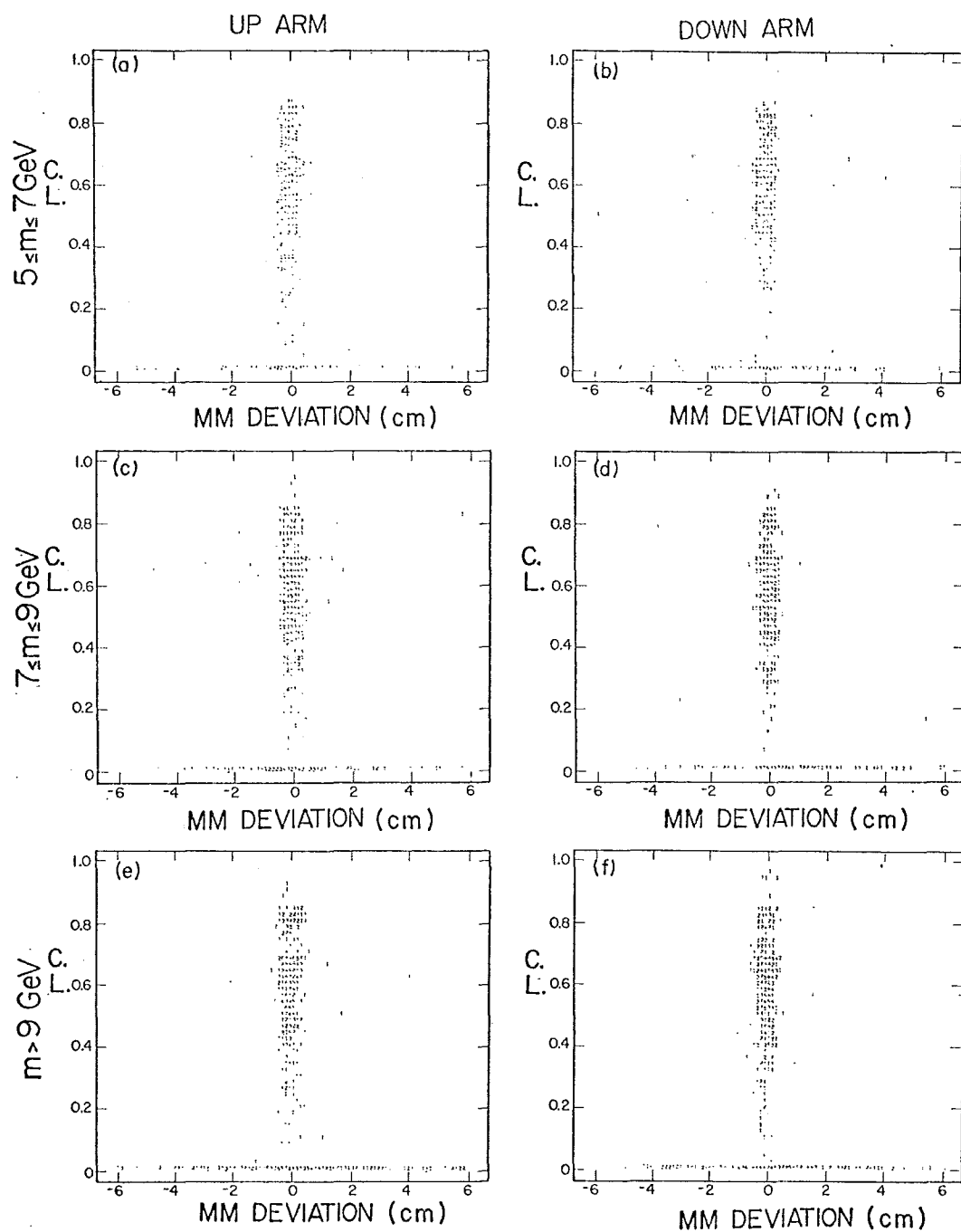
Backgrounds of correctly measured muon pairs can arise in

Table X

Effect of Successive Cuts  
on Number of Events

Mass bin:	5 to 7		7 to 9		>9 GeV	
Charge:	0	2	0	2	0	2
1 track	640	93	622	98	438	185
Fid. cuts	387	32	400	23	267	58
All cuts	327	14	330	0	185	0
95% CL upper limit on background:	.60%		.59%		1.05%	





CONFIDENCE LEVEL VS. MM DEVIATION

FIGURE 19

various ways, most of which are straightforwardly monitored by the doubly charged events. Single muons can be produced by decay of known hadrons or perhaps "directly" by unknown processes. They can give rise to pairs through accidental coincidence or through correlated pair production. If muons and antimuons are produced equally then accidental coincidence will give doubly charged events as often as neutral. If muon and antimuon rates are not equal, the  $\mu^+\mu^-$  rate is the geometric mean of  $\mu^+\mu^+$  and  $\mu^-\mu^-$ , i.e.

$$\mu^+\mu^- = \mu^-\mu^+ = \sqrt{(\mu^+\mu^+)(\mu^-\mu^-)} \quad (1)$$

If the hadronic pair correlation function

$$R \equiv \frac{E_1 E_2 \frac{d^6\sigma}{dp^3 dp^3}}{\frac{1}{E_1 \frac{d^3\sigma}{dp^3}} \frac{2}{E_2 \frac{d^3\sigma}{dp^3}}} \sigma_T$$

satisfies

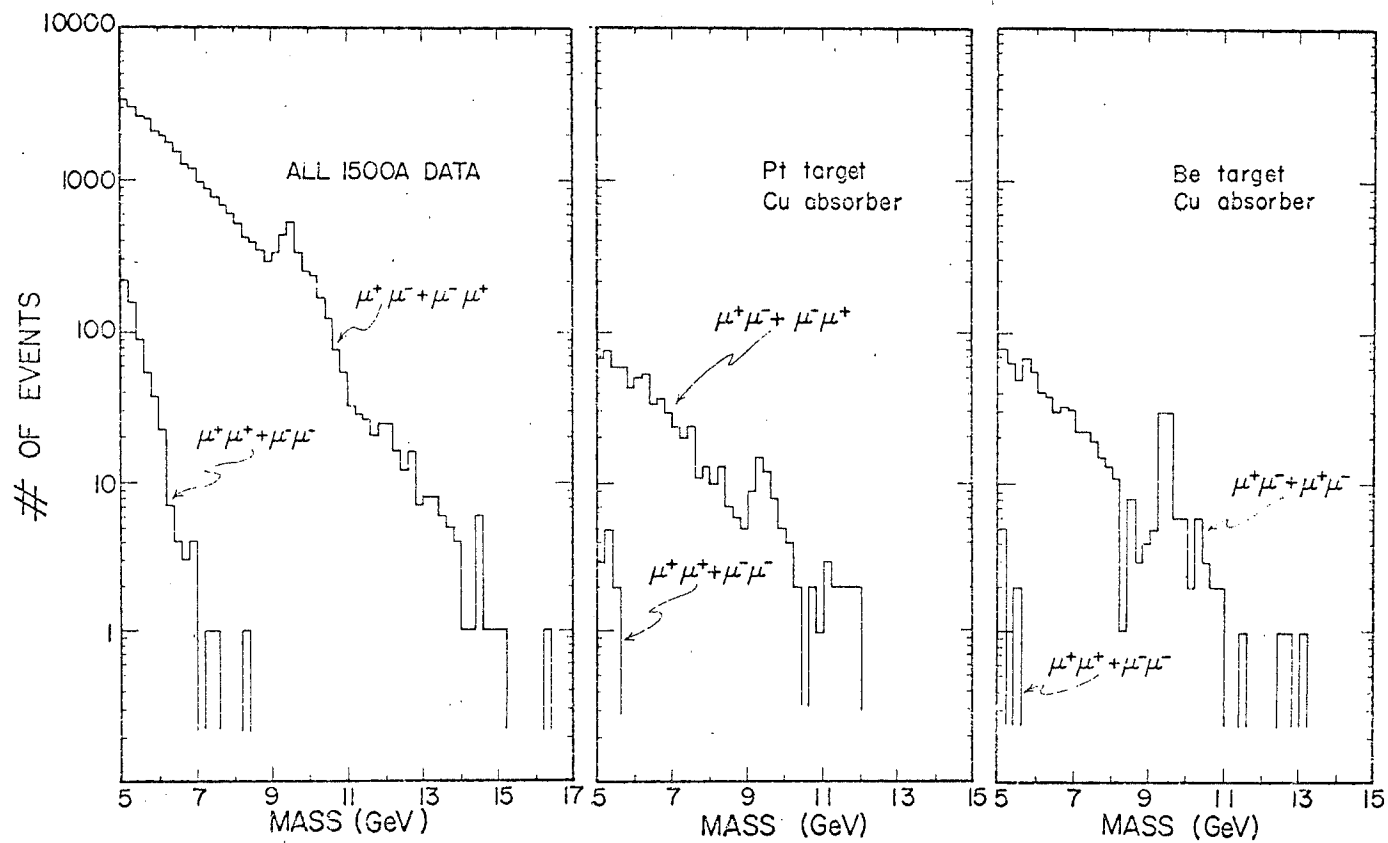
$$R_{+-} = \sqrt{R_{++} R_{--}}$$

then the correlated hadronic decay background also satisfies (1) above. The CFS hadron pair experiment<sup>28</sup> showed this to be true within

50% in the mass range from 4 to 8 GeV. A remaining possible source of background is the correlated production of a hadron and a direct muon, about which little is known; one such mechanism might be production of a pair of charmed mesons followed by semileptonic decay of one of them, which however is likely to be small and may also satisfy (1) above. Correlated production of a pair of direct muons might or might not be considered a source of background; any component not due to the decay of a single parent (virtual photon or resonance) is not the signal of interest. Such a background might arise from pair production and semileptonic decay of charmed mesons, but this is again likely to be small and may also satisfy Equation (1).

The observed  $\mu^+\mu^+$  and  $\mu^-\mu^-$  rates are equal within 30%, so that the geometric mean of (1) above is equal to the average within 1%. In practice we therefore subtracted the doubly charged events from the neutral events, except for a correction which is discussed below. Figure 20 shows mass spectra for the complete data sample and two subsamples after application of the cuts of Table VIII. We see that the doubly charged events are at worst (in the mass bin from 5.0 to 5.2 GeV) less than 6% of the neutral data and are completely negligible above 6 GeV.

The background subtraction is complicated by an acceptance



MASS DISTRIBUTIONS AT 1500A

FIGURE 20

effect. The acceptance for doubly charged events is not the same as the acceptance for neutral events; this can be seen as follows: Consider a pair of muons, one in each arm, each of which is near the top of its aperture. If they are of the same charge, half the time they will both be deflected into the aperture and half the time they will both be deflected out. However, if they are of opposite charge, one of them will always be deflected out, so the event is never accepted. At a mass of 5 GeV, this event has about a GeV of vertical transverse momentum. Now consider an event in which one muon is near the top and the other muon is near the bottom of its aperture. This time one of the muons is always deflected out if the charges are the same, while if the charges are opposite half the time both muons are deflected in. On the average, this event has no vertical momentum. Thus we see that the ratio of same charge to opposite charge pair acceptance is larger at large transverse momentum than at small transverse momentum. This means that a straight subtraction of the doubly charged events from the neutral events will bias the observed transverse momentum distribution at low mass.

There is a procedure which corrects exactly for the different acceptances if the background is entirely accidental, and which corrects approximately even if a substantial fraction is due to correlated hadron pair production. Assume first that all of the background is due to accidental coincidence. Then for

each accepted doubly charged event in which both muons are near the top of the aperture, there is another event produced with the same cross-section which isn't accepted because one muon is at the bottom of the aperture. For each accepted neutral accidental pair of which one muon is near the top and the other near the bottom of the aperture, there is another event produced with the same cross-section which isn't accepted because both muons are at the top or at the bottom of the aperture. Evidently we can obtain the spectrum of neutral accidental events from the spectrum of doubly charged accidental events by reflecting the trajectory of one muon through the median plane; the reflected event will have the same mass, transverse momentum, rapidity, and acceptance as the neutral event of the same topology. (Another way of saying this is that our single-arm acceptance is invariant under CP, not surprising since it is electromagnetic in nature.)

The reflection procedure works for accidentals because the production cross-section of accidentals is the product of the two single muon cross-sections, and reflecting a muon changes its azimuth but not its cross-section, since the cross-section is independent of azimuth. The procedure does not work exactly for muons from the decay of correlated hadron pairs since the correlation function  $R$  depends on the mass and transverse momentum of the pair<sup>28</sup>, both of which change when the muon is reflected. Fortunately this dependence is not very strong, and because our

vertical aperture is small the mass and transverse momentum do not change very much. Thus the doubly charged events can all be treated as accidentals with negligible error.

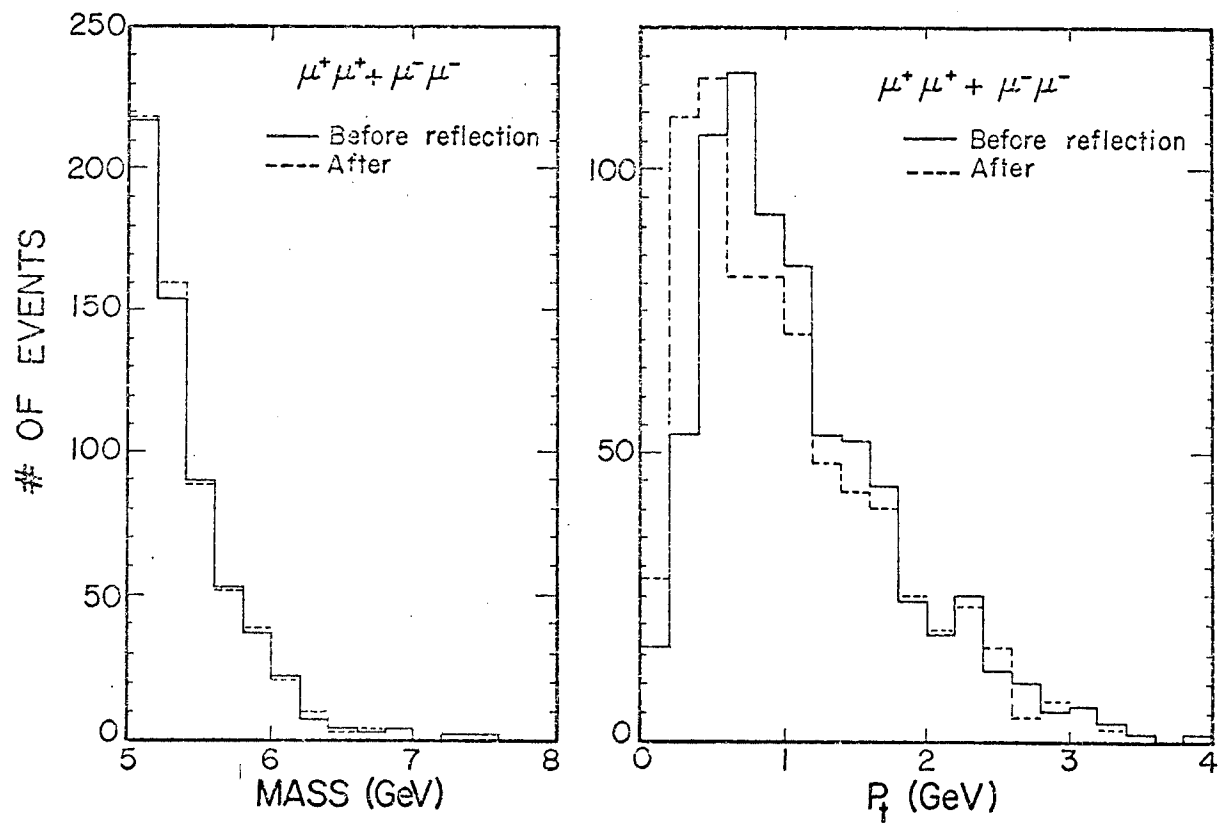
Figure 21 shows the effect of the reflection on the mass and transverse momentum distributions of the doubly charged events. The subtraction is increased by a factor of 2 at small transverse momentum but remains unchanged at large transverse momentum. There is little effect on the mass distribution.

Out of conservatism, I assign an error of  $\pm 50\%$  to the background subtraction, since the doubly charged events might be of correlated hadronic origin and, as discussed above, the correlation is not perfectly known.

#### B. Normalization

To convert these spectra to differential cross-sections, we need to know the apparatus acceptance and efficiency and the total flux of incident protons. The acceptance is the fraction of muon pairs emerging from the target which traverse the spectrometer; it is determined by the spectrometer geometry. The efficiency is the fraction of pairs traversing the spectrometer which trigger the computer and pass the various analysis cuts. The differential cross-section in a bin  $\Delta m$ ,  $\Delta y$  of mass and rapidity is then given by

$$\frac{d^2\sigma}{dm dy} \approx \frac{\Delta\sigma}{\Delta m \Delta y} = \frac{N_{ev}}{N_{inc}} \frac{A}{N_o \rho L_{eff}} \frac{1}{\epsilon \eta} \frac{1}{\Delta m \Delta y} \quad (2)$$



EFFECT OF REFLECTION ON MASS AND  $p_t$  DISTRIBUTIONS

FIGURE 21



where  $N_{ev}$  = number of events in the bin  $\Delta m, \Delta y$   
 $N_{inc}$  = number of incident protons  
 $A, \rho, L_{eff}$  = atomic weight, density, effective  
length of target  
 $N_0$  = Avogadro's number  
 $\epsilon$  = efficiency  
 $\eta$  = acceptance in the bin  $\Delta m, \Delta y$ .

The effective length of the target is the length corrected for absorption of the incident beam; it is thus given by

$$L_{eff} = \lambda(1 - e^{-L/\lambda})$$

where  $\lambda$  = hadronic absorption length of target material  
 $L$  = length of target

### 1. SEM Calibration

The number of incident protons was measured by a secondary emission monitor (SEM). The SEM was calibrated by inserting copper foils into the beam line and measuring the yield of  $^{24}\text{Na}$  per SEM count. Using a  $^{24}\text{Na}$  production cross-section of 3.5 mb per Cu nucleus<sup>32</sup>, the SEM calibration constant was found to be  $(1.01 \pm 0.02) \times 10^8$  protons per SEM count.

### 2. A-dependence

Equation (2) gives the cross-section per atomic nucleus of target material. To get the cross-section per nucleon we might

divide by  $A$ , but this is not necessarily the cross-section that would be observed on hydrogen for three reasons: 1) our targets contain neutrons, 2) the target nucleons are not at rest within the target (discussed below), and 3) the cross-section might depend on  $A$  differently than linearly. Indeed an  $A$ -dependence given by  $\sigma \propto A^{2/3}$  would be expected (and has been observed<sup>33</sup>) for the bulk of hadronic scattering cross-sections; these are the "soft" collisions in which little momentum is transferred from the beam particle to the target particle. Such a dependence can be understood in terms of "shadowing" of nucleons inside the nucleus by nucleons on the surface: the incident hadron does not penetrate very far into the nucleus (note that a platinum nucleus is about 3 nuclear collision lengths thick) and so doesn't see the nucleons in the interior.

What has been said above implies that all hadronic scattering cross-sections should have an  $A^{2/3}$  dependence. However, faster  $A$ -dependences may occur if (as seems to be the case) hadrons have internal structure. Then some components of hadrons (the ones responsible for soft collisions) might interact before reaching the interior of the nucleus, while other components which interact less strongly might see all of the nucleons and interact with linear  $A$ -dependence. In the parton model, soft processes are due to the interaction of "wee" partons. Wee partons carry a tiny fraction of the momentum of their hadrons, so wee partons from the beam and target move slowly with respect to each other and interact with

large probability and  $A^{2/3}$  dependence. By contrast, particles of large transverse momentum and pairs of large mass are produced in collisions of "hard" partons, which carry significant fractions of the momenta of their hadrons. Hard partons from the beam and target move very rapidly with respect to each other in high energy collisions and so interact rarely. Their interactions should thus exhibit linear A-dependence.

Stronger than linear A-dependence has also been observed, both for the production of single hadrons at large  $P_t$ <sup>34,35</sup>, and for hadron pair production at large mass<sup>35</sup>. The mechanism or mechanisms responsible for this are not understood.

To investigate the A-dependence we took a set of data runs using both platinum and beryllium targets, switching targets every few runs. Since knowledge of the A-dependence is necessary in order to extrapolate to cross-section per nucleon, and since this analysis is independent of efficiency and acceptance, I present the results here before going on to discuss the efficiency and acceptance. We parametrize the A-dependence by the functional form

$$\sigma \propto A^\alpha$$

and determine the exponent  $\alpha$  according to the formula

$$\alpha = \ln \frac{\sigma_{Pt}}{\sigma_{Be}} / \ln \frac{A_{Pt}}{A_{Be}} \quad (3)$$

The relative normalization of the two data samples depends only on the amount of incident flux in each data sample and the targeting fractions for the Pt and Be targets. All other factors cancel since the two samples were taken with the same apparatus and during the same period of time (this cancellation will be verified below).

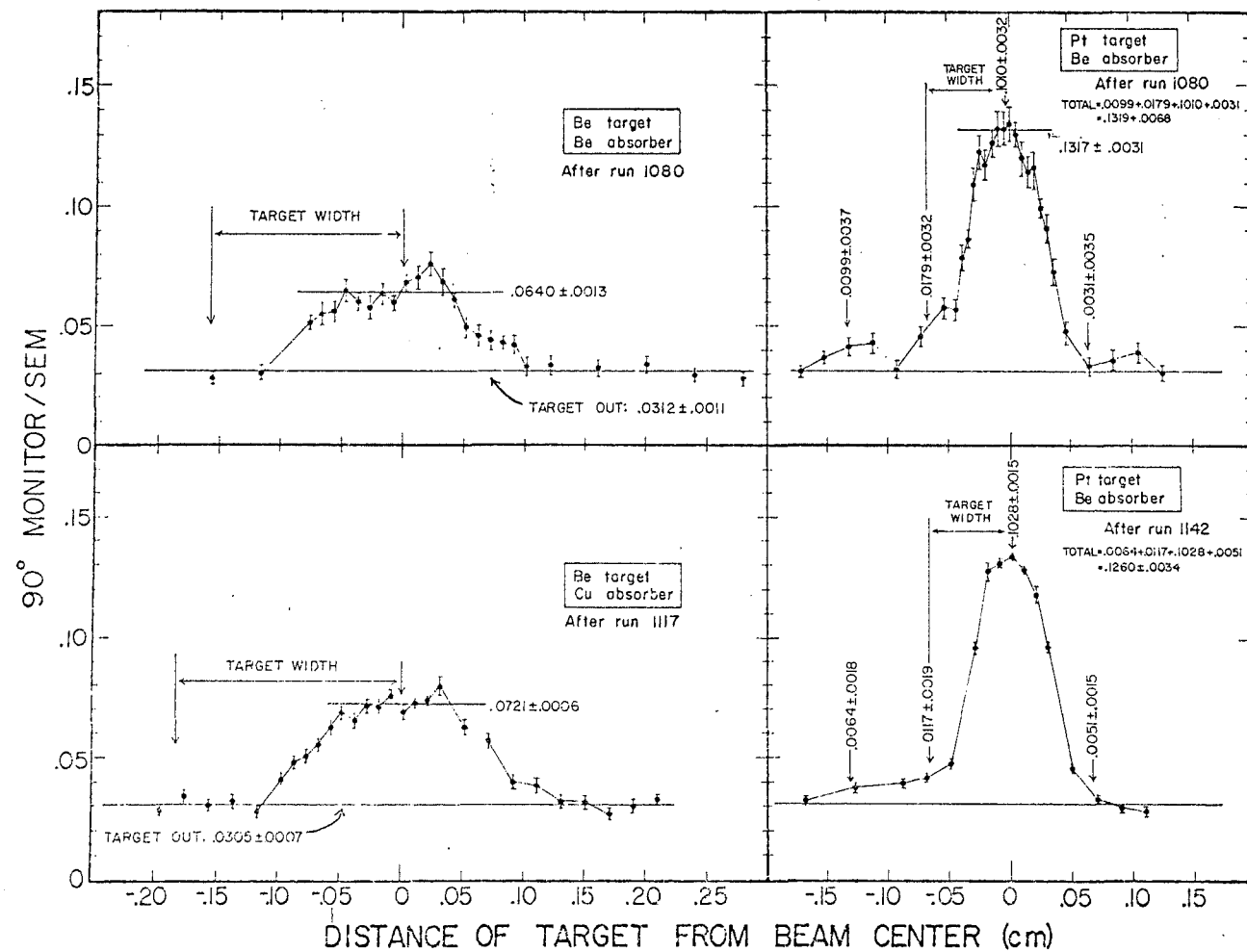
The incident flux was measured by the SEM. The flux factor for each data sample is (from Equation 2)  $N_{inc} \rho L_{eff}$ . The flux calculation is summarized in Table XI.

The targeting fraction of each target was determined by moving the target transversely to the beam and recording the  $90^\circ$  monitor and SEM readings for several beam pulses in each position. The resulting distributions are shown in Figure 22. There is seen to be a residual  $90^\circ$  monitor counting rate even when the target is completely out of the beam; this is due to particles produced in the beam dump reaching the  $90^\circ$  monitor and represents a background which must be subtracted. The two beryllium target scans (one taken with copper as the first foot of absorber and one with beryllium) determine the "target out" rate to be  $0.0307 \pm 0.0006$   $90^\circ$  monitor counts per SEM count. They also show that the "target in" part of the  $90^\circ$  monitor rate depends somewhat on which absorber is used, the ratio of copper absorber "target in" rate to beryllium absorber rate being  $1.24 \pm 0.06$ . The beryllium target is seen to be sufficiently wide that it intercepted all of the beam. However, the width of the platinum target was comparable to that of the

Table XI

## A-dependence Flux Calculation

	Pt target	Be target
SEM counts	12667101	23516602
90° mon counts	1808764	1698489
" live-time gated	1721082	1634927
Live time	.9515	.9626
Incident protons	$1.217 \times 10^{15}$	$2.286 \times 10^{15}$
Flux factor	$4.274 \times 10^{16}$	$3.793 \times 10^{16}$
Pt/Be flux ratio	1.126±.035	

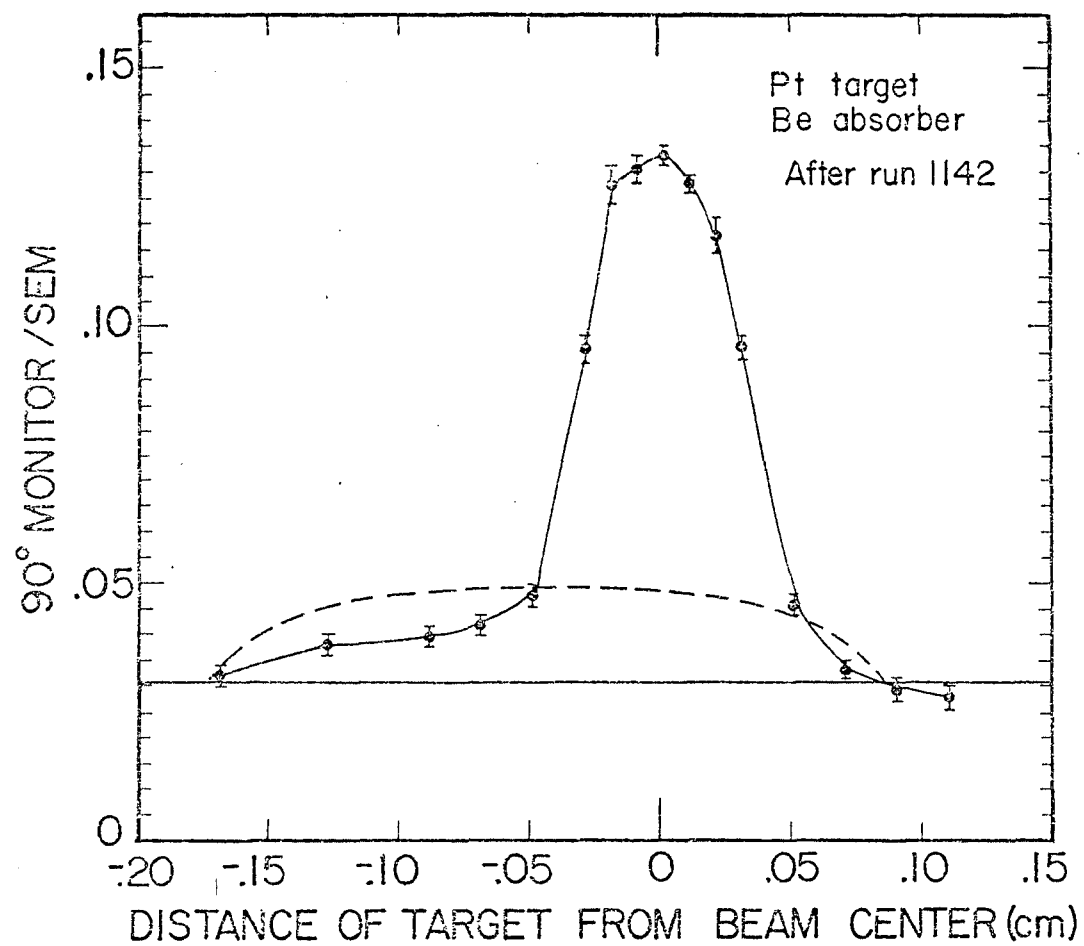


TARGET SCANS

FIGURE 22

beam, so the platinum targeting fraction depended on how well the beam was focused and varied from run to run.

The platinum target scans show substantial tails, especially to the left of the peak; these are not evident in the beryllium scans and so do not reflect the shape of the beam. Rather, they reflect the shape of the platinum target, which, as a result of the melting of the last 0.67 cm, had a large bead at the end of the intact portion. We can estimate the platinum targeting fraction by the following argument: If we were to assume (incorrectly) that the tails represented beam which missed the target in its normal position, the two platinum scans would determine the background-subtracted  $90^\circ$  monitor/SEM ratio for 100% targeting to be  $0.127 \pm 0.003$  with the beryllium absorber. Unfortunately, the A-dependence run was taken with the copper absorber, and no platinum target scans were taken with copper absorber during this period. We must therefore extrapolate using the copper-beryllium absorber ratio determined above from the beryllium target scans. This would give a 100%-targeting  $90^\circ$  monitor/SEM ratio of  $0.158 \pm 0.008$ . The background-subtracted  $90^\circ$  monitor/SEM ratio for the platinum A-dependence data was 0.112, thus the average targeting fraction would be  $0.709 \pm 0.038$ . The bead was teardrop-shaped. It can be roughly approximated by an ellipsoid with diameters 0.25 cm x 0.25 cm x 0.34 cm and long axis oriented along the beam direction. Figure 23 shows that all of the tail of the platinum target scans can be accounted for by the bead.



PLATINUM TARGET SCAN AND ESTIMATED BEAD CONTRIBUTION

FIGURE 23



Assuming conservatively that as much as half may have been due to a tail on the beam profile, we obtain as the best estimate for the platinum targeting fraction  $0.927 \pm 0.073$ .

Using this value we compute  $\alpha$  versus mass and transverse momentum as given in Table XII and Figure 24. The data are consistent with a constant value of  $\alpha$  in our mass and transverse momentum range. Averaging over mass, we obtain

$$\langle \alpha \rangle = 1.007 \pm 0.018 \pm 0.028 \quad 5 < m < 11 \text{ GeV}$$

where the first error is statistical and the second is systematic (due chiefly to the uncertainty in the  $P_t$  targeting fraction).

This analysis depends on the  $90^\circ$  monitor and SEM being stable during the A-dependence running. Figure 25 shows the  $90^\circ$  monitor/SEM ratio for each run in the data sample. The beryllium runs, for which the targeting fraction was independent of beam tuning, show that stability was within  $\pm 1.3\%$  r.m.s.

### 3. Efficiency

The trigger efficiency is measured using the study triggers. They were designed so that each trigger element would not be required by some trigger, thus the efficiency of each element can be computed. The standard reconstruction required V1 and V2, but a special compression of events satisfying study triggers was made, for which this requirement was relaxed. The

Table XIIa.

## A-dependence vs. Mass

Mass (GeV)	# events Pt		# events Be		$\alpha$
charge	0	2	0	2	
5.0- 5.4	146	8	142	4	.986 $\pm$ .041
5.4- 5.8	120	2	115	0	.994 $\pm$ .043
5.8- 6.2	95	0	95	2	.993 $\pm$ .048
6.2- 6.6	87	0	68	0	1.066 $\pm$ .053
6.6- 7.0	67	0	63	0	1.006 $\pm$ .057
7.0- 7.4	44	0	44	0	.986 $\pm$ .069
7.4- 7.8	35	0	34	0	.995 $\pm$ .078
7.8- 8.2	23	0	24	0	.972 $\pm$ .095
8.2- 8.6	20	0	9	0	1.246 $\pm$ .131
8.6- 9.0	11	0	7	0	1.133 $\pm$ .157
9.0- 9.4	24	0	18	0	1.079 $\pm$ .101
9.4- 9.8	20	0	19	0	1.003 $\pm$ .104
9.8-10.2	9	0	8	0	1.024 $\pm$ .158
10.2-10.6	2	0	9	0	.497 $\pm$ .254
10.6-11.0	3	0	4	0	.892 $\pm$ .248

## NOTE

Errors are statistical only. There is an additional .028 systematic error at all masses.

Table XIIb.

A-dependence vs.  $p_t$ 

$p_t$ (GeV)	# events Pt		# events Be		$\alpha$
charge	0	2	0	2	
0.0-0.2	35	0	49	1	$1.089 \pm .073$
0.2-0.4	120	2	107	1	$.951 \pm .044$
0.4-0.6	127	2	124	1	$.981 \pm .042$
0.6-0.8	105	1	102	0	$.980 \pm .046$
0.8-1.0	90	0	93	1	$.993 \pm .049$
1.0-1.2	69	1	84	4	$1.039 \pm .055$
1.2-1.4	44	0	50	0	$1.027 \pm .067$
1.4-1.6	28	0	37	1	$1.068 \pm .083$
1.6-1.8	17	0	26	2	$1.098 \pm .107$
1.8-2.0	10	0	12	0	$1.045 \pm .139$
2.0-2.2	8	0	9	0	$1.024 \pm .158$
2.2-2.4	4	0	6	0	$1.118 \pm .210$
2.4-2.6	5	0	2	0	$.688 \pm .272$

## NOTE

Errors are statistical only. There is an additional .028 systematic error at all transverse momenta.

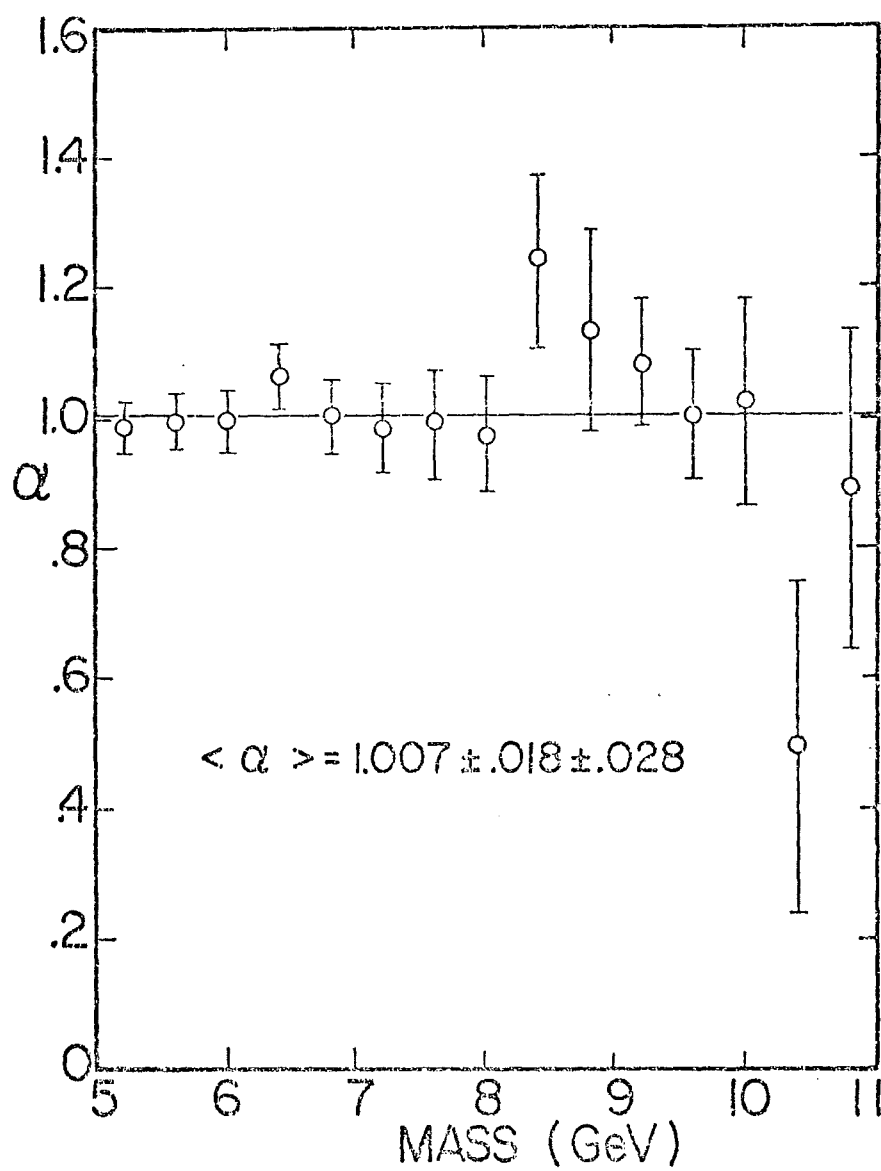
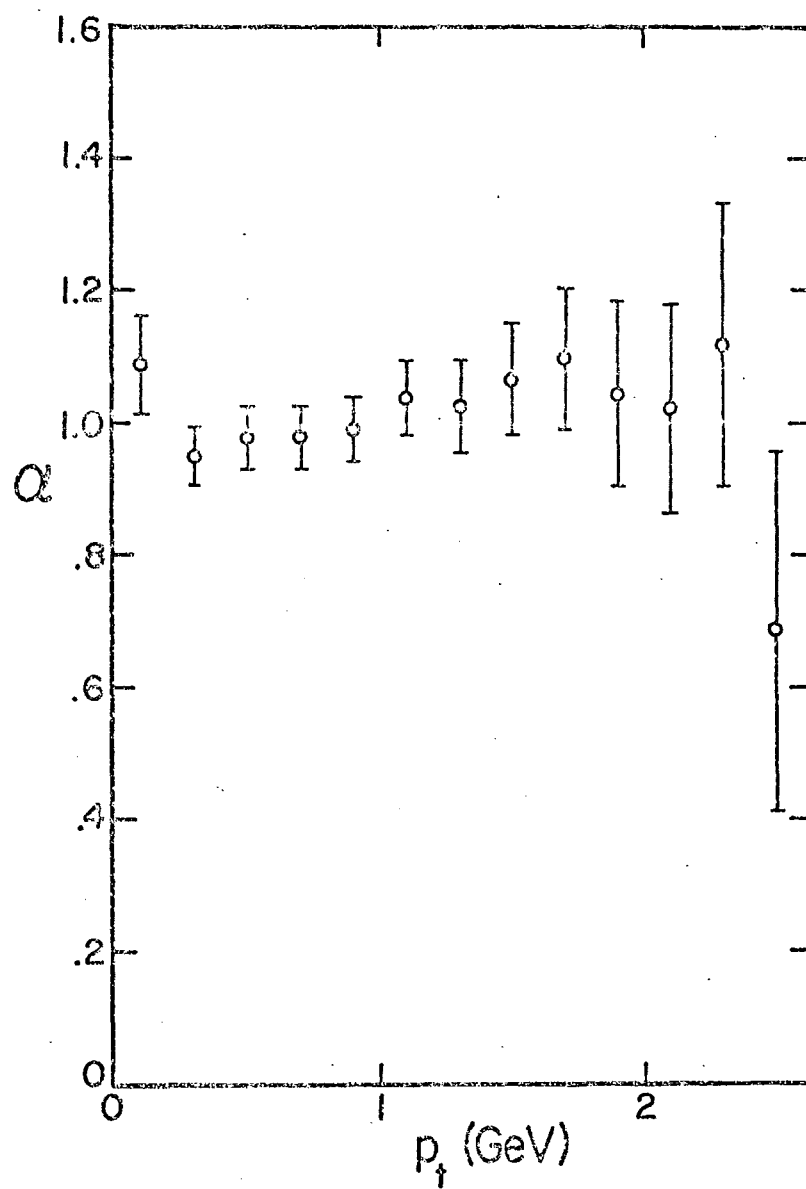
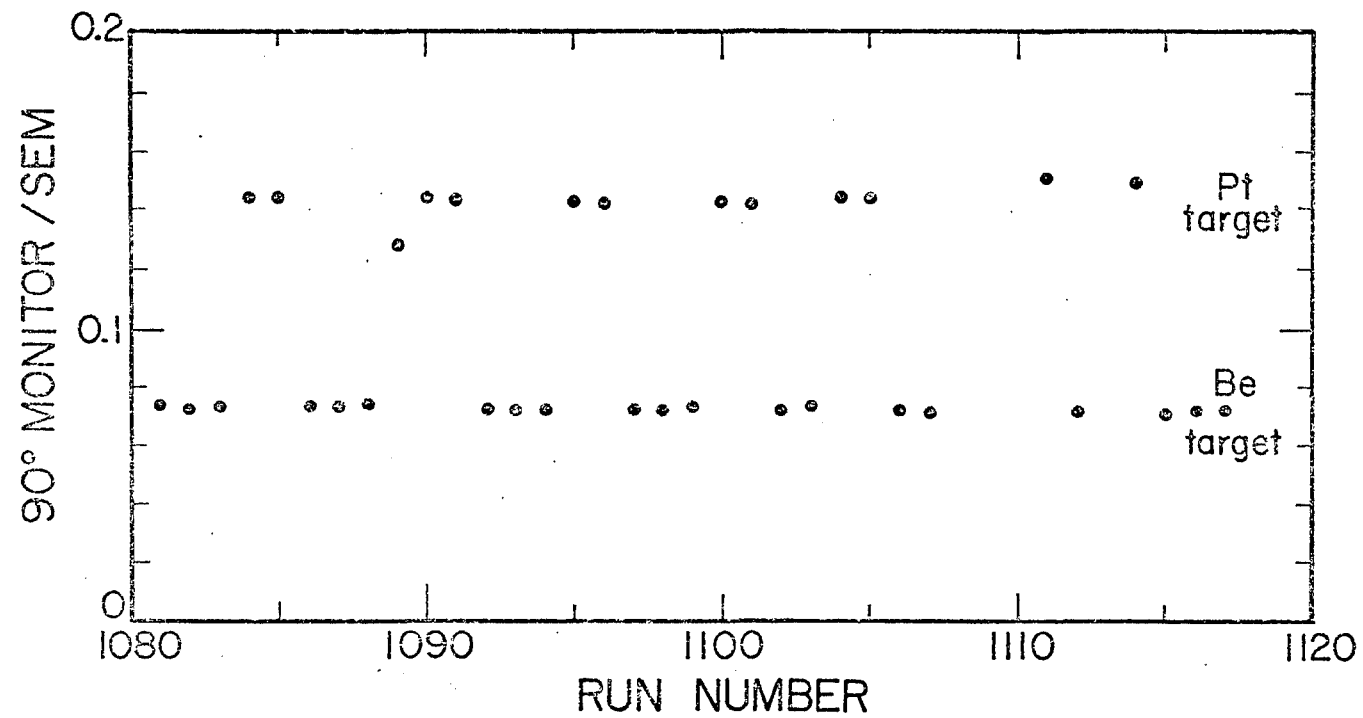
THE POWER  $\alpha$  OF THE A-DEPENDENCE VS. MASS

FIGURE 24a



THE POWER  $\alpha$  OF THE A-DEPENDENCE VS.  $p_t$

FIGURE 24b



90° MONITOR/SEM RATIO DURING THE A-DEPENDENCE RUNNING

FIGURE 25

state of each trigger element except V4 was indicated by a bit which was set on or off by the trigger logic. These bits were available on the study trigger DST, as well as a bit for V4 which was concocted by software using information from the hodoscope readout system. If  $N_o$  is the number of good events for which all the bits are on and  $N_i$  the number for which all but bit  $i$  are on, then the efficiency of element  $i$  is

$$E_i = \frac{N_o}{N_o + N_i} \quad .$$

These efficiencies are tabulated in Table XIII for the two data samples, along with the trigger efficiencies computed from them.

The compression efficiency was determined by writing DST's directly from a few raw data tapes and observing how many good events had been lost in compression. The results are given in table XIV.

Reconstruction and muon cut efficiencies were determined using events in which one chamber did not participate in the reconstructed track or one cut was failed. Since V1 and V2 were required by the standard reconstruction, their reconstruction efficiencies were determined using events from the study trigger DST. Other efficiencies were measured using the full A-dependence event sample. The efficiencies are tabulated in Tables XV and XVI.

Additional efficiencies which must be taken into account are the efficiencies of the target cut, track confidence level cut,

Table XIII

Trigger Efficiencies  
(A-dependence Data)

Trigger element	Trigger	Pt target		Be target	
		Efficiency			
		up	down	up	down
H0	THUD	$.970 \pm .015$	$.985 \pm .010$	$.983 \pm .012$	$.975 \pm .014$
H1	TVUD	$1.000 \pm .045$	$1.000 \pm .048$	$1.000 \pm .030$	$1.000 \pm .030$
H2	TVUD	$1.000 \pm .045$	$1.000 \pm .048$	$1.000 \pm .030$	$1.000 \pm .030$
H3	TVUD	$1.000 \pm .045$	$.955 \pm .045$	$1.000 \pm .030$	$1.000 \pm .030$
C	SINK	$1.000 \pm .007$	$1.000 \pm .007$	$1.000 \pm .007$	$1.000 \pm .007$
V2	THUD	$.985 \pm .011$	$.993 \pm .007$	$1.000 \pm .009$	$.983 \pm .012$
V4	THUD	$1.000 \pm .008$	$1.000 \pm .008$	$1.000 \pm .009$	$1.000 \pm .009$
M	THUD	$.992 \pm .008$	$1.000 \pm .008$	$.992 \pm .008$	$1.000 \pm .009$
T		$1.000 \pm .000$	$1.000 \pm .003$	$1.000 \pm .000$	$1.000 \pm .000$
SINK		$.884 \pm .051$		$.933 \pm .038$	



Table XIV

Compression Efficiencies  
(A-dependence Data)

Pt target	$.956 \pm .014$
Be target	$.963 \pm .013$

Table XV

Reconstruction Efficiencies  
(A-dependence Data)

Plane	Pt target		Be target	
	up	down	up	down
JY	.972 $\pm$ .008	.983 $\pm$ .006	.966 $\pm$ .009	.977 $\pm$ .007
JU	.987 $\pm$ .005	.960 $\pm$ .009	.990 $\pm$ .005	.970 $\pm$ .009
JV	.978 $\pm$ .007	.971 $\pm$ .008	.988 $\pm$ .005	.965 $\pm$ .009
1Y	.968 $\pm$ .008	.958 $\pm$ .010	.935 $\pm$ .012	.944 $\pm$ .011
2Y	.958 $\pm$ .009	.925 $\pm$ .013	.937 $\pm$ .012	.933 $\pm$ .012
3Y	.891 $\pm$ .014	.912 $\pm$ .013	.881 $\pm$ .015	.928 $\pm$ .013
3P	.906 $\pm$ .013	.925 $\pm$ .013	.941 $\pm$ .011	.951 $\pm$ .011
3X	.976 $\pm$ .007	.962 $\pm$ .009	.959 $\pm$ .010	.968 $\pm$ .009
V1	1.000 $\pm$ .010	1.000 $\pm$ .011	1.000 $\pm$ .009	1.000 $\pm$ .010
V2	.990 $\pm$ .010	1.000 $\pm$ .011	1.000 $\pm$ .009	1.000 $\pm$ .010
Track	.965 $\pm$ .014	.971 $\pm$ .016	.972 $\pm$ .013	.979 $\pm$ .014
Pair	.937 $\pm$ .021		.951 $\pm$ .019	

Table XVI

Muon Cut Efficiencies  
(A-dependence Data)

Plane	Pt target		Be target	
	up	down	up	down
4Y	$.964 \pm .009$	$.906 \pm .014$	$.935 \pm .012$	$.911 \pm .014$
5Y	$.949 \pm .010$	$.938 \pm .012$	$.952 \pm .010$	$.933 \pm .012$
H2	$1.000 \pm .002$	$1.000 \pm .002$	$1.000 \pm .002$	$1.000 \pm .003$
H3	$1.000 \pm .002$	$1.000 \pm .002$	$1.000 \pm .002$	$1.000 \pm .003$
V3	$.998 \pm .002$	$.985 \pm .006$	$.983 \pm .006$	$.982 \pm .007$
V4	$.996 \pm .003$	$1.000 \pm .002$	$1.000 \pm .002$	$1.000 \pm .003$
Combined	$.998 \pm .001$	$.992 \pm .002$	$.995 \pm .001$	$.991 \pm .002$
Pair	$.990 \pm .002$		$.987 \pm .002$	

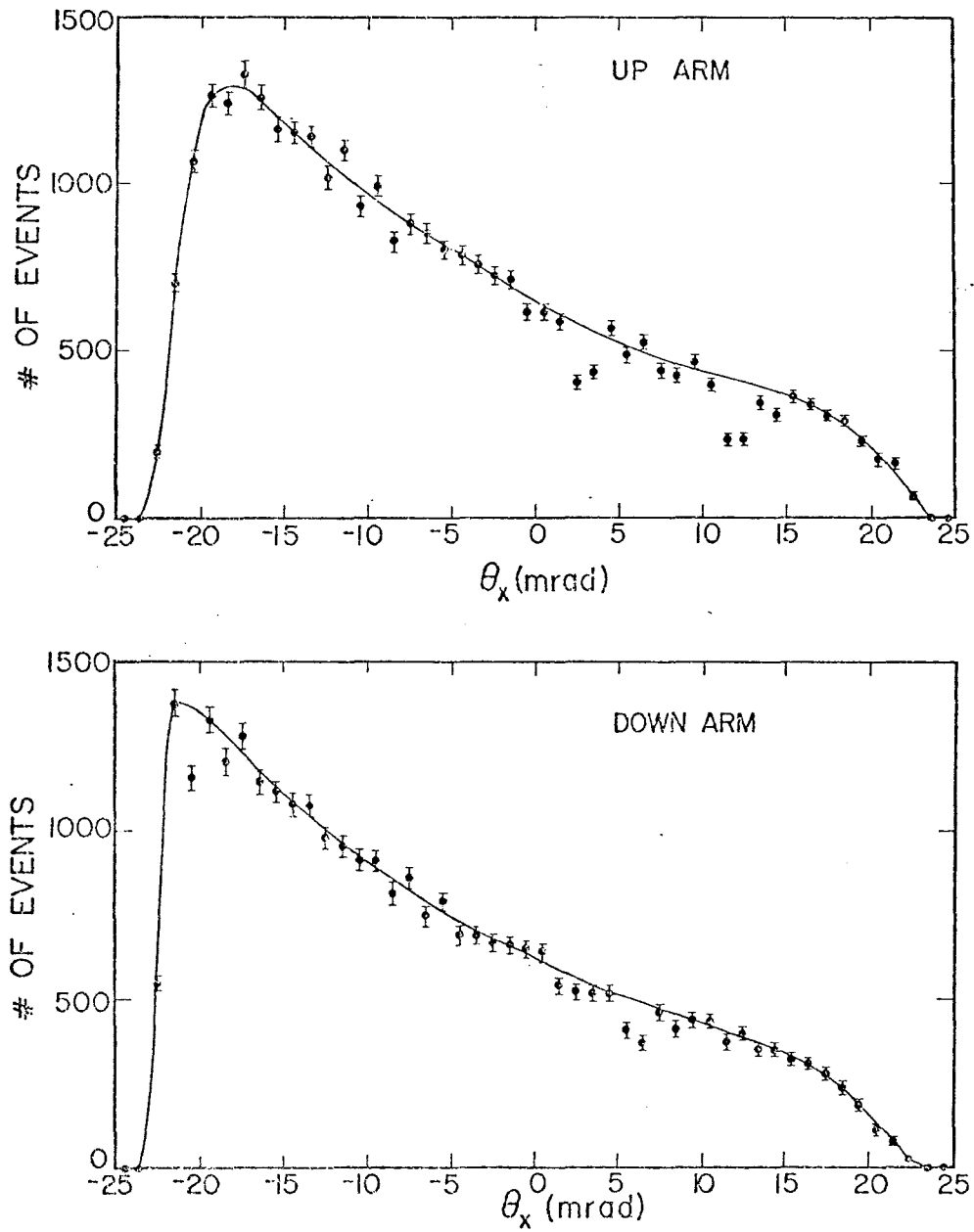
and one-track-per-arm requirement; they are given in Table XVII, which also summarizes all the other efficiencies and gives the overall efficiency for each data sample. The efficiencies of the two data samples are consistent, verifying the cancellation in Equation (3). I use the average of the two efficiencies in computing cross-sections.

For the most part efficiencies were uniform across the apertures. Recalcitrant hodoscope or MWPC channels were watched for carefully during the run and were repaired mercilessly whenever they showed themselves. At large angles however, where rates were low, an inefficient element might lurk for days, hidden among innocent fluctuations. Such are the inefficiencies revealed in Figure 26, which shows the distribution of events versus horizontal angle in the two arms. These inefficiencies are corrected for in the acceptance calculation using the efficiency factors listed in Table XVIII. The factors are the ratios of the inefficient points of Figure 26 to the curves drawn through the surrounding points. Only points differing from the curves by at least 10% and two standard deviations were corrected. Possible inefficiencies at small angles were ignored, as events at the edges of the apertures are to be removed by a cut discussed in section 4 below. These corrections have no significant effect on the A-dependence analysis. (It might be thought that this correction procedure represents double counting of the inefficiency, since the hodoscope

Table XVII

Efficiency Summary  
(A-dependence Data)

	Pt target	Be target
Trigger	$.884 \pm .051$	$.933 \pm .038$
Compression	$.956 \pm .014$	$.963 \pm .013$
Reconstruction	$.937 \pm .021$	$.951 \pm .019$
Muon cuts	$.990 \pm .002$	$.987 \pm .002$
Target cut	$.988 \pm .005$	$.972 \pm .008$
Track C.L.	$1.000 \pm .002$	$1.000 \pm .003$
One track	$.990 \pm .004$	$.993 \pm .003$
Combined	$.767 \pm .057$	$.814 \pm .045$
Average	$.796 \pm .035$	



HORIZONTAL ANGLE DISTRIBUTIONS IN THE TWO ARMS

FIGURE 26

efficiencies averaged over the aperture were already determined above using the study trigger data. However, the inefficiencies of Table XVIII do not show up in the study trigger data, as they were caused by malfunctions of the hodoscope fanin logic going into the trigger, rather than by malfunctions of the hodoscopes themselves.)

#### 4. Acceptance

The acceptance as a function of any one kinematic variable is an integral of the production cross-section over all the other variables, with complicated limits of integration which are determined by the placement of detectors. To compute the acceptance one must thus know the production cross-section, and vice versa, so an iterative procedure is used which has converged once self-consistent results are obtained. The integration is done by Monte Carlo simulation of the spectrometer. All relevant effects are simulated, including multiple scattering and energy loss in the copper, beryllium, CH<sub>2</sub>, and steel, measuring error of the chambers, and hodoscope inefficiencies (discussed above). The acceptances thus obtained are shown in Figures 27-30 versus the mass, transverse momentum  $p_t$ , CMS rapidity  $y$ , and decay angle of the muon pair. The rapidity is defined as

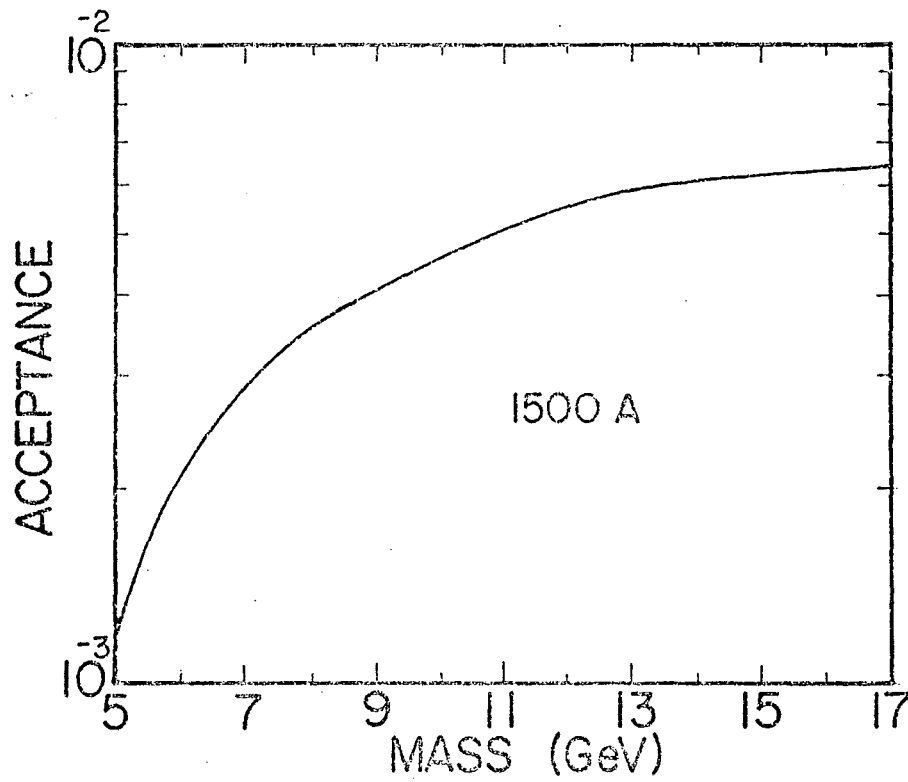
$$y = 0.5 \ln ((E + p_{||}) / (E - p_{||}))$$

where  $E$  and  $p_{||}$  are the energy and longitudinal momentum of the muon

TABLE XVIII  
Hodoscope Efficiency Corrections

$\theta_x$ bin	Efficiency
Up arm	
.002-.003	.70
.003-.004	.79
.011-.012	.56
.012-.013	.59
.013-.014	.90
.014-.015	.83
Down arm	
.005-.006	.81
.006-.007	.75





ACCEPTANCE VS. MASS

FIGURE 27

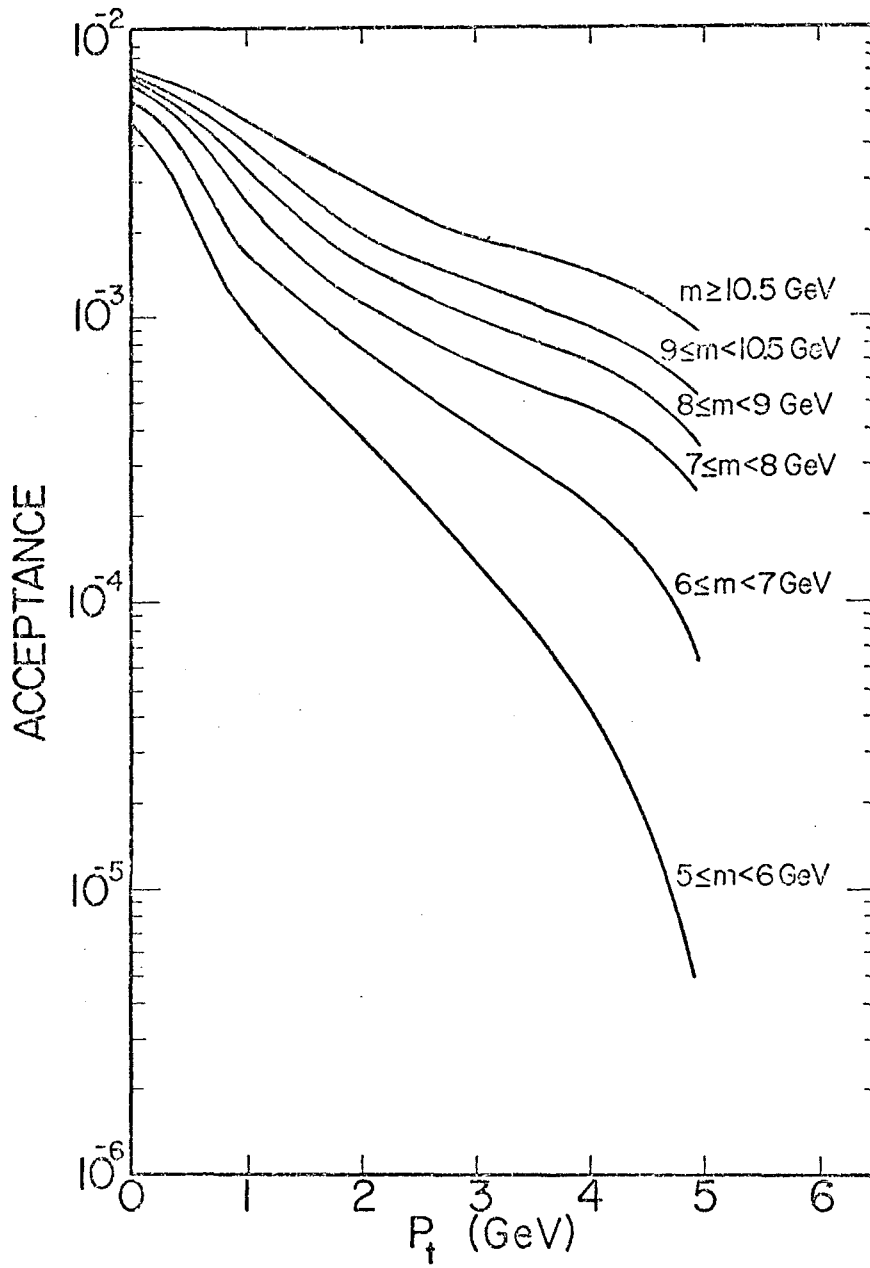
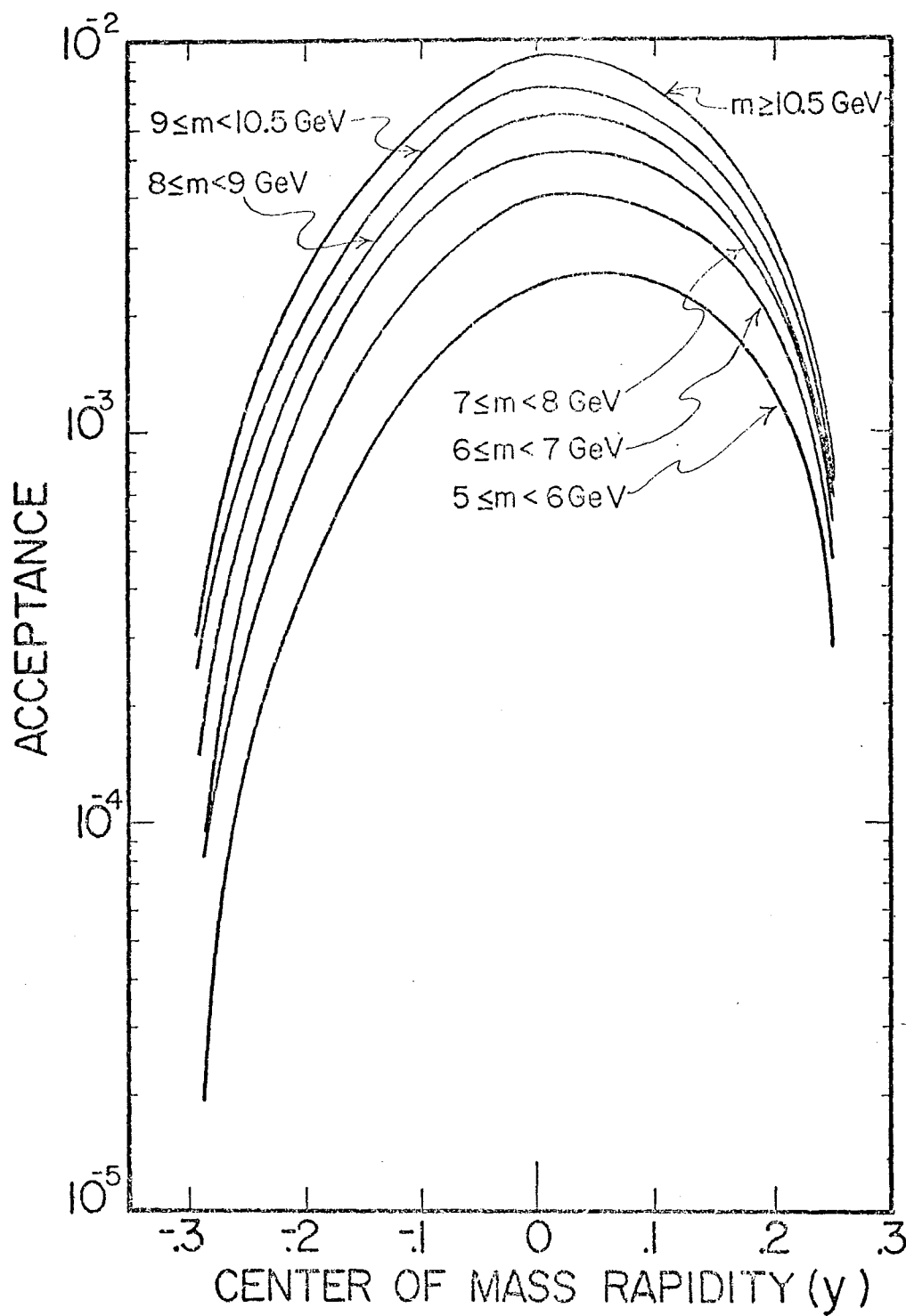
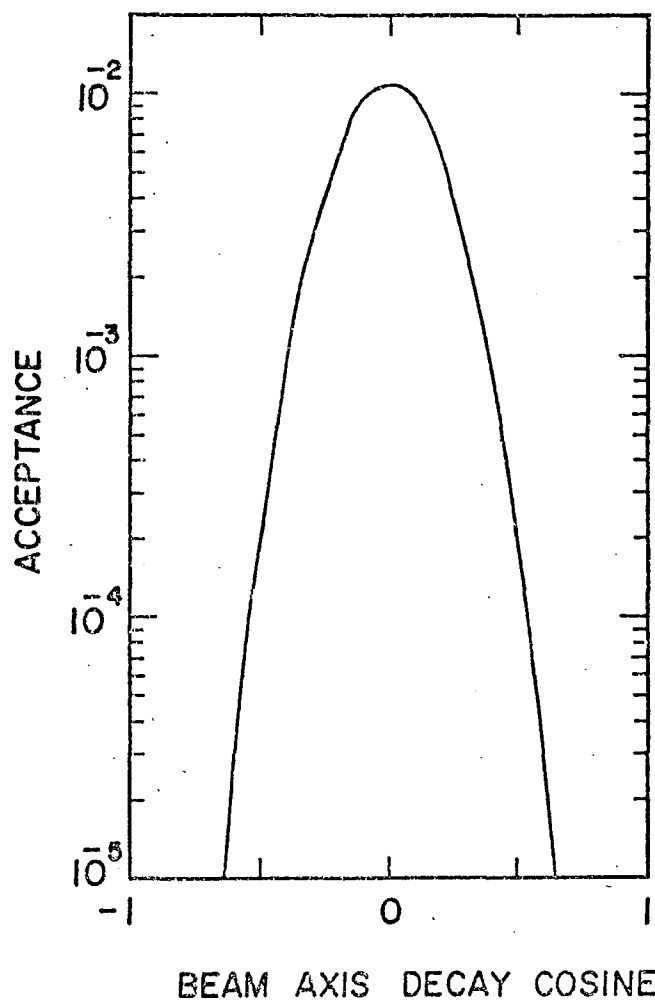
ACCEPTANCE VS.  $p_t$ 

FIGURE 28



ACCEPTANCE VS. RAPIDITY

FIGURE 29



ACCEPTANCE VS. BEAM AXIS DECAY COSINE

FIGURE 30

pair in the CMS. The decay angle is discussed below.

The shape of the mass acceptance can be qualitatively understood as follows: At low mass the muons have low momenta and are deflected through large angles, thus only muons near the top and bottom of the aperture are accepted; muons entering the magnet in the middle of the aperture are deflected out and miss the detectors. As the mass increases and the deflection angle decreases, the fraction of the aperture over which muons are accepted increases.

The  $p_t$  acceptance falls rapidly at low mass because high  $p_t$  events are asymmetrical, one muon having lower momentum than the other, and the low momentum muon is accepted only over a small fraction of the aperture. At high mass momenta increase, so this effect is less pronounced and the  $p_t$  acceptance falls less rapidly.

The shape of the rapidity acceptance is approximately independent of mass, since for symmetric events the rapidity is approximately independent of momentum and a function of horizontal angle only:

$$y = -\eta (\tan \theta/2)$$

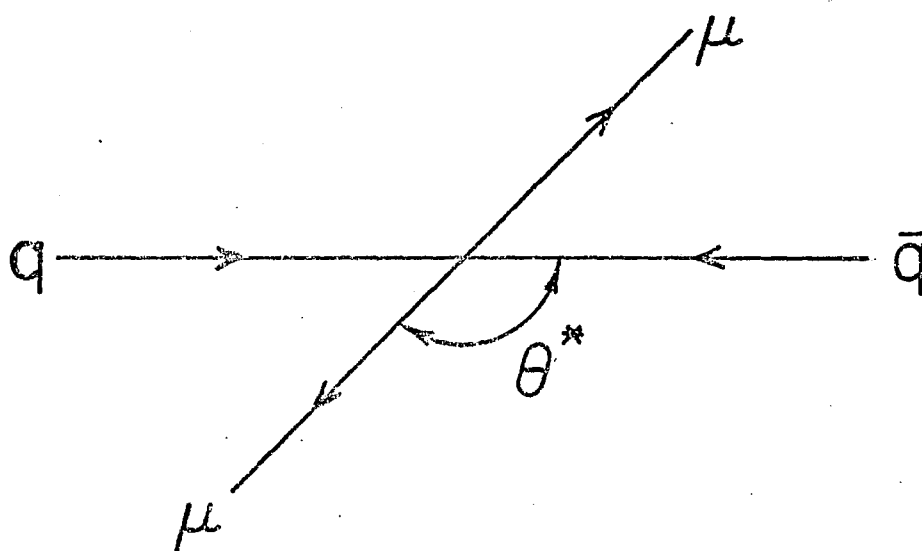
where  $\theta$  is the angle of each muon relative to the beam in the CMS. A slight mass dependence comes about as follows: At low mass the acceptance is peaked slightly forward of  $y = 0$ , since events at positive  $y$  have higher momentum in the lab than events at negative

y and are accepted over more of the aperture. As the mass increases this effect becomes less important and the rapidity acceptance becomes more symmetrical.

It is desirable that acceptances be slowly varying so that shapes of measured distributions will not be strongly affected by small mistakes in the positions or efficiencies of detectors. We see that at high mass the mass and  $p_t$  acceptances satisfy this condition. However, the rapidity acceptance is quite narrow and rapidly changing, and so is the acceptance in decay angle. In order to avoid egregious model-dependence of our results, we therefore present cross-sections differential in rapidity and make no attempt to extrapolate beyond the observed rapidity interval of  $-0.28 \leq y < 0.26$ . Within this interval the Monte Carlo assumes that the cross-section is independent of rapidity. Cross-sections differential in decay angle would be less useful, so we integrate over decay angle, accepting reluctantly the resulting model-dependence. The expected decay angle distribution for Drell-Yan production is<sup>3</sup>

$$\frac{dN}{d \cos \theta^*} \propto 1 + \cos^2 \theta^*$$

measured in the dimuon CMS. The angle  $\theta^*$  is measured from the direction of motion of the quark to one of the outgoing muons (see Figure 31). Transverse momentum complicates matters. Since the annihilating quarks may not have been moving in the same directions as the



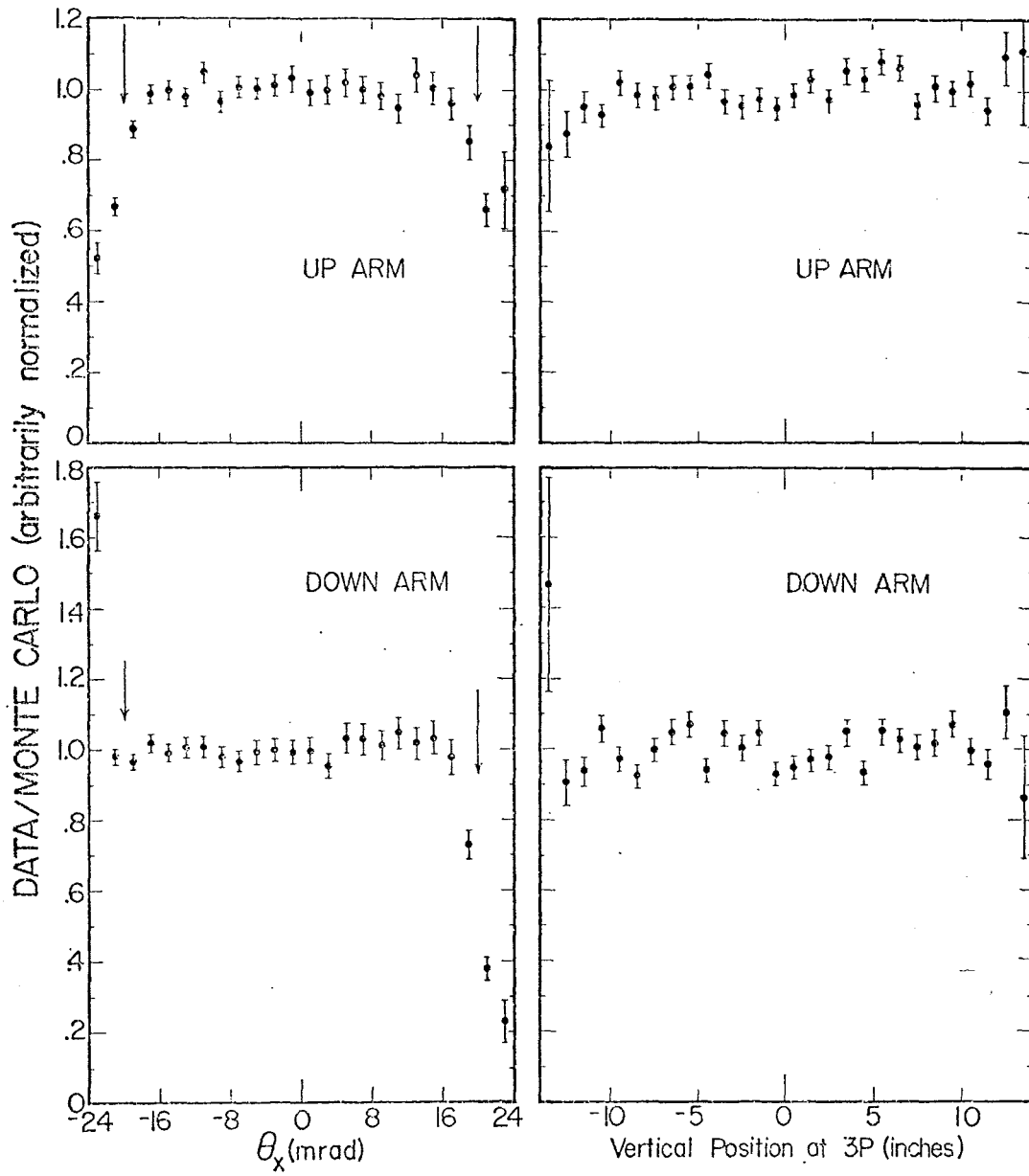
DEFINITION OF THE DECAY  
ANGLE  $\theta^*$

FIGURE 31

colliding nucleons, one doesn't know in what directions the annihilating quarks were moving, or with respect to what axis to evaluate the decay angle. It is a good approximation, however, to use the beam direction<sup>36</sup> (this is known as the Gottfried-Jackson or t-channel helicity frame). The acceptance in beam axis decay angle is shown in Figure 30. It is seen to be insufficiently broad to permit a measurement of the decay angle distribution; in particular,  $1 + \cos^2\theta$  and isotropic decay are practically indistinguishable in shape over our region of acceptance. Fortunately, the decay angle dependence factors out of our acceptance to a good approximation. The only important effect is a change in normalization: the acceptance is 30% bigger assuming isotropic decay. This is a simple geometrical effect: the two spectrometer arms are at  $90^\circ$  in the CMS, and the  $1 + \cos^2\theta$  decay distribution suppresses decays at  $90^\circ$ . (An additional slight coupling of the  $p_t$  and decay angle acceptances is discussed in section E.3.)

To verify that the Monte Carlo program accurately simulates the apparatus, we compare Monte Carlo-generated event distributions to those of the data. This comparison has little meaning for the physics variables (mass,  $p_t$ , and rapidity) since the Monte Carlo has been adjusted to match the data in these variables. Figure 32 therefore shows ratios of Monte Carlo distributions in horizontal angle and vertical position at 3P in each spectrometer arm. The





RATIOS OF DATA EVENT DISTRIBUTIONS  
TO MONTE CARLO EVENT DISTRIBUTIONS

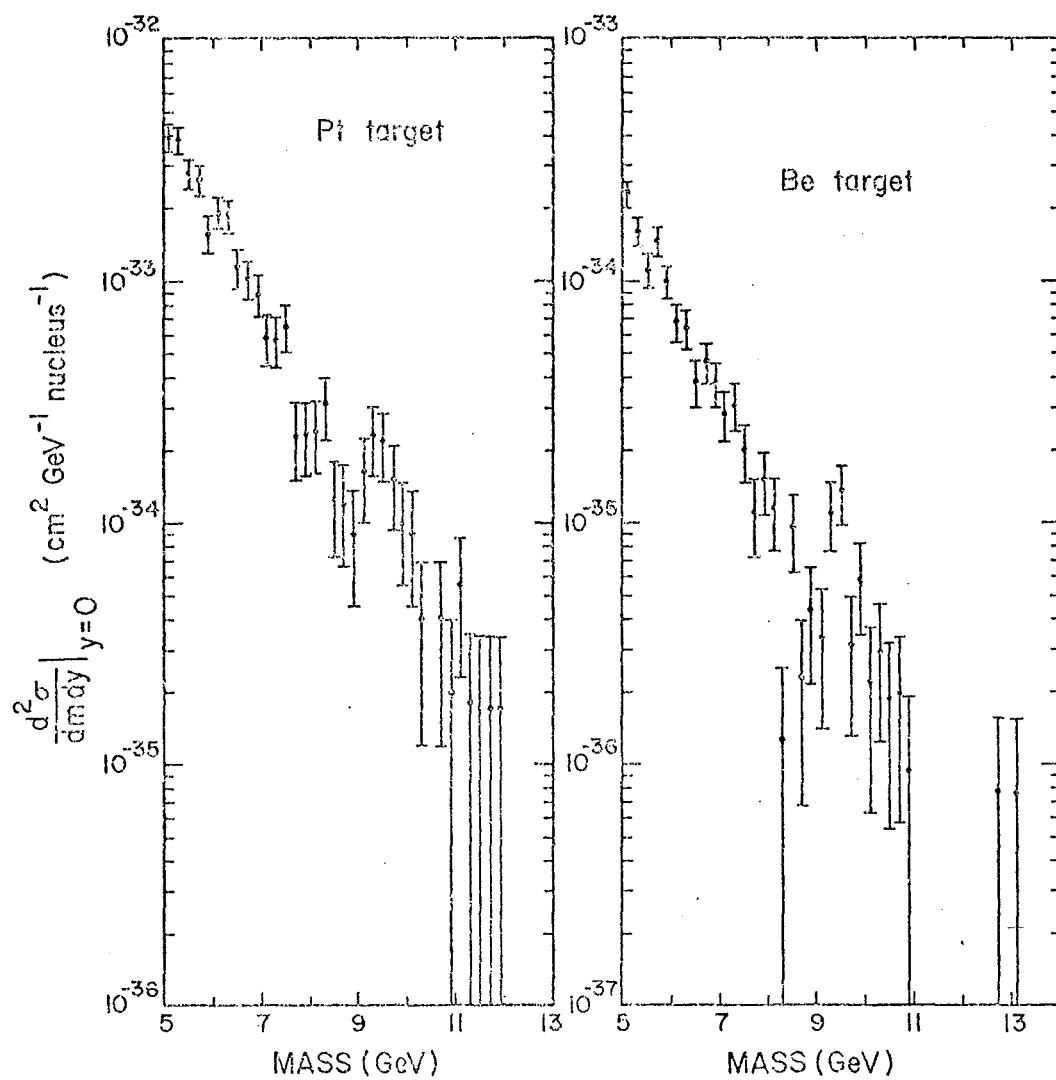
FIGURE 32

Monte Carlo and the data disagree at the horizontal edges of the apertures. Since the edges of the apertures contain few events, it is reasonable to tighten the fiducial cuts to exclude the regions of disagreement. This has been done in the acceptance curves of Figures 27-30. These cuts restrict events to horizontal angles within  $\pm 20$  mrad. They reduce the acceptance by 40% but remove only 20% of the events.

It is natural to ask how accurately the acceptance is known. The statistical error is straightforward. Sufficient Monte Carlo events were generated so that the statistical error of the acceptance increases the statistical error of the cross-section by nowhere more than 27%. Systematic errors are more difficult to assess. One check of the systematic accuracy of the Monte Carlo is provided by the comparisons discussed in the preceding paragraph. We also compared the mass resolution of the Monte Carlo with the resolution calculated from the data. The resolutions agreed within 20% with the Monte Carlo having the worse resolution. Another check is provided by a second, independent Monte Carlo program, which computed a mass acceptance which agreed within 10% with that computed by the main Monte Carlo.

### C. Mass Spectra and Resonant Structure

Figure 33 presents the differential cross-sections per nucleus versus mass for the two A-dependence data sets. The data have been corrected using the acceptance of Figure 27, i.e. assuming  $1 + \cos^2 \theta$  decay distribution and flat rapidity distribution. This



DIFFERENTIAL CROSS-SECTION PER NUCLEUS VS. MASS

FIGURE 33

latter assumption means that what is graphed is actually the cross-section evaluated at the mean accepted rapidity, which changes slightly as a function of mass. However, it is never greater than 0.02 and, as shown below, the rapidity dependence of the cross-section is sufficiently gentle that negligible error is made in calling Figure 33 the cross-section at zero rapidity.

The cross-section per nucleon computed from the entire 1500A data sample is shown in Figure 34. The data have been normalized by matching areas with the Be target data of Figure 33 divided by 9.012, i.e. by assuming linear A-dependence.

The most striking feature of Figures 33 and 34 is the enhancement of the cross-section in the vicinity of 9.5 GeV mass. To study the 9.5 GeV region in more detail, we fit the data excluding the region from 8.8 to 11 GeV and examine the excess of the data over the fit. A good fit is obtained with the function

$$A \exp \left[ -b (m - m_o) \right]$$

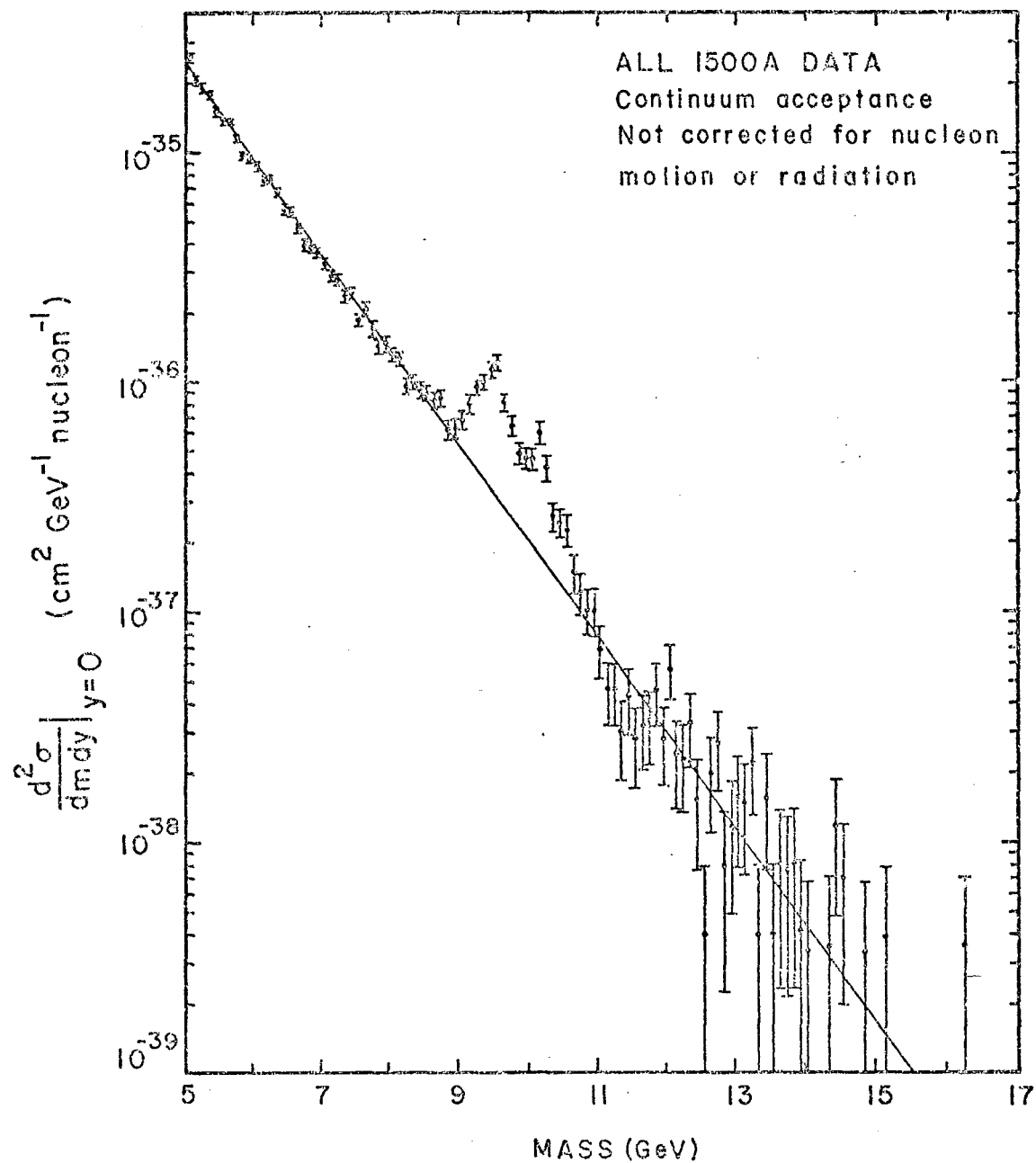
where  $A = (3.519 \pm 0.033) \times 10^{-36} \text{ cm}^2/\text{GeV/nucleon}$

$$b = 0.953 \pm 0.008 \text{ GeV}^{-1}$$

$$m_o = 7 \text{ GeV}$$

$$\chi^2 = 56.0 \text{ for 45 degrees of freedom}$$

$$\text{confidence level} = 0.127$$



DIFFERENTIAL CROSS-SECTION PER NUCLEON VS. MASS

Line is exponential fit (see text)

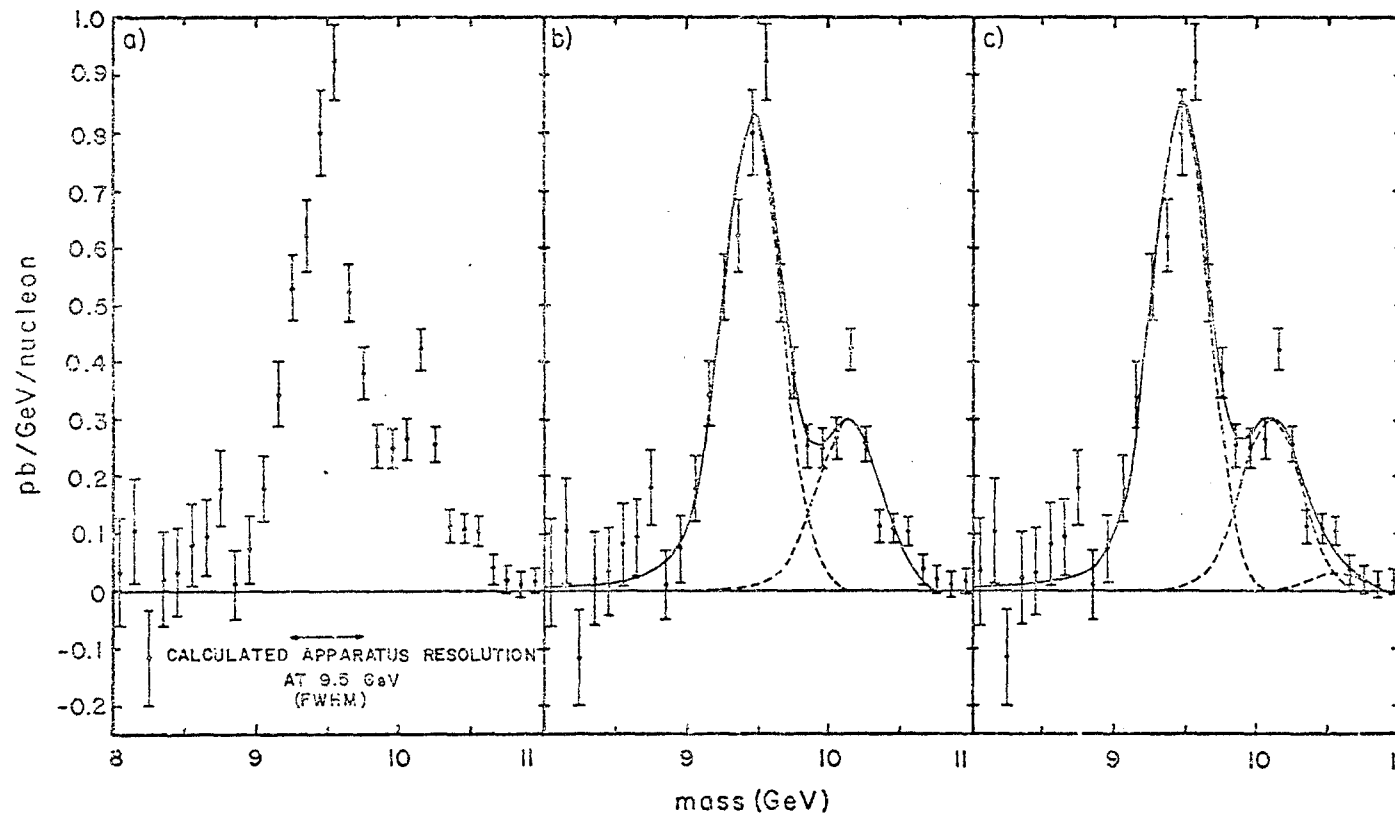
FIGURE 34

(Note that  $m_0$  is not a variable parameter of the fit; rather, it is included in order to reduce the correlation between A and b.) This is the line shown in Figure 34. In the region from 9 to 10.5 GeV there are 1942 events where the fit predicts 780, so the enhancement represents a 40 standard deviation fluctuation of the continuum. Its statistical significance is thus beyond question.

Figure 35a shows the excess of the data over the exponential fit in the enhancement region. The enhancement is seen to be broader than the calculated apparatus resolution, which is 490 MeV FWHM (full-width at half maximum) at 9.5 GeV. The shape of the enhancement is highly suggestive of two closely spaced resonances, and indeed the hypothesis of a single broad resonance is a very poor fit:  $\chi^2 = 139.3$  for 64 degrees of freedom. It is therefore appropriate to try fitting the data under the hypothesis that two or more closely spaced narrow resonances are being observed. The response of the apparatus to a narrow resonance, as calculated by the Monte Carlo program, is shown in Figure 36a. It is Gaussian in shape to good approximation. However, radiative effects create a tail extending to lower mass<sup>37</sup> according to the formula

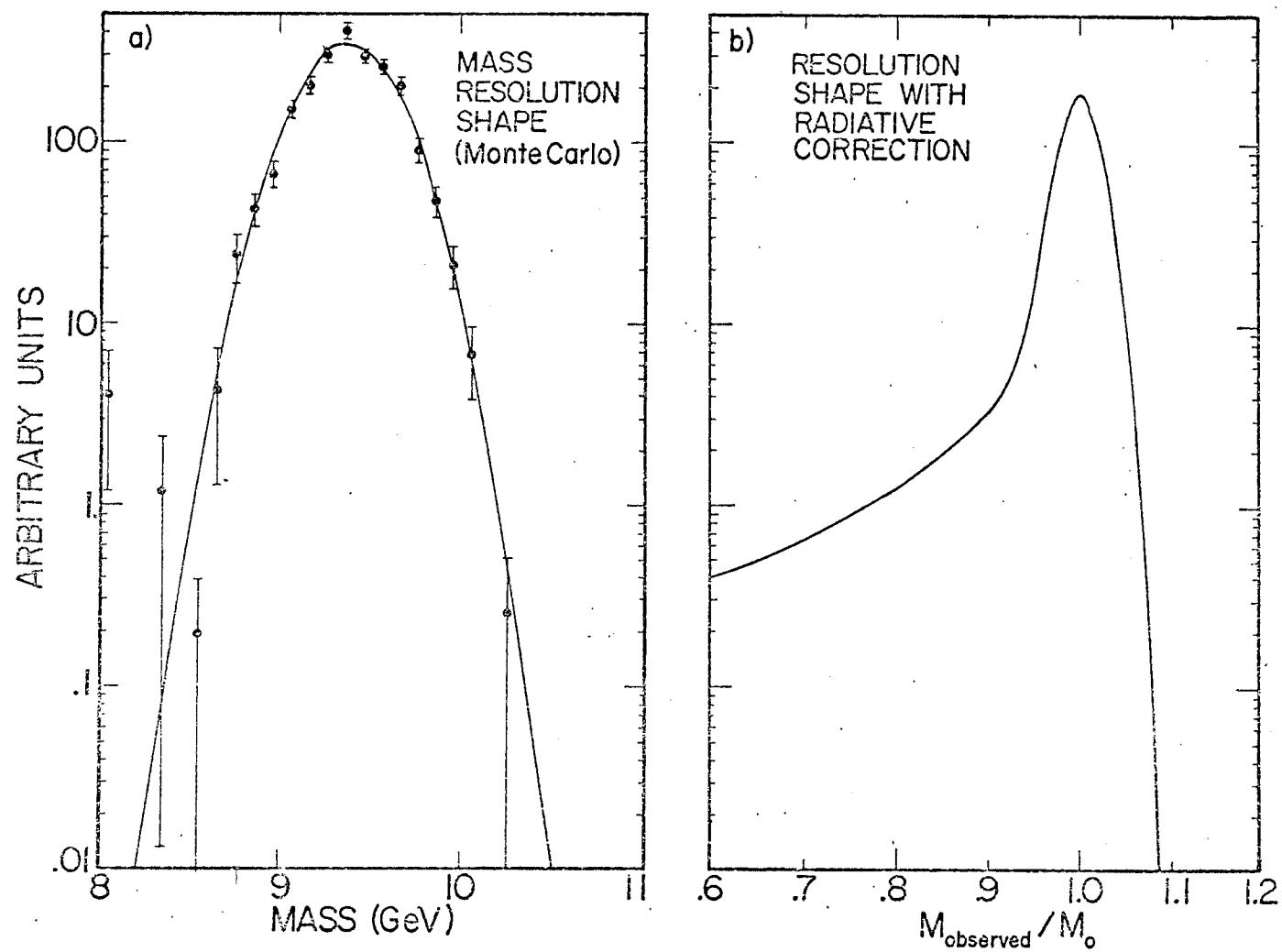
$$\frac{dN}{dM_{\text{obs}}^2} \propto \frac{1 + M_{\text{obs}}^4/M^4}{1 - M_{\text{obs}}^2/M^2} \left( \ln \frac{M_{\text{obs}}^2}{m_\mu^2} - 1 \right)$$

This has been folded with the apparatus resolution to produce the



a) CONTINUUM-SUBTRACTED CROSS-SECTION IN THE ENHANCEMENT REGION  
AND b) TWO- AND c) THREE-RESONANCE FITS

FIGURE 35



MASS RESOLUTION SHAPE a) WITHOUT AND b) WITH RADIATIVE CORRECTION

FIGURE 36



distribution shown in Figure 36b. We fit the data of Figure 34 with the sum of an exponential and two or three resonance distributions whose shapes are given by Figure 36b. The widths of the resonance distributions are permitted to vary, but the ratios of the widths are fixed according to the ratios of the calculated mass resolutions at the fitted mass values. The results of the fits are given in Table XIX and Figures 35b and c. It is evident that at least two resonances are being observed. The hypothesis of a third resonance improves the  $\chi^2$  by an insignificant amount. We have dubbed the resonances T, T', and, should it be confirmed, T''. As discussed in section VI below, there is additional evidence for the existence of the T''. The observed widths of the resonances are consistent with our calculated mass resolution, leading to the conclusion that their intrinsic widths are less than 100 MeV. Concerning the nature of the T's, the most likely hypothesis is that they are bound states of a new heavy quark and its antiquark; this will be amplified below. Note that the cross-sections of Table XIX and Figures 34 and 35 are intermediate results of the analysis; corrections to them are discussed below.

Several studies were made to insure that the enhancement is genuine and not the result of non-uniformities in the apparatus response, errors in the analysis software, or other such bugaboos. These have been discussed by Herb et al.<sup>1</sup> and Lederman<sup>38</sup>. Since the T has now been observed in other experiments<sup>39</sup> as well as ours,

TABLE XIX

Resonance Plus Continuum Fits  
(Not corrected for nucleon motion, radiation, or T acceptance)

	1-resonance	2-resonance	3-resonance
A (cm <sup>2</sup> /GeV)	(3.42±.03)x10 <sup>-36</sup>	(3.52±.03)x10 <sup>-36</sup>	(3.51±.03)x10 <sup>-36</sup>
b (GeV <sup>-1</sup> )	.982±.010	.951±.007	.953±.007
m <sub>1</sub> (GeV)	9.509±.017	9.467±.015	9.465±.015
(B $\frac{d\sigma}{dy}$ ) <sub>1</sub> (cm <sup>2</sup> )	(8.26 <sup>+.50</sup> <sub>-.47</sub> )x10 <sup>-37</sup>	(4.72±.28)x10 <sup>-37</sup>	(4.62±.28)x10 <sup>-37</sup>
Width (GeV)	.662 <sup>+.045</sup> <sub>-.044</sub>	.206±.012	.195±.013
m <sub>2</sub> -m <sub>1</sub> (GeV)		.691±.027	.653 <sup>+.037</sup> <sub>-.040</sub>
(B $\frac{d\sigma}{dy}$ ) <sub>2</sub> (cm <sup>2</sup> )		(1.85±.17)x10 <sup>-37</sup>	(1.76±.18)x10 <sup>-37</sup>
m <sub>3</sub> -m <sub>1</sub> (GeV)			1.097 <sup>+.163</sup> <sub>-.170</sub>
(B $\frac{d\sigma}{dy}$ ) <sub>3</sub> (cm <sup>2</sup> )			(2.17 <sup>+.2.04</sup> <sub>-1.46</sub> )x10 <sup>-38</sup>
$\chi^2$ /DF	139.3/64	72.7/62	70.2/60
C.L.	<10 <sup>-6</sup>	.167	.172

## NOTE

1. Errors are statistical only.
2. For details of mass calibration see Appendix.
3. Width is  $\Gamma$  of Breit-wigner distribution for 1-resonance fit, resolution width for 2- and 3-resonance fits.

these studies are no longer of much relevance, so I will not discuss them here.

#### D. Transverse Momentum and Rapidity Spectra

Figure 37 shows the invariant cross-section per nucleon versus the transverse momentum of the muon pair. The curves represent a convenient parametrization of the cross-section which works well at all masses except for the 9 to 10.5 GeV bin:

$$E \frac{d^3\sigma}{dp^3} \propto \left[ 1 + \left( \frac{p_t}{2.8 \text{ GeV}} \right)^2 \right]^{-6} \quad (1)$$

This curve has also been indicated in the 9 to 10.5 GeV bin, normalized to have the same area as the data. In that bin the data are seen to fall significantly more slowly with increasing  $p_t$  than the curve. Figure 38 shows the mean  $p_t$  and  $p_t^2$  of the data versus mass. Averaging over mass but excluding the T bin,

$$\langle p_t \rangle = 1.20 \pm 0.02 \text{ GeV} .$$

Using this value for the  $\langle p_t \rangle$  of the continuum under the T, we can extract the  $\langle p_t \rangle$  of the T:

$$\langle p_t \rangle_T = 1.42 \pm 0.08 \text{ GeV} .$$

This is evidence that the T is produced by a different production

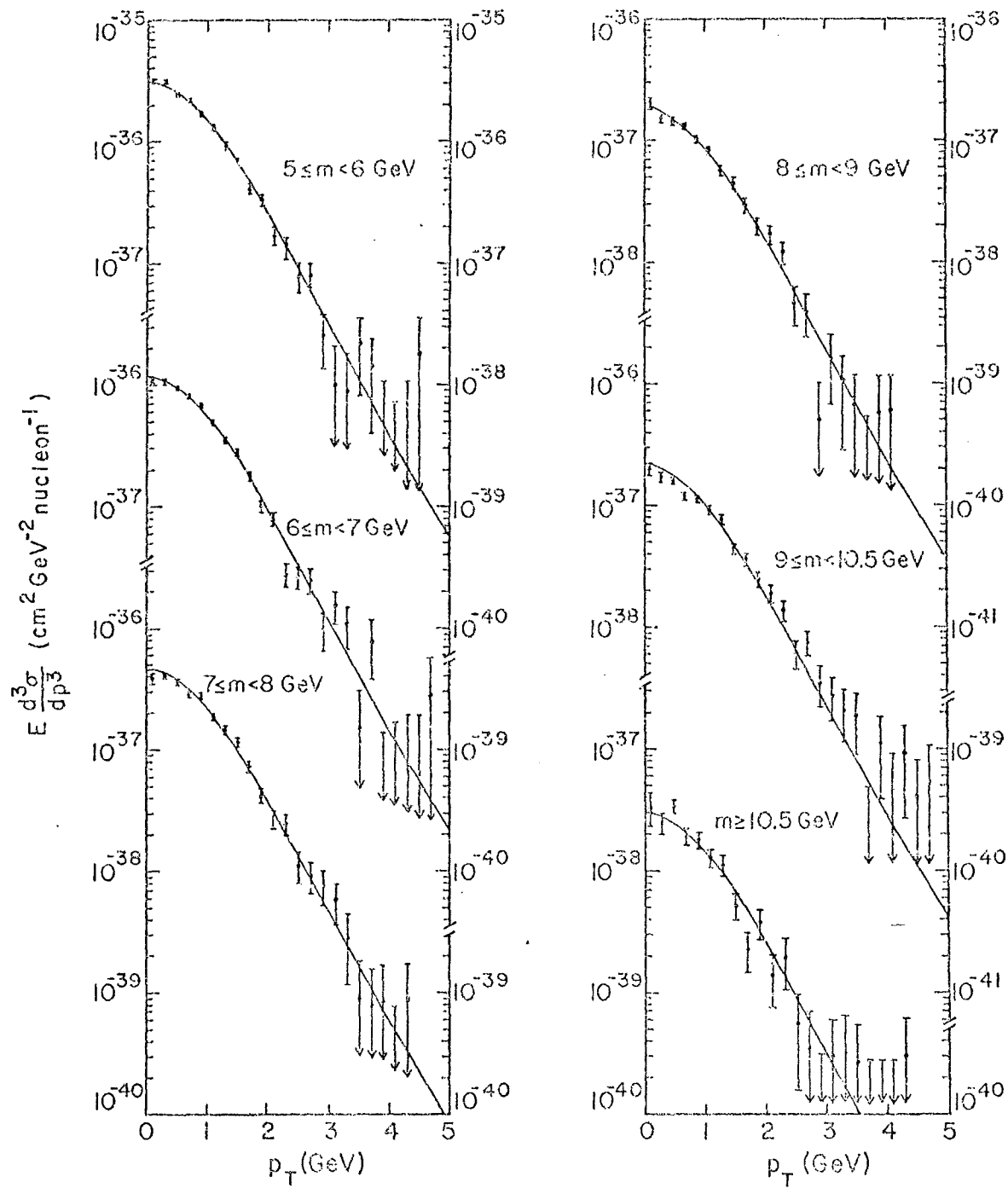
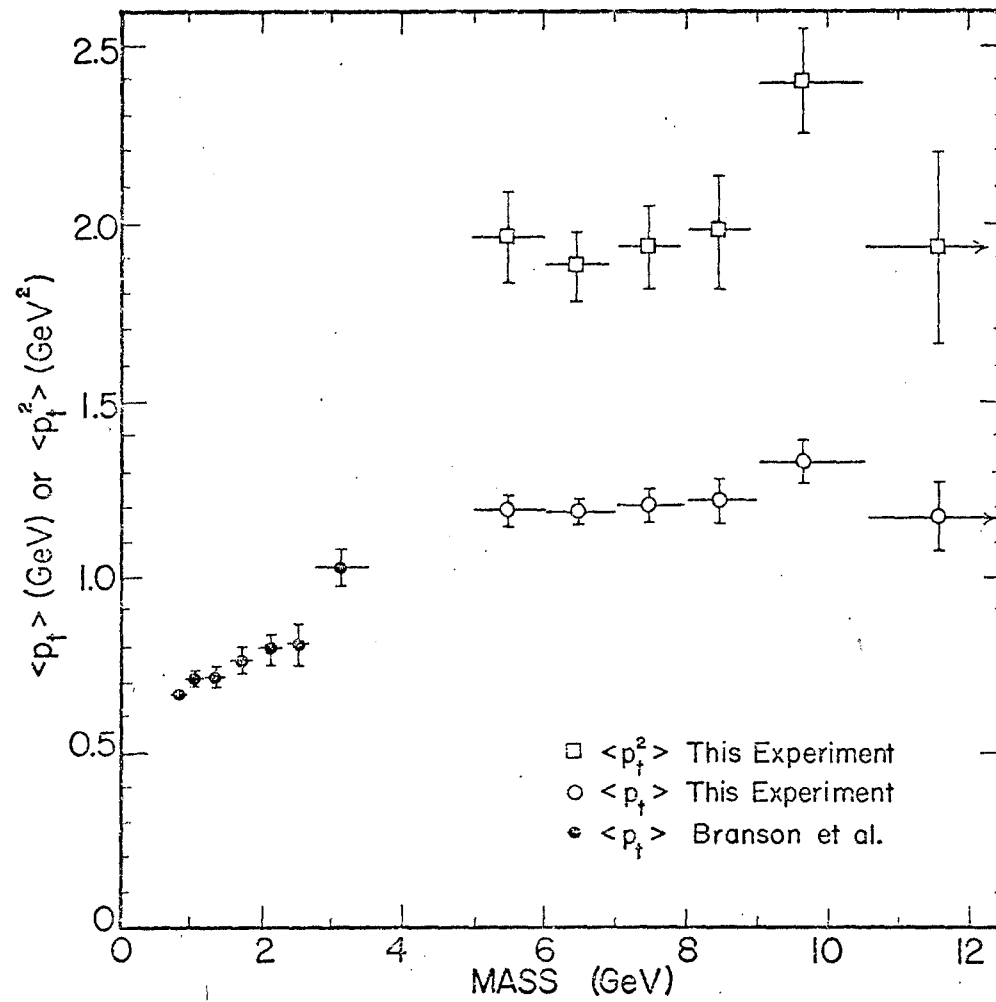
INVARIANT CROSS-SECTION VS.  $p_t$ 

FIGURE 37



$\langle p_t \rangle$  AND  $\langle p_t^2 \rangle$  VS. MASS

FIGURE 38

mechanism than that of the continuum. (A slightly larger value for  $\langle p_t \rangle_T$  will be obtained in section E.3 below due to an acceptance effect therein discussed.)

Figure 39 shows the differential cross-section versus rapidity. Linear fits in each mass bin are also shown, and the slopes of the fits are graphed versus mass in Figure 40. The positive slopes of the continuum rapidity distributions can be understood in the parton model (discussed in section VI below). The T stands out as having a flatter rapidity spectrum. This is further evidence of the differing origins of the T and the continuum.

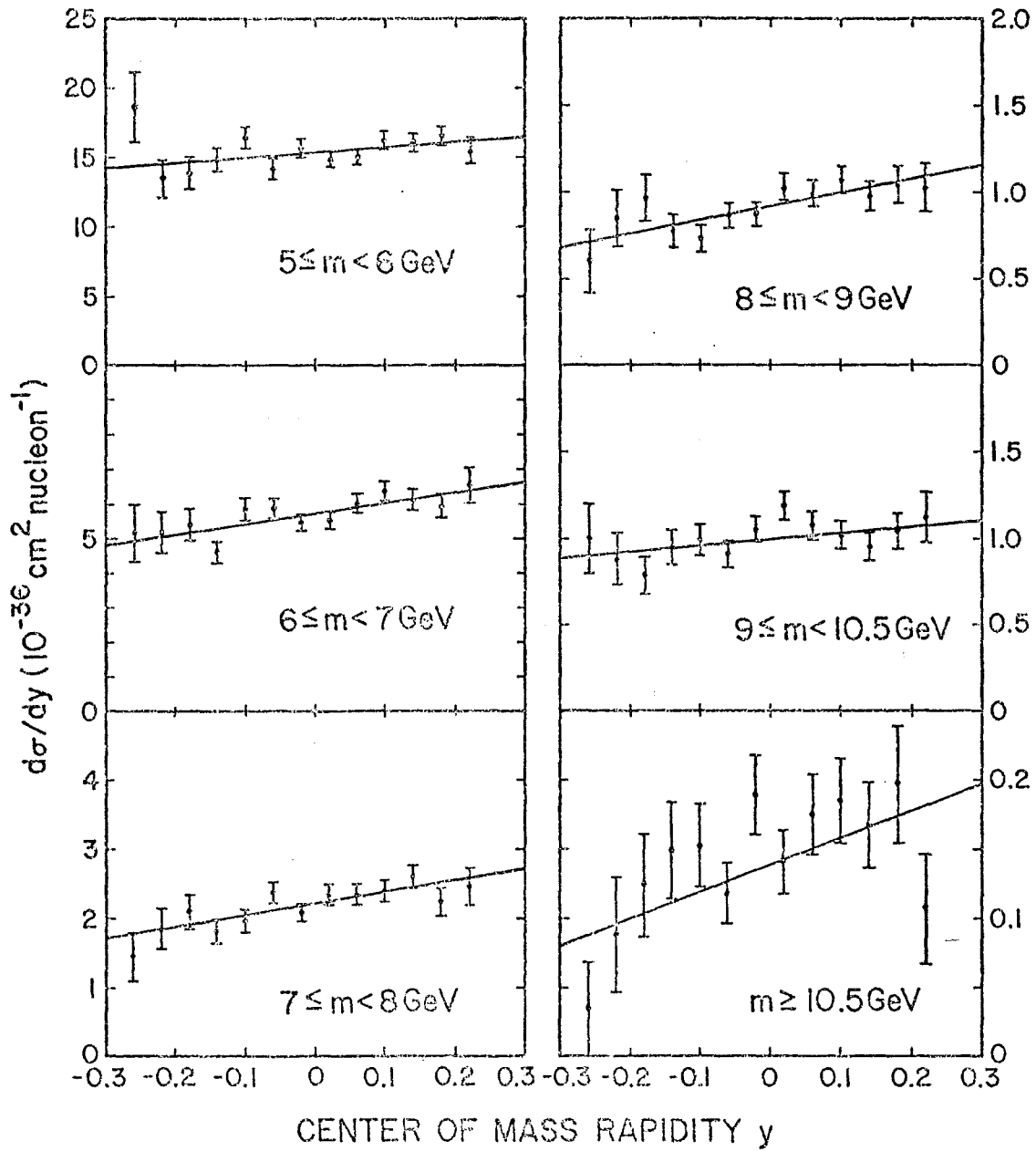
#### E. Further Corrections to the Cross-section

##### 1. Nucleon Motion

Because the target nucleons are in motion within the nucleus, some collisions have more energy available than the nominal 27.43 GeV and some have less. Since the muon pair cross-section increases rapidly with energy, the net effect of the target nucleon motion is to increase the observed cross-section. The energy dependence of muon pair production has been measured by the CFS group in an experiment subsequent to the present one. We find for the continuum<sup>40</sup>

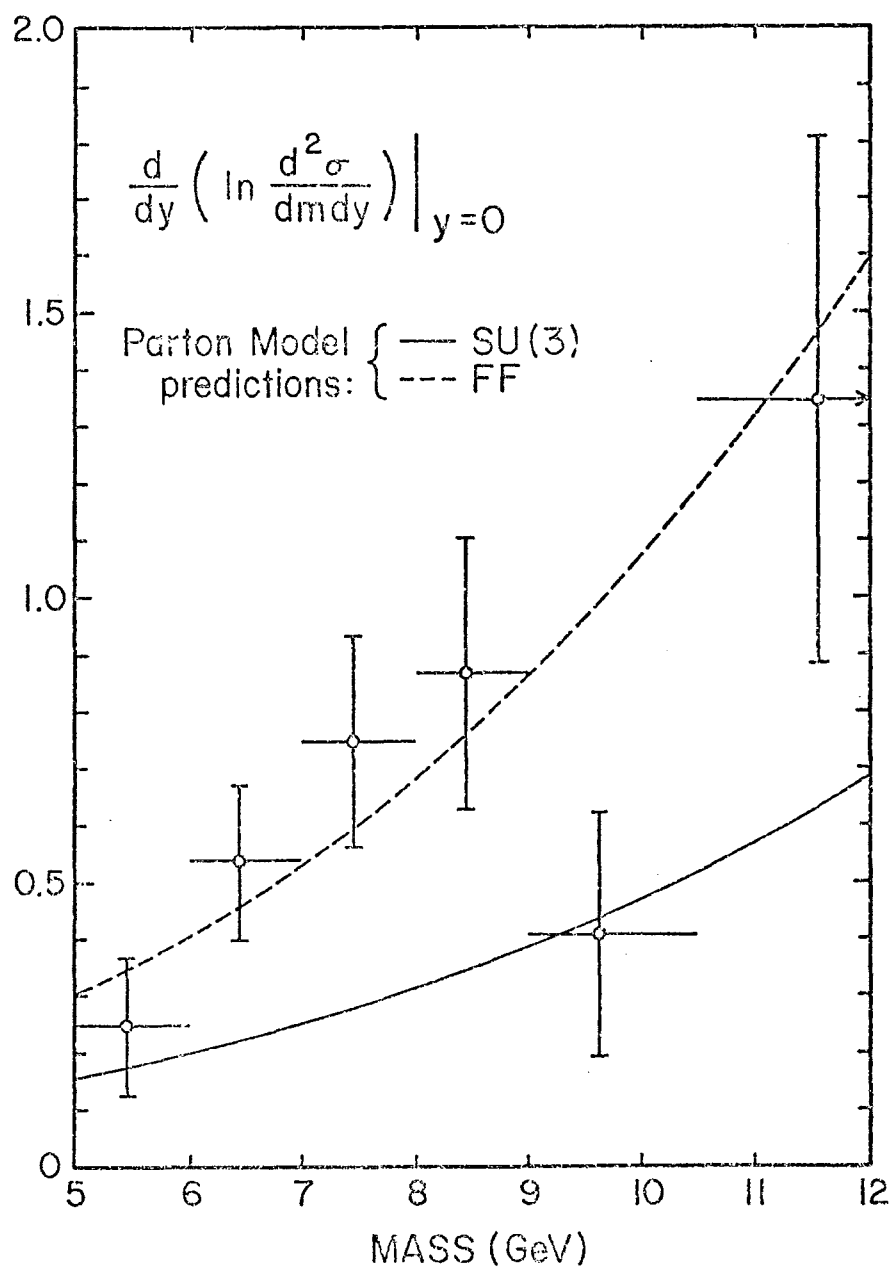
$$\left. \frac{d^2\sigma}{d\sqrt{s}dy} \right|_{y=.2} \propto e^{-(25.3 \pm .2 \pm .6)\sqrt{s}}$$

We have estimated the correction due to nucleon motion by Monte



DIFFERENTIAL CROSS-SECTION VS. RAPIDITY

FIGURE 39



RELATIVE RAPIDITY SLOPE VS. MASS

FIGURE 40



Carlo using both a Fermi gas model of the nucleus<sup>41</sup> and a nucleon momentum distribution measured at high energy<sup>33</sup> given by

$$\frac{dN}{dp} \propto \frac{1}{1 + e^{(p-p_0)/\lambda}}$$

where  $p_0 = 0.1$  GeV and  $\lambda = 0.05$  GeV. Since most of our data were obtained with the platinum target, a reasonable value for the momentum cutoff in the Fermi gas model is  $0.26$  GeV<sup>42</sup>; we have also tried  $0.21$  GeV and  $0.31$  GeV in order to estimate the uncertainty of the correction. Our results can be parametrized by the form

$$\left( \frac{d^2\sigma}{dm dy} \right)_{\text{observed}} / \left( \frac{d^2\sigma}{dm dy} \right)_{\text{produced}} = e^{a(m-m_0)} \quad (1)$$

with  $m_0 = 3$  GeV and  $a$  as given in Table XX for the various nucleon momentum distributions. We correct the cross-section using  $a = 0.03 \pm 0.01$  GeV<sup>-1</sup>. The correction is applied also to the  $T$ , since the  $T$  appears to have energy dependence similar to that of the continuum<sup>39</sup>.

The effect of nucleon motion on the transverse momentum distribution is to smear the transverse momentum by about 30 MeV (r.m.s). Since the r.m.s. apparatus resolution width is  $\sim 200$  MeV, this is a negligible effect. There is a net effect on the rapidity distribution: on the average, nucleon motion decreases the observed rapidity by 0.03 units, i.e.

Table XX

## Nucleon Motion Correction Parameters

## a. Fermi Gas Model

$p$	(GeV)	$a$ (GeV <sup>-1</sup> )
0.21		0.02
0.26		0.03
0.31		0.04

## b. Experimental Fit (Ref. 32)

$$a = 0.023 \text{ GeV}^{-1}$$

$$\left( E \frac{d^3\sigma}{dp^3} \right)_{\text{corrected}} \bigg|_y = \left( E \frac{d^3\sigma}{dp^3} \right)_{\text{uncorrected}} \bigg|_{y + 0.03} .$$

An additional effect is to smear the rapidity by 0.02 units r.m.s.; this is of negligible importance due to the weak rapidity dependence of the cross-section.

## 2. Radiative Corrections

In addition to the effect on the resolution shape mentioned in section C above, radiative corrections change the shape and normalization of the continuum mass spectrum. This occurs through the emission of photons and the consequent reduction of the mass of the muon pair, and since the muon pair cross-section falls exponentially with mass, it is a small effect. I have computed it following Ref. 37 and find that it can be parametrized by the form (1) with  $a = -0.0046 \text{ GeV}^{-1}$  and  $m_0 = -0.95 \text{ GeV}$ . The combined effect of nucleon motion and radiation is then corrected for by multiplying the cross-section by the factor

$$\exp \left[ -.0254 (m - 3.715) \right] .$$

## 3. T Acceptance

The acceptances used above were computed using the continuum production model, i.e. assuming

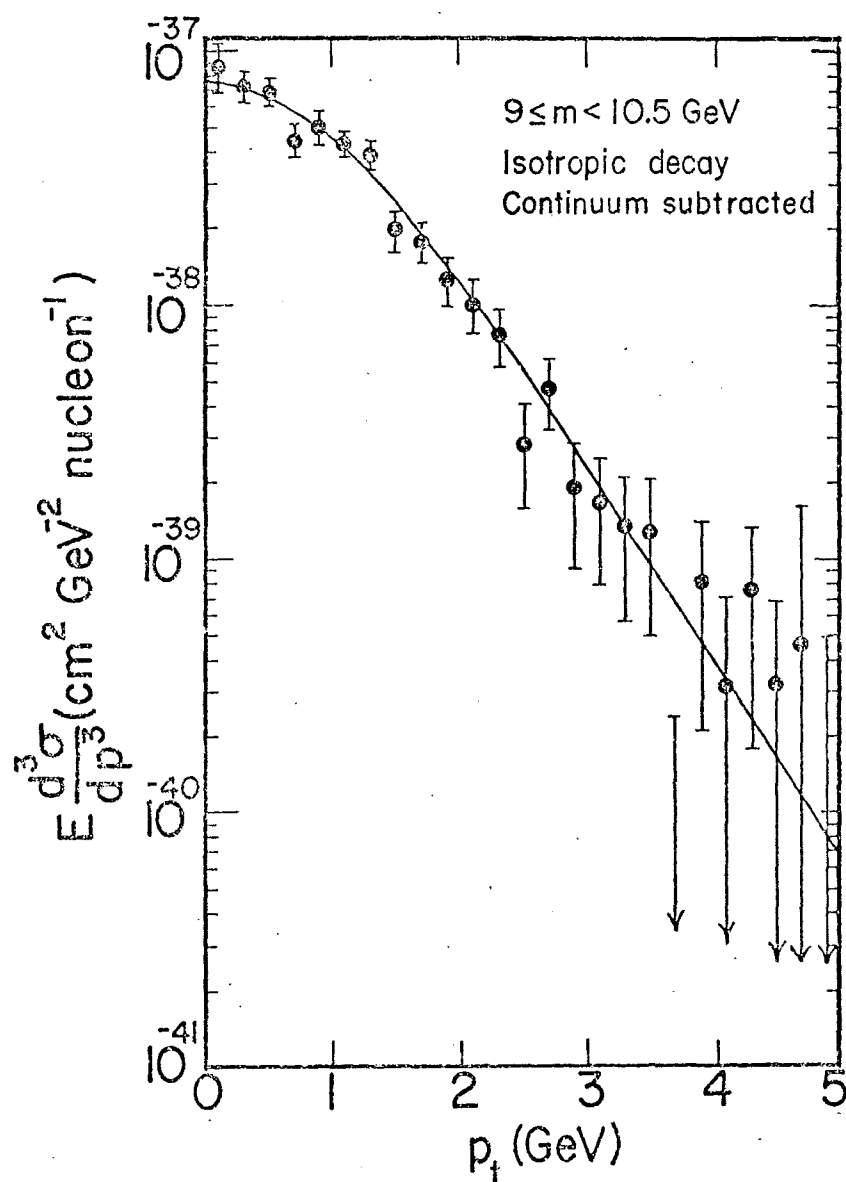
$$\frac{d^4\sigma}{dm dy dp_t d\cos\theta^*} \propto e^{-.95m} \frac{p_t}{\left[1 + \left(\frac{p_t}{2.8}\right)^2\right]^6} \left(1 + \cos^2\theta^*\right).$$

This acceptance is incorrect for the  $T$  for two reasons:

1) the  $T$  presumably decays isotropically<sup>43</sup>, and 2)  $T$ 's are produced with a larger average transverse momentum than is the continuum. The first effect increases the  $T$  acceptance by 30%, while the second decreases it. To find the size of the second effect, I subtracted the continuum transverse momentum fit (Equation D.1) from the transverse momentum distribution of the data in the 9 to 10.5 GeV mass bin and corrected the excess events using the transverse momentum acceptance generated assuming isotropic decay. (The isotropic decay  $p_t$  acceptance is larger than the  $1 + \cos^2\theta$   $p_t$  acceptance by 30% at zero  $p_t$ , which decreases to 10% at 5 GeV  $p_t$ .) The continuum-subtracted  $T$   $p_t$  distribution is shown in Figure 41. The curve represents the fit

$$E \frac{d^3\sigma}{dp^3} \propto \left[1 + \left(\frac{p_t}{3.39}\right)^2\right]^{-6}.$$

Using this fit in the Monte Carlo, and assuming isotropic decay, I find that the  $T$  acceptance is 14% larger than the continuum mass acceptance at 9.5 GeV.



CONTINUUM-SUBTRACTED CROSS-SECTION IN THE ENHANCEMENT REGION VS.  $p_t$

FIGURE 41

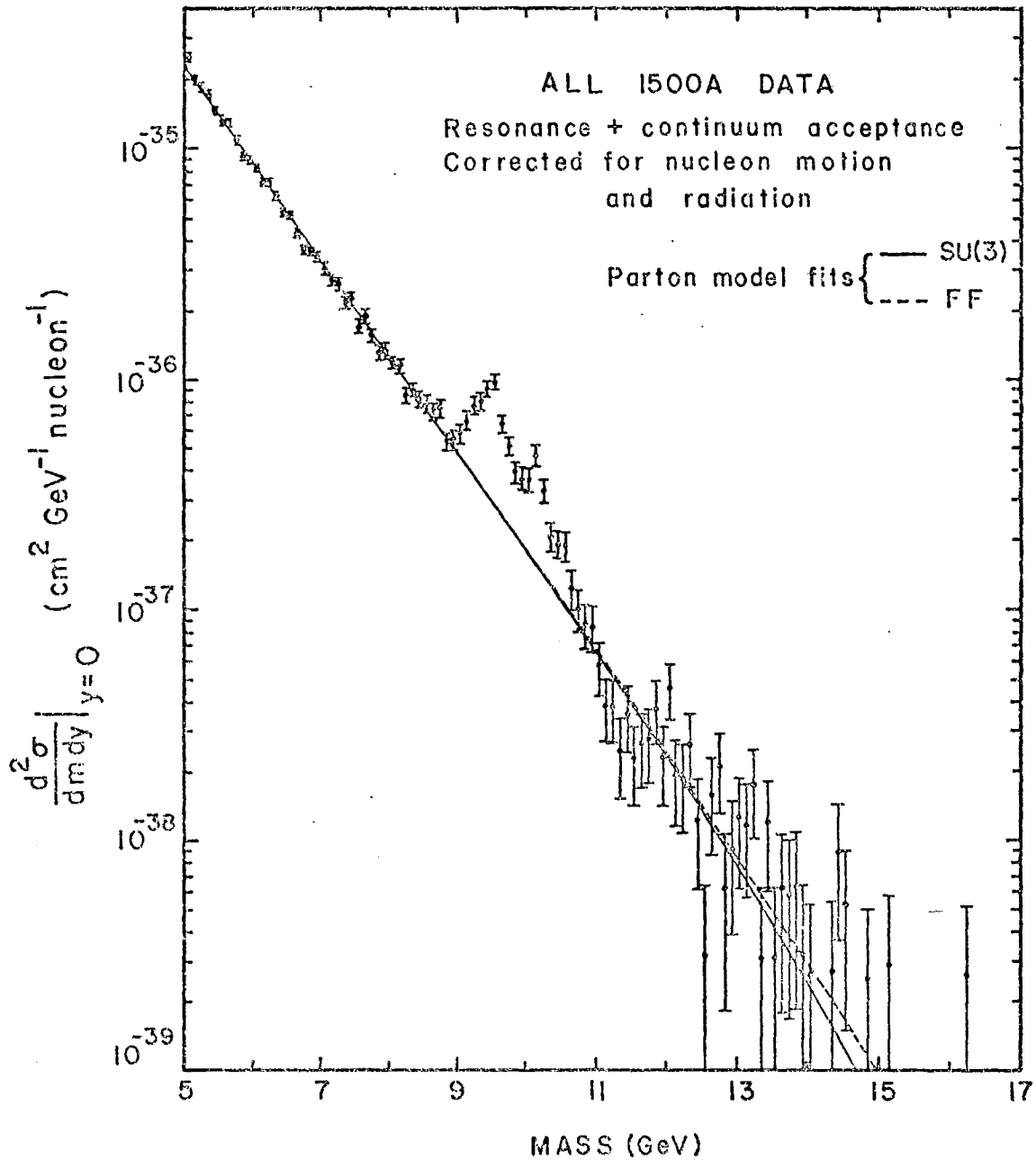
Applying all of the above corrections, I obtain the cross-sections and fit parameters of Figure 42 and Tables XXI and XXII.

Note that assuming isotropic decay for the T increases  $\langle p_t \rangle_T$  to  $1.43 \pm 0.08$  GeV.

#### F. Estimate of Systematic Errors

There is an overall absolute normalization uncertainty of  $\pm 5\%$  due to the uncertainty of the SEM calibration,  $\pm 4\%$  due to the statistical error of the Be target data sample, and another  $\pm 5\%$  due to the uncertainties of the efficiency and the length and density of the beryllium target (the 4.4% efficiency error is the dominant contribution). The nucleon motion correction contributes a  $\pm 4\%$  error in the normalization of the cross-section per nucleon at 7 GeV mass and a  $\pm 1\%$  error in the exponential slope. I estimate the systematic uncertainty of the acceptance to be  $\pm 10\%$  overall and  $\pm 10\%$  in the normalization of low mass relative to high mass; the latter contributes  $\pm 1\%$  to the error of the exponential slope. Adding these in quadrature, the normalization at 7 GeV is uncertain by  $\pm 13\%$ .

There are in addition the model dependences of the acceptance calculation and the extrapolation to nucleon target. If isotropic decay were assumed for the continuum, the acceptance would be 30% higher and the continuum cross-section 23% lower. Although we measure the A-dependence well at low mass, at high mass the use of linear A-dependence must be regarded as an assumption



DIFFERENTIAL CROSS-SECTION PER NUCLEON VS. MASS

FIGURE 42

TABLE XXI

DIFFERENTIAL CROSS-SECTION VS. MASS  
(after all corrections)

Mass (GeV)	Events	Background	Acceptance (%)	$\frac{d^2\sigma}{dm dy}$ y=0	(fb/nucleon)
5.05	1454	97	.1210 $\pm$ .0023	24750 $\pm$ 784	
5.15	1311	84	.1364 $\pm$ .0026	19810 $\pm$ 648	
5.25	1294	79	.1461 $\pm$ .0028	18270 $\pm$ 603	
5.35	1193	64	.1460 $\pm$ .0029	16940 $\pm$ 584	
5.45	1089	35	.1592 $\pm$ .0032	14470 $\pm$ 519	
5.55	1068	35	.1720 $\pm$ .0035	13090 $\pm$ 475	
5.65	1037	20	.1720 $\pm$ .0036	12860 $\pm$ 479	
5.75	972	21	.1910 $\pm$ .0040	10800 $\pm$ 411	
5.85	886	24	.2028 $\pm$ .0044	9198 $\pm$ 364	
5.95	832	11	.1996 $\pm$ .0045	8875 $\pm$ 366	
6.05	825	9	.2134 $\pm$ .0049	8229 $\pm$ 342	
6.15	743	6	.2219 $\pm$ .0052	7129 $\pm$ 310	
6.25	757	5	.2254 $\pm$ .0056	7145 $\pm$ 313	
6.35	697	3	.2364 $\pm$ .0060	6272 $\pm$ 285	
6.45	632	3	.2539 $\pm$ .0065	5279 $\pm$ 250	
6.55	604		.2494 $\pm$ .0067	5147 $\pm$ 251	
6.65	546	3	.2658 $\pm$ .0073	4331 $\pm$ 220	
6.75	471		.2713 $\pm$ .0078	3671 $\pm$ 199	
6.85	500	2	.2918 $\pm$ .0085	3600 $\pm$ 192	
6.95	474	1	.2925 $\pm$ .0089	3402 $\pm$ 187	
7.05	417		.2877 $\pm$ .0091	3041 $\pm$ 177	
7.15	384		.2988 $\pm$ .0098	2690 $\pm$ 163	
7.25	386	1	.3114 $\pm$ .0106	2581 $\pm$ 158	
7.35	335		.3211 $\pm$ .0113	2173 $\pm$ 141	
7.45	326		.3043 $\pm$ .0115	2225 $\pm$ 149	
7.55	286	1	.3444 $\pm$ .0128	1715 $\pm$ 120	
7.65	298		.3245 $\pm$ .0130	1898 $\pm$ 134	
7.75	251		.3334 $\pm$ .0137	1552 $\pm$ 117	
7.85	236		.3686 $\pm$ .0153	1317 $\pm$ 102	
7.95	236		.3612 $\pm$ .0160	1340 $\pm$ 105	
8.05	214		.3680 $\pm$ .0068	1190 $\pm$ 84	
8.15	199		.3543 $\pm$ .0070	1146 $\pm$ 84	
8.25	155		.3711 $\pm$ .0075	850 $\pm$ 70	
8.35	161	1	.3671 $\pm$ .0078	885 $\pm$ 72	
8.45	153		.3801 $\pm$ .0083	815 $\pm$ 68	



TABLE XXI (continued)

Mass	Events	Acceptance	Cross-Section
8.55	149	.3841 $\pm$ .0088	783 $\pm$ 67
8.65	147	.4072 $\pm$ .0096	727 $\pm$ 62
8.75	144	.3892 $\pm$ .0097	743 $\pm$ 65
8.85	115	.4266 $\pm$ .0107	540 $\pm$ 52
8.95	114	.4177 $\pm$ .0111	546 $\pm$ 53
9.05	123	.4278 $\pm$ .0120	574 $\pm$ 54
9.15	143	.4312 $\pm$ .0128	660 $\pm$ 59
9.25	167	.4343 $\pm$ .0134	763 $\pm$ 64
9.35	187	.4637 $\pm$ .0147	798 $\pm$ 64
9.45	222	.4860 $\pm$ .0159	902 $\pm$ 67
9.55	238	.4858 $\pm$ .0166	965 $\pm$ 71
9.65	156	.4814 $\pm$ .0174	636 $\pm$ 56
9.75	124	.4787 $\pm$ .0180	508 $\pm$ 49
9.85	101	.5063 $\pm$ .0197	390 $\pm$ 42
9.95	95	.5029 $\pm$ .0204	368 $\pm$ 41
10.05	89	.4768 $\pm$ .0206	363 $\pm$ 42
10.15	106	.4441 $\pm$ .0209	463 $\pm$ 50
10.25	79	.4695 $\pm$ .0227	326 $\pm$ 40
10.35	58	.5438 $\pm$ .0254	206 $\pm$ 29
10.45	54	.5408 $\pm$ .0265	192 $\pm$ 28
10.55	47	.4771 $\pm$ .0252	189 $\pm$ 29
10.65	30	.4655 $\pm$ .0262	123 $\pm$ 24
10.75	25	.4733 $\pm$ .0276	101 $\pm$ 21
10.85	22	.4902 $\pm$ .0294	85.5 $\pm$ 18.9
10.95	21	.4755 $\pm$ .0305	83.9 $\pm$ 19.1
11.05	15	.4999 $\pm$ .0115	56.9 $\pm$ 14.7
11.15	11	.5440 $\pm$ .0126	38.2 $\pm$ 11.6
11.25	11	.5440 $\pm$ .0131	38.1 $\pm$ 11.5
11.35	7	.5364 $\pm$ .0136	24.5 $\pm$ 9.3
11.45	10	.5314 $\pm$ .0142	35.3 $\pm$ 11.2
11.55	7	.5765 $\pm$ .0156	22.7 $\pm$ 8.6
11.65	8	.5702 $\pm$ .0163	26.2 $\pm$ 9.3
11.75	8	.5453 $\pm$ .0167	27.3 $\pm$ 9.7
11.85	11	.5500 $\pm$ .0174	37.1 $\pm$ 11.3
11.95	7	.5738 $\pm$ .0188	22.6 $\pm$ 8.6
12.05	14	.5650 $\pm$ .0195	45.8 $\pm$ 12.3
12.15	6	.5731 $\pm$ .0206	19.3 $\pm$ 7.9
12.25	6	.5951 $\pm$ .0221	18.5 $\pm$ 7.6
12.35	8	.5595 $\pm$ .0227	26.2 $\pm$ 9.3
12.45	4	.5992 $\pm$ .0246	12.2 $\pm$ 6.1

TABLE XXI (continued)

Mass	Events	Acceptance	Cross-Section
12.55	1	.5745 $\pm$ .0249	3.2 $\pm$ 3.2
12.65	5	.5798 $\pm$ .0265	15.7 $\pm$ 7.1
12.75	7	.6016 $\pm$ .0282	21.1 $\pm$ 8.0
12.85	2	.5803 $\pm$ .0286	6.2 $\pm$ 4.4
12.95	3	.5901 $\pm$ .0303	9.2 $\pm$ 5.3
13.05	4	.5808 $\pm$ .0316	12.4 $\pm$ 6.2
13.15	4	.6252 $\pm$ .0349	11.5 $\pm$ 5.8
13.25	6	.6174 $\pm$ .0361	17.4 $\pm$ 7.2
13.35	1	.5742 $\pm$ .0368	3.1 $\pm$ 3.1
13.45	4	.5961 $\pm$ .0384	12.0 $\pm$ 6.0
13.55	1	.5705 $\pm$ .0399	3.1 $\pm$ 3.1
13.65	2	.5664 $\pm$ .0414	6.3 $\pm$ 4.5
13.75	2	.6047 $\pm$ .0448	5.9 $\pm$ 4.2
13.85	2	.5573 $\pm$ .0443	6.3 $\pm$ 4.5
13.95	1	.5485 $\pm$ .0470	3.2 $\pm$ 3.2
14.05	1	.6739 $\pm$ .0551	2.6 $\pm$ 2.6
14.15		.6564 $\pm$ .0575	0. $\pm$ 2.7
14.25		.6426 $\pm$ .0591	0. $\pm$ 2.7
14.35	1	.6439 $\pm$ .0637	2.7 $\pm$ 2.7
14.45	3	.5847 $\pm$ .0628	8.9 $\pm$ 5.2
14.55	2	.6539 $\pm$ .0690	5.3 $\pm$ 3.8
14.65		.6495 $\pm$ .0723	0. $\pm$ 2.7
14.75		.6119 $\pm$ .0718	0. $\pm$ 2.8
14.85	1	.6836 $\pm$ .0829	2.5 $\pm$ 2.5
14.95		.9247 $\pm$ .0995	0. $\pm$ 1.9
15.05		.5667 $\pm$ .0098	0. $\pm$ 3.0
15.15	1	.5884 $\pm$ .0104	2.9 $\pm$ 2.9
15.25		.5770 $\pm$ .0108	0. $\pm$ 3.0
15.35		.5858 $\pm$ .0114	0. $\pm$ 2.9
15.45		.5867 $\pm$ .0119	0. $\pm$ 2.9
15.55		.5829 $\pm$ .0125	0. $\pm$ 2.9
15.65		.5833 $\pm$ .0131	0. $\pm$ 2.9
15.75		.6152 $\pm$ .0142	0. $\pm$ 2.7
15.85		.6385 $\pm$ .0151	0. $\pm$ 2.6
15.95		.6046 $\pm$ .0154	0. $\pm$ 2.8
16.05		.6011 $\pm$ .0161	0. $\pm$ 2.8
16.15		.6341 $\pm$ .0174	0. $\pm$ 2.6
16.25	1	.6390 $\pm$ .0183	2.6 $\pm$ 2.6
16.35		.5867 $\pm$ .0184	0. $\pm$ 2.8
16.45		.6222 $\pm$ .0198	0. $\pm$ 2.7

TABLE XXII

Resonance Plus Continuum Fits  
(Corrected for nucleon motion, radiation, and T acceptance)

	2-resonance	3-resonance
A (cm <sup>2</sup> /GeV)	(3.24±.03)x10 <sup>-36</sup>	(3.23±.03)x10 <sup>-36</sup>
b (GeV <sup>-1</sup> )	.977±.007	.978±.007
m <sub>1</sub> (GeV)	9.467±.015	9.465 <sup>+.015</sup> <sub>-.014</sub>
(B $\frac{d\sigma}{dy}$ ) <sub>1</sub> (cm <sup>2</sup> )	(3.41±.20)x10 <sup>-37</sup>	(3.34±.20)x10 <sup>-37</sup>
Width (GeV)	.206 <sup>+.013</sup> <sub>-.011</sub>	.195 <sup>+.013</sup> <sub>-.012</sub>
m <sub>2</sub> -m <sub>1</sub> (GeV)	.691 <sup>+.028</sup> <sub>-.027</sub>	.653 <sup>+.037</sup> <sub>-.040</sub>
(B $\frac{d\sigma}{dy}$ ) <sub>2</sub> (cm <sup>2</sup> )	(1.33±.14)x10 <sup>-37</sup>	(1.27 <sup>+.14</sup> <sub>-.16</sub> )x10 <sup>-37</sup>
m <sub>3</sub> -m <sub>1</sub> (GeV)		1.10 <sup>+.16</sup> <sub>-.17</sub>
(B $\frac{d\sigma}{dy}$ ) <sub>3</sub> (cm <sup>2</sup> )		(1.58 <sup>+.145</sup> <sub>-1.06</sub> )x10 <sup>-38</sup>
$\chi^2$ /DF	72.7/62	70.2/60
C.L.	.167	.172

## NOTE

1. Errors are statistical only. The systematic uncertainties in A and b are ±13% and ±1.4% respectively. The systematic uncertainty of resonance cross-sections is ±15%. (See Section V.F.)
2. For details of mass calibration see Appendix.

motivated by theoretical expectation, so this is also properly considered a model dependence.

The normalization uncertainty of the T is  $\pm 15\%$ ; it is larger than the uncertainty at 7 GeV due to the increased contribution ( $\pm 7\%$ ) of the nucleon motion correction. The nucleon motion correction to the T cross-section is of course dependent on the T energy dependence, which is not well known.

## VI. DISCUSSION AND CONCLUSIONS

### A. Nature of the T's

Below I discuss the "quarkonium" hypothesis: that the T's are positronium-like bound states of a new quark and its antiquark. In general the best argument against the T's being something else is the success of the quarkonium hypothesis. However, some other hypotheses concerning the nature of the T's can be addressed using the available experimental evidence, so I will discuss these first.

#### 1. Are they conventional vector mesons?

On the basis of our data alone, this seems highly unlikely, considering that the  $\rho$  is already 100 MeV wide and its excited states are considerably wider. Now that the T has been observed in  $e^+e^-$  annihilation at DESY<sup>44</sup>, its width is known to be  $<18$  MeV, and the best estimate is  $\Gamma \approx 50$  keV<sup>45</sup>, so it is clear that some new quantum number or mechanism must be responsible for preventing the T from decaying rapidly into one of the myriad available multihadron states.

#### 2. Is it the Z?

There are of course theoretical biases against this hypothesis. First, the mass of the Z is expected<sup>46</sup> to be  $\sim 70$  GeV. Second, why are there more than one of them? Experimentally, if the T is the Z one might expect to observe interference between the production of T's and the production of virtual photons<sup>47</sup>. This would show up as an asymmetry in energy of the  $\mu^+$  versus the  $\mu^-$ . To

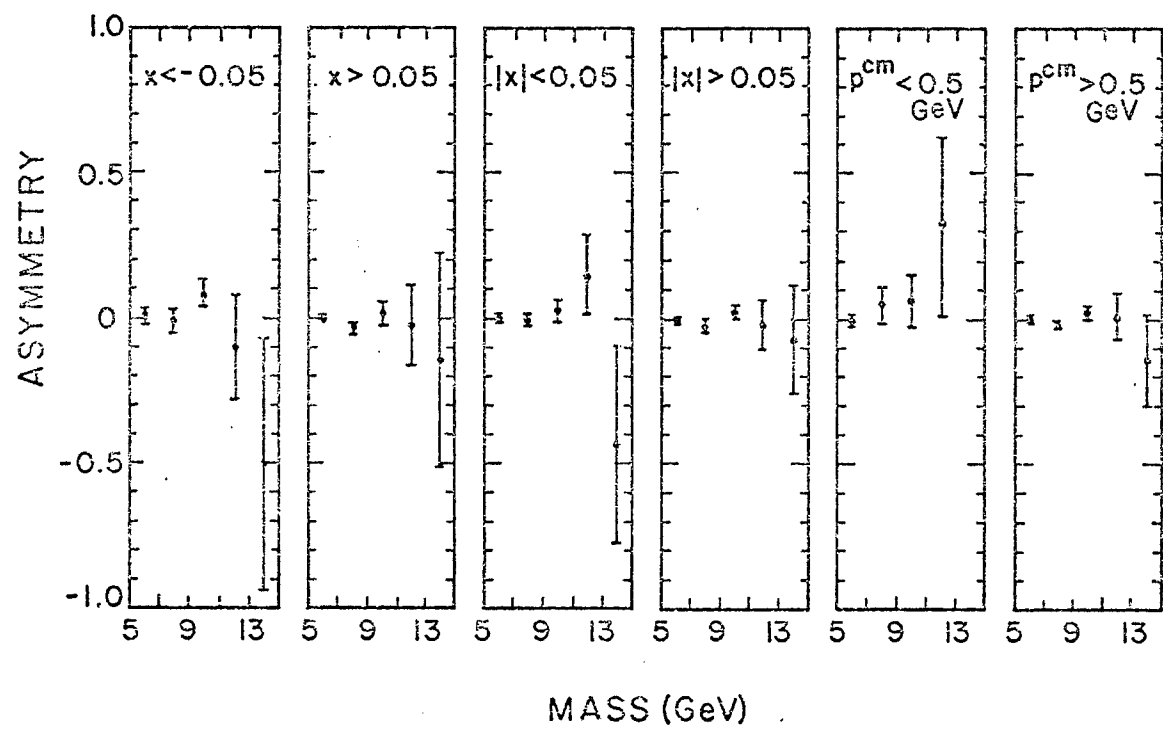
investigate this we define the asymmetry

$$A = \frac{N_+ - N_-}{N_+ + N_-}$$

where  $N_+(N_-)$  is the number of events in which the positive muon is more (less) energetic than the negative muon. This asymmetry will be zero in the absence of interference. Clearly in the rest frame of the produced  $T$  the energies are always equal, so no effect can be observed when the  $T$  is produced at rest in the CMS. Figure 43 presents the asymmetry versus mass in various bins of Feynman  $x$  and CMS momentum. The observed symmetry at  $x=0$  shows that the apparatus is not biasing the measurement. In the bins away from zero where a legitimate effect is possible, none is seen. (Note that our Feynman  $x$  acceptance covers about  $\pm 0.1$  units at 5 GeV mass and  $\pm 0.5$  units at 15 GeV.)

### 3. Is it the Higgs?

The Higgs meson is supposed to couple to vector mesons in proportion to their mass-squared<sup>48</sup>, so its coupling to muon pairs is 40,000 times as strong as its coupling to electron pairs. In the CFS electron pair data<sup>49</sup> there is an isolated cluster of 6 events at 9.5 GeV mass, not inconsistent with the 3 expected if the  $T$  couples equally to muons and to electrons. The  $T$  decay into electrons has also been observed at the CERN ISR<sup>50</sup>, but to compare their results to ours one must know the energy dependence of  $T$  production.



ASYMMETRY VS. MASS

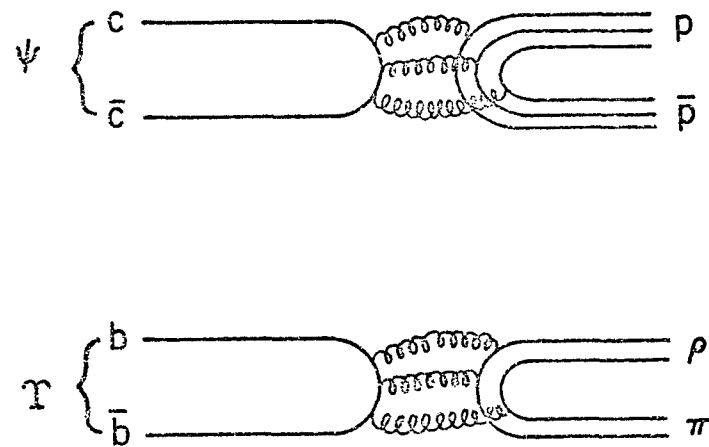
FIGURE 43

The observed energy dependence is consistent with the hypothesis of equal coupling to muons and electrons<sup>39</sup>. Finally, the expected<sup>48</sup> cross-section for a 9.5 GeV Higgs meson in  $e^+e^-$  annihilation is  $10^6$  times smaller than the observed<sup>44</sup>  $T$  cross-section.

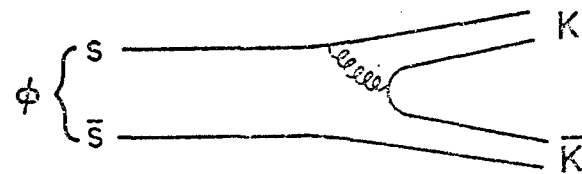
#### 4. Quarkonium

In view of the success of the charmonium hypothesis<sup>22,51</sup> for the  $T$  family, it is natural to try to explain the  $T$  in similar fashion. There is now a large body of literature<sup>51-57</sup> which attempts to identify the  $T$ ,  $T'$ , and  $T''$  with the first three  $S$  states of a  $q\bar{q}$  system, where  $q$  is a new heavy ( $m_q \cong 5$  GeV) quark. The narrow widths of the  $T$ 's then result from the difficulty of  $q\bar{q}$  annihilation into lighter quarks (as also in the case of the  $\phi$  and the  $\psi$ ), a process which in QCD must proceed via at least 3 gluons (see Figure 44a) in order to conserve color and C-parity. Such processes, in which the quarks of the initial state are not found in the final state, are suppressed by a mechanism which is not entirely understood but which has come to be known as the Okubo-Zweig-Iizuka (OZI) rule<sup>58</sup>. The number of narrow  $\mu^+\mu^-$  resonances depends on the threshold for OZI-allowed decay (see Figure 44b) and increases with the mass of the quark<sup>52</sup>, so that the  $\phi$  can (just barely) decay into  $K\bar{K}$  while the  $\psi$  and  $\psi'$  are both too light to decay into  $D\bar{D}$ . In the case of the  $T$  family, theory predicts that there should be at least three and possibly four<sup>52,55</sup> OZI-stable  $\mu^+\mu^-$  resonances. Data obtained by the CFS group subsequently to the





a. OZI-suppressed



b. OZI-allowed

# EXAMPLES OF QUARKONIUM DECAYS

FIGURE 44

present experiment establish the existence of the  $T''$  at the level of several standard deviations<sup>59</sup>, so this prediction is borne out.

Quarkonium calculations are usually done using a non-relativistic potential model for the interaction of two quarks, which is reasonable in the case of the  $T$  (somewhat less so for the  $\psi$ ) since the quarks are so heavy. (Gottfried<sup>51</sup> estimates that the quarks in the  $\psi'$  and  $T'$  have  $\beta^2 \approx 0.3$  and  $0.1$  respectively.) A potential which successfully describes the  $T$  family is<sup>52</sup>

$$V(r) = -\frac{4}{3} \frac{\alpha_s(m)}{r} + \lambda r \quad (1)$$

where  $r$  is the quark separation,  $\alpha_s(m)$  is the QCD coupling "constant", and  $m$  is the mass of the quark. The first (coulomb-like) term has the short distance behavior expected in QCD, while the linear term serves to confine the quarks. This was the potential used in most of the earliest quarkonium papers, which preceded<sup>52,53</sup> or immediately followed<sup>54</sup> our announcement in July 1977 of the observation of the  $T$ . At that time the  $T'$  had not yet been clearly resolved; using the potential (1), the various authors predicted the  $T'$  to be 420 MeV above the  $T$  in mass. Our subsequent results showed a larger mass splitting, indicating that (1) is not exactly correct. The approximate equality of the  $T$ - $T'$  and  $\psi$ - $\psi'$  mass splittings led Quigg and Rosner<sup>56</sup> to suggest that the correct moderate distance behavior might be more closely given by a

logarithmic potential, which has the property that the mass splittings are independent of the mass of the quark. Note that while the mass splitting obtained here is somewhat larger than that of charmonium, smaller splittings have been observed by the CFS group<sup>59</sup> in the larger data sample subsequently obtained ( $0.57 \pm 0.03$  GeV) and by the DESY experimenters<sup>60</sup> ( $0.56 \pm 0.01$  GeV). Theoretical efforts to refine the interquark potential are continuing<sup>57</sup>.

The new quark of which the T family is composed is usually thought to be a member of a third doublet of quarks, the existence of which was first proposed<sup>61</sup> to allow the introduction of CP violation into the Weinberg-Salam model of weak interactions. Theoretical interest in the new doublet was abetted by the high-y anomaly<sup>62</sup> observed in neutrino results (which later proved incorrect<sup>63</sup>). The quark-lepton analogy (which originally motivated the postulation of the charmed quark<sup>23</sup>) also suggests the existence of a new quark doublet, now that the heavy lepton  $\tau$  has been found<sup>64</sup>, presumably accompanied by its own brand of neutrino. The new doublet would be made up of a "top" quark  $t$  (possessing the attribute of "truth") and a "bottom" quark  $b$  (blessed with "beauty"). If the pattern of the charmed-strange doublet is repeated, the  $b$  quark (with charge  $-\frac{1}{3}$ ) is the lighter of the two, and the  $t$  quark (with charge  $\frac{2}{3}$ ) the heavier. Our observed cross-sections together with the calculations of several authors<sup>54</sup> suggest that the T is made of quarks of charge  $1/3$

rather than  $2/3$  (see Table III of Innes et al.<sup>1</sup>). The  $T$  then consists of  $b\bar{b}$ : "bottomonium." This charge assignment has been verified by the measurement at DESY of the  $T$  and  $T'$  leptonic widths<sup>45,60</sup>. Given then that the  $T$  is  $b\bar{b}$ , the  $t$  quark must indeed be heavier than the  $b$ , since a charge  $-2/3$  quarkonium resonance between the  $\psi$  and the  $T$  would have an even larger ratio of signal-to-continuum than the  $T$  and thus could not have been overlooked in our data. In this context the increased data sample published in Ueno et al.<sup>59</sup> allows us to rule out the existence of a  $t\bar{t}$  resonance below a mass of 16.5 GeV.

The dominant production mechanism for quarkonium  $S$  states is thought to be<sup>65</sup> a cascade process in which two gluons coalesce into a  $P$  state followed by the decay of the  $P$  state into an  $S$  state and a photon. (This dominates direct production via gluons since three gluons are needed to couple to an  $S$  state. Direct production via quark-antiquark annihilation is smaller by a factor  $\sim 50$ <sup>66</sup>). Only  $P$  states which are below OZI-allowed decay threshold will contribute, since those above threshold decay dominantly into hadrons containing a single new quark and have negligible branching ratios into  $S$  states. In the case of charmonium, the OZI-allowed threshold is evidently just above the  $\psi'$ , so the  $\psi$  is fed from  $P$  states but the  $\psi'$  is not. This may explain the small ratio of  $\psi'$  to  $\psi$  production which we observed in proton-nucleon collisions<sup>67</sup>:

$$\left( B \frac{d\sigma}{dy} \right)_{y=0}^{\psi'} / \left( B \frac{d\sigma}{dy} \right)_{y=0}^{\psi} = 0.018 \pm 0.006.$$

There remains a difficulty in the  $T$  case. The  $\psi'$  decays half the time into  $\psi$ , and the  $T'$  might be expected<sup>51</sup> to decay into  $T$  at a similar rate since the mass differences are comparable. Since we cannot distinguish experimentally between  $T'$ 's from  $T'$  decay and  $T'$ 's from other sources, our observed ratio of  $T'$  to  $T$  production

$$\left( B \frac{d\sigma}{dy} \right)_{y=0}^{T'} / \left( B \frac{d\sigma}{dy} \right)_{y=0}^T = 0.38 \pm 0.05$$

would then imply that the primordial rate of  $T'$  production is approximately equal to or greater than the primordial rate of  $T$  production, which is difficult to understand if the  $T'$  is really a radial excitation of the  $T$ . Evidently if the quarkonium hypothesis is correct, the rate of  $T' \rightarrow T + \text{anything}$  must be considerably smaller than the corresponding charmonium rate. Why this should be so is not completely understood, though Gottfried<sup>51</sup> has given an argument which reduces the expected rate by a factor of  $\sim 10$ . Whether or not this is a sufficient reduction is uncertain.

Experimental evidence in support of the cascade hypothesis for psion production has recently been obtained by the BNL-CERN-Syracuse-Yale group at the CERN ISR<sup>68</sup>. They observe a peak in the  $\gamma\psi$  mass spectrum at a mass of 3.5 GeV, suggesting that  $43 \pm 21\%$  of  $\psi$ 's are produced via photonic decay of the  $\chi(3.5)$ .

Cascade production of the T is supported by the large  $\langle p_t \rangle$  of the T. Using a P state-ground state mass splitting of 0.49 GeV predicted by Thacker, Quigg, and Rosner<sup>57</sup>, I find that the decay of the P state contributes 1/2 GeV of momentum in quadrature. This is ~~not~~ quite enough to account for the difference in  $\langle p_t \rangle$  between the T and the continuum; however, it is not expected to be enough, since I have neglected the additional  $p_t$  contributed by more massive P states.

## B. Nature of the Continuum: The Parton Model

### 1. The naive parton model

The only current theory of the continuum is the parton model (with or without elaborations from QCD), in which massive virtual photons arise from annihilation of quarks with antiquarks. In the original ("naive") version<sup>3</sup> transverse momenta and masses of the quarks were assumed to be negligible compared with the virtual photon mass and the collision energy, and gluonic corrections were not considered (not surprising since QCD had hardly been formulated at the time). These assumptions lead to simple relations between the cross-sections for massive lepton-pair production and deep inelastic lepton-nucleon scattering in terms of the momentum distributions of quarks and antiquarks within the nucleon. The differential lepton pair cross-section versus mass was given in I.A. above. For comparison with our data we want the cross-section differential also in rapidity, given by

$$\frac{d^2\sigma}{dm dy} = \left[ \frac{1}{3} \right] \frac{8\pi\alpha^2}{3m^3} G(\tau, y)$$

$$\text{where } G(\tau, y) = \tau \sum_i \lambda_i^2 f_i^{h_1}(x_1) f_i^{h_2}(x_2)$$

$$x_1 = \sqrt{\tau} e^y \quad x_2 = \sqrt{\tau} e^{-y}$$

(See I.A for definitions of variables.)

The factor of  $1/3$  is present if quarks come in three colors (as supposed in QCD); it arises as follows: The quark  $x$  distributions are measured in deep inelastic scattering, which isn't sensitive to the presence of color. However, quark-antiquark annihilation into photons can take place only between quarks and antiquarks of the same color, so if there is color only  $1/3$  of the possible  $q\bar{q}$  combinations contribute to the annihilation cross-section.

What is measured in deep inelastic scattering is the structure function  $\nu W_2(x)$ , which in the naive parton model is given by

$$\nu W_2(x) = x \sum_i \lambda_i^2 f_i(x) \quad .$$

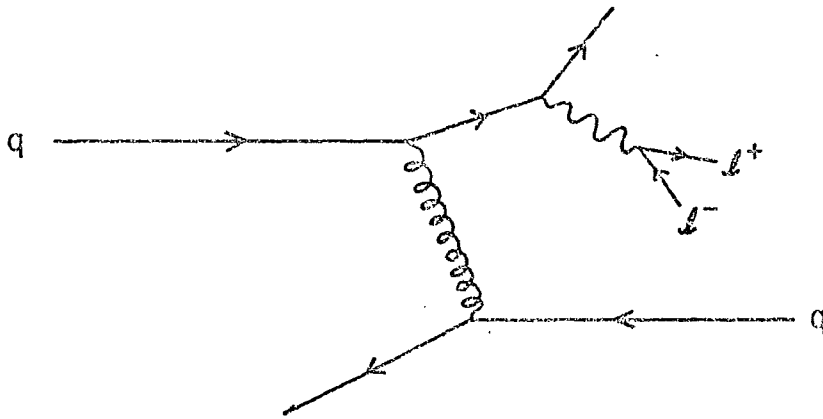
By varying the beam and target particles one can extract information about the various quark distributions and use this information to try to predict the pair cross-section. It is found experimentally that sea quark distributions fall more rapidly with increasing  $x$  than valence quark distributions, such that the quark-antiquark sea dominates at small  $x$  and the valence quarks dominate at large  $x$ . This means that the sea distributions at large  $x$  are difficult to measure in deep inelastic scattering. By contrast, massive lepton-pair production is highly sensitive to the sea at large  $x$ , since an antiquark at large  $x$  is required for the annihilation process. If the model is valid, lepton-pair production is thus a good way to measure sea  $x$  distributions. Comparison of sea distributions



measured in lepton-pair production with those measured in deep inelastic scattering also provides a potentially incisive test of the existence of color.

## 2. QCD corrections

The naive parton model predicted that  $G(\tau, y)$  and  $\nu W_2(x)$  would be independent of the virtual photon mass-squared  $Q^2$  and the collision energy  $\sqrt{s}$  at sufficiently high  $Q^2$  and  $s$ ; this is called scaling. The model also assumed that lepton pair transverse momenta would be small, based on the typical hadronic  $\langle p_t \rangle$  of 300 to 500 MeV. The observation of scaling violations in deep inelastic scattering<sup>16</sup> and of large transverse momentum in lepton-pair production shows that the naive parton model is too naive. These results stimulated much theoretical activity<sup>17,69-71</sup> aimed at calculating QCD corrections to the basic parton annihilation process. It was found that QCD corrections are not negligible even at the highest  $Q^2$ , since the lowest order gluonic effects (see Fig.5) decrease only logarithmically with  $Q^2$ . It is generally hoped, however, that the parton model equations can be retained in their naive form if the quark  $x$  distributions are allowed an additional  $Q^2$  dependence, and that this  $Q^2$  dependence is the same in deep inelastic scattering as in lepton-pair production; this is called factorization. Politzer<sup>69</sup> showed this for the one-gluon processes of Figure 5. Georgi<sup>70</sup> pointed out the importance of the higher-order process of quark-quark scattering (figure 45). Whether



# QUARK-QUARK SCATTERING

FIGURE 45

the contributions of this and other higher-order processes also factorize is currently unclear, but Politzer speculated that factorization would hold to all orders. We assume factorization in the analysis which follows.

### 3. Extraction of sea x distributions

We compare our data with the parton model using the scaling violating  $W_2^{\text{HP}}(x, Q^2)$  fit of T. Kirk<sup>72</sup>, along with a fit to the deuterium data of Atwood et al.<sup>73</sup> given by

$$\nu W_2^{\text{eD}} = \nu W_2^{\text{HP}} (2 - 0.8x) \quad .$$

We assume for lack of better knowledge that the scaling violation is the same for neutrons as for protons. We further assume, following various authors<sup>14</sup>, that sea quark distributions can be parametrized by the form  $A(1-x)^\alpha/x$  and determine the parameters  $A$  and  $\alpha$  by fitting our observed mass spectrum. We neglect possible  $Q^2$  dependence of the sea distributions. Fits are performed for two different assumptions concerning the nature of the quark-antiquark sea: 1) the sea is SU(3)-symmetric, i.e.

$$\begin{aligned} u_s(x) &= d_s(x) = s(x) = \bar{u}(x) = \bar{d}(x) = \bar{s}(x) \\ &\equiv 0(x) \quad (\text{for "ocean"}) \end{aligned}$$

where  $u$ ,  $d$ , and  $s$  are probability distributions for  $u$ ,  $d$  and  $s$

quarks in the proton and the subscript s refers to the sea; and

2) each type of sea quark has its own x dependence but the ratios are fixed following the quark model of Feynman and Field<sup>74</sup>;

$$\frac{u_s(x)}{d_s(x)} = (1-x)^3$$

$$\frac{s(x)}{d_s(x)} = 1-x \quad .$$

In the SU(3)- symmetric case we find

$$O(x) = (0.616 \pm 0.029) (1-x)^{9.05 \pm 0.16}$$

$$\chi^2 = 58 \text{ for 45 degrees of freedom}$$

$$CL = 0.10.$$

In the Feynman-Field case we find

$$d_s(x) = (0.702 \pm 0.032) (1-x)^{8.13 \pm 0.16}$$

$$\chi^2 = 52 \text{ for 45 degrees of freedom}$$

$$CL = 0.22.$$

(Note that Feynman and Field assumed  $\alpha=7$ )

The errors are statistical only and are highly correlated; they represent extreme projections of the error ellipse on the A- and

$\alpha$ - axes. There is an additional error of 0.25 in the exponent due to the uncertainty of the nucleon motion correction and the acceptance, and an absolute normalization error of 12%. These results represent measurements in the range  $0.18 < x < 0.5$ , excluding the resonance region  $0.32 < x < 0.40$ . Figure 42 compares the parton model mass spectra under the two sea assumptions with the observed mass spectrum.

#### 4. Rapidity slopes

Figure 40 compares the parton model rapidity slopes at  $y=0$  with those of the data. The large positive slopes reflect the presence of neutrons in the target, as follows: The paucity of antiquarks at large  $x$  means that at positive rapidity we observe mostly annihilation of quarks from the beam with antiquarks from the target, and vice versa at negative rapidity. The contribution of  $u\bar{u}$  to the cross-section is four times as great as the contribution of  $d\bar{d}$ , due to the quark charges. Thus even in the SU(3)-symmetric case we obtain a larger cross-section at positive rapidity than at negative, since at positive rapidity the dominant quarks are  $2/3$   $u$  and  $1/3$   $d$ , while at negative rapidity (and for Pt target) they are 47%  $u$  and 53%  $d$ . In the Feynman-Field case the effect is even stronger, since then  $\bar{u}$  in the proton is suppressed at large  $x$  by the factor  $(1-x)^3$ , and hence  $\bar{u}$  in the neutron is enhanced, since the neutron and the proton are related by isospin rotation. Annihilation of a  $u$  from a proton with a  $\bar{u}$  from a neutron then contributes more

strongly than annihilation of a  $u$  from a neutron with a  $\bar{u}$  from a proton, increasing the rapidity slope relative to the SU(3)-symmetric case.

The data are seen to prefer the Feynman-Field type model over the SU(3)-symmetric model, however caution is in order, since at large mass the  $\sqrt{s}W_2$  fits are being extrapolated beyond the range of  $Q^2$  in which they are well determined. (Possible systematic errors in the data at the 10% level are dominated by the statistical uncertainties.)

#### 5. Transverse momentum

The same gluonic processes responsible for scaling violation in deep inelastic scattering lead to large transverse momentum in lepton pair production. Many authors<sup>17,69,71</sup> have calculated the resulting transverse momentum spectra; they find that the lowest order processes diverge at  $p_t = 0$ , where perturbation techniques in QCD break down and asymptotic freedom no longer applies. The theoretical distributions have shapes roughly consistent with those of the data above  $p_t$  of 1 1/2 GeV or so. If each quark is assumed to have  $\sim 0.6$  GeV of  $\langle p_t \rangle$  arising from the quark confinement mechanism, and this is added in quadrature to the lowest order QCD contributions, the observed  $\langle p_t \rangle$  of 1.2 GeV independent of mass can be accommodated. Berger<sup>71</sup> has pointed out that the observed approximate mass-independence of  $\langle p_t \rangle$  constrains the gluon  $x$  distribution: if the gluon  $x$  distribution is assumed to have the

form  $(1-x)^p/x$  then  $p$  must be in the range 4 through 7. It is evident that the transverse momentum behavior is, in principle, a sensitive test of the theory, but not at the present level of calculational ability. (A more clear-cut prediction<sup>17</sup> that the  $\langle p_t \rangle$  decreases sharply with increasing Feynman  $x$  has not been borne out by data<sup>75</sup> and is now also theoretically controversial. We have insufficiently broad  $x$  acceptance to address this question.) Evidently the complete understanding of lepton pair transverse momentum will have to await the solution of the problems of quark confinement and QCD at small momentum transfer.

#### 6. Quark-meson scattering

An alternative approach has been taken by Duong-van et al.<sup>18</sup> They apply the constituent interchange model (CIM) to massive lepton pair production, taking the basic subprocess to be quark-meson scattering (Figure 6) rather than quark-antiquark annihilation (though the latter mechanism is included in their model as a limiting case at  $p_t = 0$ ). Their predicted  $\langle p_t \rangle$  versus mass, which includes a contribution due to the intrinsic  $p_t$  of the initial-state quark and meson, agrees quite well with our data. The CIM has so far weathered all attempts to disprove it, but it remains less satisfying than a genuine field theory of the elementary constituents of matter such as QCD attempts to be.

#### C. Lepton Pairs and Single Leptons

There is still some mystery concerning the source of single

leptons in hadron collisions<sup>76</sup>. Above 1/2 GeV of  $p_t$  or so the lepton production cross-section is observed to be approximately  $10^{-4}$  of the pion cross-section over a wide range of collision energies. We have computed the contribution of lepton pair production to single lepton production by Monte Carlo integration over the momentum of the second lepton. Figure 46 shows the results, along with the pion production fit of Clark et al.<sup>77</sup> multiplied by  $10^{-4}$ . The  $J/\psi$  curve comes from Snyder et al.<sup>6</sup> (assuming the Gaussian form for the  $J/\psi$   $p_t$  distribution). The continuum model used was that of Kaplan et al.<sup>1</sup>, using the  $vW_2$  fit of Kirk<sup>72</sup> and a sea fit similar to the ones presented here. We integrated over masses from 4 to 24 GeV. For T production we assumed a Feynman  $x$  dependence given by

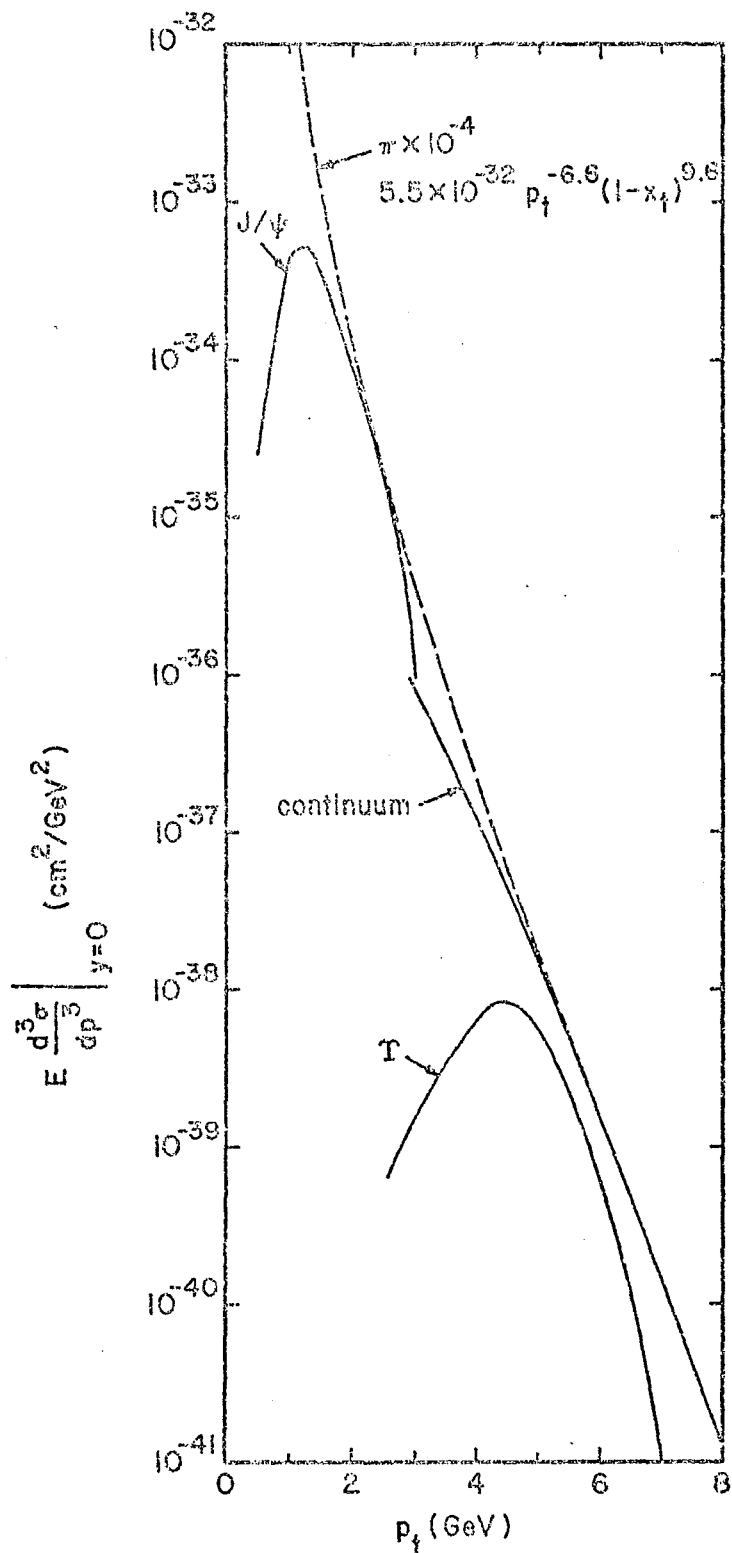
$$\frac{d\sigma}{dx} \propto (1-|x|)^{4.3}$$

as has been observed for the  $J/\psi$ <sup>75</sup>. The  $J/\psi$  is found to dominate out to  $p_t$  of 3 GeV, while the T contribution is small compared to that of the continuum. If single leptons are indeed represented by  $10^{-4}$  of pions at these large transverse momenta (measurements hardly go beyond  $p_t \approx 5$  GeV), then it is clear that a substantial fraction of single leptons at very large  $p_t$  originate as members of pairs.

#### D. Summary of Conclusions

1. We have measured the yield of massive muon pairs in 400 GeV





DIRECT LEPTONS FROM LEPTON PAIRS (solid lines)  
 COMPARED TO PIONS  $\times 10^{-4}$  (dashed line; from ref. 77)

FIGURE 46

proton-nucleon collisions with high statistical precision and good mass resolution. 24,000 events are observed in the range  $5 < m < 17$  GeV.

2. Measurements of the muon-pair cross-section with Be and Pt targets imply linear nucleon number dependence, consistent with parton model expectations.
3. We have measured the dependence of the cross-section on mass, transverse momentum, and rapidity within the range  $-0.28 < y < 0.26$ .
4. At least two new narrow resonances are observed in the mass range  $9 < m < 10.5$  GeV.
5. The dependence of the resonance cross-section on transverse momentum and rapidity is significantly different from that of the continuum, implying differing production mechanisms.
6. The most likely interpretation of the resonances is that they are bound states of a new, heavy charge  $-\frac{1}{3}$  quark with its antiquark.
7. The shape of the continuum can be accommodated in the parton annihilation model if steep antiquark  $x$  distributions like those of Feynman and Field are assumed.
8. The observed broad transverse momentum distributions can be accommodated in the parton model if QCD corrections are taken into account. The state of the theory does not yet permit incisive comparison with the available experimental data.
9. Massive lepton-pair production should provide a substantial signal of single leptons at very large transverse momentum ( $p_t > 4$  GeV).
10. The promise of Prof. Lederman's proposal<sup>27</sup> has been borne out.

## APPENDIX

### Mass Calibration

The mass calibration of our spectrometer depends on accurate knowledge of three things: positions of proportional chambers, strength of the field in the air gap magnets, and energy loss in the hadron absorber. Careful measurements permitted us to calibrate the spectrometer to an estimated accuracy of  $\pm 1\%$  (r.m.s.), but the final calibration was derived from measurements of the  $J/\psi$  and T masses in  $e^+e^-$  annihilation experiments. Details of the calibration are given below.

#### A. Alignment

In the plane of magnetic deflection, the chambers were aligned with the target using the alignment runs. Deflection angle measurements are accurate to better than 0.06 mrad (r.m.s.), which corresponds to 0.35% in momentum at the mass of the T where typical momenta are 70 GeV. However, since both charges of muon are accepted in each arm, this error cancels to first order and represents a negligible contribution to the absolute mass error.

The separation of the arms in the horizontal plane was measured to 0.25" accuracy. The opening angle measurement is thus accurate to  $<0.1\%$ .

#### B. Magnet Calibration

The line integral of the field was measured as a function of magnet current and x and y position using a 15'-long flip coil.

Saturation between 1000A where we observe the  $J/\psi$  and 1500A where we observe the  $T$  was found to be 0.9%. These measurements should be accurate to  $<0.2\%$ . The variation of the field integral with horizontal and vertical position is given by

$$\int \vec{B} \cdot d\vec{l} = \left[ 1 + 0.00012 (x^2 - 2y^2) \right] \int \vec{B}_0 \cdot d\vec{l}$$

where  $\int \vec{B}_0 \cdot d\vec{l}$  is the line integral of the field along the center of the aperture ( $x=y=0$ ). The aperture is 20" wide by 10" high half way through the magnet, thus the maximum excursion of the field integral from its central value is  $\pm 1\%$ . The coefficient 0.00012 was determined by requiring the observed mass of the  $J/\psi$  to be independent of track position in the magnet, since flip coil measurements in extreme positions were difficult to make. The coefficient is not well determined and could vary by  $\pm 50\%$ . A 50% variation would have  $< 0.2\%$  effect on the mass of the  $T$  and perhaps somewhat more effect on the mass of the  $J/\psi$ , since  $J/\psi$  events at 1000A tend to have muons closer to the inside edge of the aperture than  $T$  events at 1500A.

### C. Energy Loss

The muons pass through the materials described in Table III and Section II.C.6 before their momentum is measured. The correction to the measured momentum is based on the calculations of Sternheimer<sup>78</sup> for the most probable energy loss in these

materials. We measured the energy loss of pions in beryllium at 10 and 50 GeV momentum. The result was 10% larger than Sternheimer's calculation,<sup>79</sup> therefore we have used Sternheimer's results increased by 10% for all materials. It is not clear whether the calculation or the measurement is more reliable. Since the energy loss is 2.8 GeV, this is a 0.4% uncertainty in the mass of the T.

#### D. Observed Masses and Calibration Adjustment

The above calibration yielded an T mass of 9.51 GeV and a J/ $\psi$  mass of 3.112 GeV. If the J/ $\psi$  mass is actually 3.097 GeV then this is 0.5% too high. If this discrepancy is attributable to magnetic field or opening angle then the T mass is also 0.5% too high. If it is attributable to energy loss then the T mass is only 0.17% high. If the magnet saturation were only 0.5% instead of 0.9% then the observed T mass would be correct. Prior to the observation of the T at DESY, our best estimate of its mass was  $9.45 \text{ GeV} \pm 1\%$  taking these considerations into account. When the DESY experimenters announced their observed mass of  $9.46 \pm 0.01 \text{ GeV}$ , we adjusted the magnetic field calibration to agree with this value.

## REFERENCES

1. S.W. Herb, D.C. Hom, L.M. Lederman, J.C. Sens, H.D. Snyder, J.K. Yoh, J.A. Appel, B.C. Brown, C.N. Brown, W.R. Innes, K. Ueno, T. Yamanouchi, A.S. Ito, H. Jöstlein, D.M. Kaplan, R.D. Kephart, Phys. Rev. Lett. 39, 252 (1977).  
  
W.R. Innes, J.A. Appel, B.C. Brown, C.N. Brown, K. Ueno, T. Yamanouchi, S.W. Herb, D.C. Hom, L.M. Lederman, J.C. Sens, H.D. Snyder, J.K. Yoh, R.J. Fisk, A.S. Ito, H. Jöstlein, D.M. Kaplan, R.D. Kephart, Phys. Rev. Lett. 39, 1240 (1977).  
  
D.M. Kaplan, R.J. Fisk, A.S. Ito, H. Jöstlein, J.A. Appel, B.C. Brown, C.N. Brown, W.R. Innes, R.D. Kephart, K. Ueno, T. Yamanouchi, S.W. Herb, D.C. Hom, L.M. Lederman, J.C. Sens, H.D. Snyder, J.K. Yoh, Phys. Rev. Lett. 40, 435 (1977).  
  
J.K. Yoh, S.W. Herb, D.C. Hom, L.M. Lederman, J.C. Sens, H.D. Snyder, K. Ueno, B.C. Brown, C.N. Brown, W.R. Innes, R.D. Kephart, T. Yamanouchi, R.J. Fisk, A.S. Ito, H. Jöstlein, D.M. Kaplan, Phys. Rev. Lett. 41, 684 (1978).
2. J.H. Christenson, G.S. Hicks, L.M. Lederman, P.J. Limon, B.G. Pope, E. Zavattini, Phys. Rev. D8, 2016 (1973).
3. S.D. Drell, T.-M. Yan, Phys. Rev. Lett. 25, 316 (1970); Ann. Phys. 66, 578 (1971).
4. J.J. Aubert, U. Becker, P.J. Biggs, J. Burger, M. Chen, G. Everhart, P. Goldhagen, J. Leong, T. McCorriston, T. G. Rhoades, M. Rhode, S.C.C. Ting, S.L. Wu, Y.Y. Lee, Phys. Rev. Lett. 33, 1404 (1974).
5. J.E. Augustin, A.M. Boyarski, M. Breidenbach, F. Bulos, J.T. Dakin, G.J. Feldman, G.E. Fischer, D. Fryberger, G. Hanson, B. Jean-Marie, R.R. Larsen, V. Luth, H.L. Lynch, D. Lyon, C.C. Morehouse, J.M. Paterson, M.L. Perl, B. Richter, P. Rapidis, R.F. Schwitters, W. M. Tanenbaum, F. Vannucci, G.S. Abrams, D. Briggs, W. Chinowsky, C.E. Friedberg, G. Goldhaber, R.J. Hollebeek, J.A. Kadyk, B. Lulu, F. Pierre, G.H. Trilling, J.S. Whitaker, J. Wiss, J.E. Zipse, Phys. Rev. Lett. 33, 1406 (1974).
6. D.C. Hom, L.M. Lederman, H.P. Paar, H.D. Snyder, J.M. Weiss, J.K. Yoh, J.A. Appel, B.C. Brown, C.N. Brown, W.R. Innes, T. Yamanouchi, D.M. Kaplan, Phys. Rev. Lett. 36, 1236 (1976).

- H.D. Snyder, D.C. Hom, L.M. Lederman, H.P. Paar, J.M. Weiss, J.K. Yoh, J.A. Appel, B.C. Brown, C.N. Brown, W.R. Innes, T. Yamanouchi, D.M. Kaplan, Phys. Rev. Lett. 36, 1415 (1976).
- B.C. Brown, J.A. Appel, C.N. Brown, W.R. Innes, T. Yamanouchi, R.J. Engelmann, R.J. Fisk, H. Jöstlein, D.M. Kaplan, R.D. Kephart, R.L. McCarthy, D.C. Hom, L.M. Lederman, H.P. Paar, H.D. Snyder, J.M. Weiss, J.K. Yoh, "Study of J/psi (3100) and Psi' (3700) Production in Proton-Nucleon Collisions with Electron and Muon Pairs," FERMILAB-PUB-77/54-EXP (1977).
7. D.C. Hom, L.M. Lederman, H.P. Paar, H.D. Snyder, J.M. Weiss, J.K. Yoh, J.A. Appel, B.C. Brown, C.N. Brown, W.R. Innes, T. Yamanouchi, R.J. Engelmann, R.J. Fisk, H. Jöstlein, D.M. Kaplan, R.D. Kephart, R.L. McCarthy, Phys. Rev. Lett. 37, 1374 (1976). The anomalously large mean transverse momenta ( $\langle p_t \rangle = 1.5$  GeV) reported in this reference reflect the choice of fitting function. The data are in agreement with those presented here.
  8. L. Kluberg, P.A. Piroue, R.L. Sumner, D. Antreasyan, J.W. Cronin, H.J. Frisch, M.J. Shochet, Phys. Rev. Lett. 37, 1451 (1976).
  9. K. J. Anderson, G.G. Henry, K.T. McDonald, J.E. Pilcher, E.I. Rosenberg, J.G. Branson, G.H. Sanders, A.J.S. Smith, J.J. Thaler, Phys. Rev. Lett. 36, 237 (1976); Phys. Rev. Lett. 37, 799 (1976).  
  
J.G. Branson, G.H. Sanders, A.J.S. Smith, J.J. Thaler, K.J. Anderson, G.G. Henry, K.T. McDonald, J.E. Pilcher, E.I. Rosenberg, Phys. Rev. Lett. 38, 1331 (1977); Phys. Rev. Lett. 38, 1334 (1977).
  10. B. Knapp, W. Lee, P. Leung, S.D. Smith, A. Wijangco, J. Knauer, D. Yount, D. Nease, J. Bronstein, R. Coleman, L. Cornell, G. Gladding, M. Gormley, R. Messner, T. O'Halloran, J. Sarracino, A. Wattenburg, D. Wheeler, M. Binkley, R. Orr, J. Peoples, A.L. Read, Phys. Rev. Lett. 34, 1040 (1975); Phys. Rev. Lett. 34, 1044 (1975).  
  
M. Binkley, I. Gaines, J. Peoples, B. Knapp, W. Lee, P. Leung, S.D. Smith, A. Wijangco, J. Knauer, J. Bronstein, R. Coleman, G. Gladding, M. Goodman, M. Gormley, R. Messner, T. O'Halloran, J. Sarracino, A. Wattenburg, Phys. Rev. Lett. 37, 574 (1976).
  11. R. P. Feynman, Phys. Rev. Lett. 23, 1415 (1969); Proceedings of the Third International Conference on High Energy Collisions at Stony Brook, Gordon and Breach Science Publishers, Inc., New York, 1969, p. 237.

12. J.D. Bjorken, Phys. Rev. 179, 1547 (1969).
13. G. Miller, E.D. Bloom, G. Buschhorn, D.H. Coward, H.DeStaebler, J. Drees, C.L. Jordan, L.W. Mo, R.E. Taylor, J.I. Friedman, G.C. Hartmann, H.W. Kendall, R. Verdier, Phys. Rev. D5, 528 (1972).
14. S.M. Berman, J.D. Bjorken, J.B. Kogut, Phys. Rev. D4, 3388 (1971).  
J. Kuti, V.F. Weisskopf, Phys. Rev. D4, 3418 (1971).

These two earliest papers preceded most of the data and used almost entirely theoretical input. Of the many authors who have since addressed this problem, a representative sample is:

- H.P. Paar, E.A. Paschos, Phys. Rev. D10, 1502 (1974).
- V. Barger, R.J.N. Phillips, Nucl. Phys. B73, 269 (1974).
- G.R. Farrar, Nucl. Phys. B77, 429 (1974).
- R. McElhaney, S.F. Tuan, Phys. Rev. D8, 2267 (1973).
- G. Altarelli, N. Cabibbo, L. Maiani, R. Petronzio, Nucl. Phys. B69, 531 (1974).
- S. Pakvasa, D. Parashar, S.F. Tuan, Phys. Rev. D10, 2124 (1974).
15. D.H. Perkins, Contemp. Phys. 16, 173 (1975).
16. C. Chang, K.W. Chen, D.J. Fox, A. Kotlewski, P.F. Kunz, L.N. Hand, S. Herb, A. Russell, Y. Watanabe, S.C. Loken, M. Strovink, W. Vernon, Phys. Rev. Lett. 35, 901 (1975).
17. For recent reviews see F. Halzen, D.M. Scott, "Hadroproduction of Photons and Leptons," University of Wisconsin preprint COO-881-21 (1978); and  
E.L. Berger, "Massive Lepton Pair Production in Hadronic Collisions, Vanderbilt Conference, 1978, p. 178.
18. M. Duong-van, K.V. Vasavada, R. Blankenbecler, Phys. Rev. D16, 1389 (1977).  
M. Duong-van, R. Blankenbecler, "Production of Massive Lepton Pairs," SLAC-PUB-2017 (1977).
19. S. Weinberg, Phys. Rev. Lett. 19, 1264 (1967); Phys. Rev. Lett. 27, 1688 (1971).



20. T.D. Lee, G.C. Wick, Phys. Rev. D2, 1033 (1970).
21. P.W. Higgs, Phys. Lett. 12, 132 (1964); Phys. Rev. Lett. 13, 508 (1964); Phys. Rev. 145, 1156 (1966).
22. T. Appelquist, H.D. Politzer, Phys. Rev. Lett. 34, 43 (1975).  
 A. DeRujula, S.L. Glashow, Phys. Rev. Lett. 34, 46 (1975).  
 T. Appelquist, A. DeRujula, H.D. Politzer, S.L. Glashow, Phys. Rev. Lett. 34, 365 (1975).  
 E. Eichten, K. Gottfried, T. Kinoshita, J. Kogut, K.D. Lane, T.-M. Yan, Phys. Rev. 34, 369 (1975).  
 A recent review can be found in F.J. Gilman, "Hadron Spectroscopy and the New Particles," SLAC-PUB-2065 (1977).
23. J.D. Bjorken, S.L. Glashow, Phys. Lett. 11, 255 (1964).
24. S.L. Glashow, J. Iliopoulos, L. Maiani, Phys. Rev. D2, 1285 (1970).
25. H. Harari, Comm. Nucl. Part. Phys. 6, 123 (1976).
26. R.M. Barnett, "A Review of Models with More Than Four Quarks," FERMILAB-Conf-75/71-THY (1975).
27. NAL Proposal #288 (1974).
28. R.J. Fisk, Ph.D. thesis, State University of New York at Stony Brook (1978).
29. V.L. Highland, Nucl. Instr. Meth. 129, 497 (1975).
30. Y.-S. Tsai, Rev. Mod. Phys. 46, 815 (1974).
31. "A Modular Instrumentation System for Data Handling," U.S. Atomic Energy Commission report TID-25875 (1972).  
 "Organization of Multi-Crate Systems," U.S. Atomic Energy Commission report TID-25876 (1972).
32. This value was measured at Brookhaven National Laboratory by J. Hudis et al., Phys. Rev. 129, 434 (1963). A recent measurement at Fermilab by S. Baker et al. (unpublished) yielded 3.8 mb. If this new number were used, our cross-sections would increase by 9%. In order to maintain continuity with earlier Fermilab experiments we have used the BNL cross-section.

33. P.A. Piroue and J.S. Smith, Phys. Rev. 148, 1315 (1966).
34. J.W. Cronin, H.J. Frisch, M.J. Shochet, J.P. Boymond,  
P.A. Pirone, R.L. Sumner, Phys. Rev. D11, 3105 (1975).  
L. Kluberg, P.A. Pirone, R.L. Sumner, D. Antreasyan,  
J.W. Cronin, H.J. Frisch, M.J. Shochet, Phys. Rev. Lett.  
38, 670 (1977).
35. R.L. McCarthy, R.J. Engelmann, R.J. Fisk, M.L. Good, A.S. Ito,  
H. Jöstlein, D.M. Kaplan, R.D. Kephart, H. Wahl, S.W. Herb,  
D.C. Hom, L.M. Lederman, J.C. Sens, H.D. Snyder, J.K. Yoh,  
J.A. Appel, B.C. Brown, C.M. Brown, W.R. Innes, K. Ueno,  
Phys. Rev. Lett. 40, 984 (1978).
36. E.L. Berger, J.T. Donohue, S. Wolfram, Phys. Rev. D17,  
858 (1978).
37. A. Soni, Phys. Rev. D8, 2264 (1973).
38. L.M. Lederman, "Lepton Pair Production in Hadronic Collisions,"  
Cargèse Summer Institute, July 1977.
39. For a review see A.S. Ito, "Review of the Upsilon," International  
Conference on Neutrino Physics and Neutrino Astrophysics, Purdue, 1978.
40. J.K. Yoh et al., op. cit. Ref. 1.
41. J. Orear, A.H. Rosenfeld, R.A. Schluter, Nuclear Physics,  
University of Chicago Press, 1950, p. 159.
42. A. deShalit, H. Feshbach, Theoretical Nuclear Physics,  
Vol. I: Nuclear Structure, Wiley, 1974, p. 115.
43. Isotropic delay has been observed for the  $J/\psi$  by J.G. Branson  
et al., Phys. Rev. Lett. 38, 1331 (1977).
44. Ch. Berger et al., Phys. Lett. 76B, 243 (1978).  
C.W. Darden et al., Phys. Lett. 76B, 246 (1978).
45. G. Flugge, XIX International Conference on High Energy Physics,  
Tokyo, 1978.
46. S. Weinberg, Rev. Mod. Phys. 46, 255 (1974).  
J.C. Pati, S. Rajpoot, A. Salam, Phys. Lett. 71B, 387 (1977).
47. R.W. Brown, K.O. Mikaelian, M.K. Galliard, Nucl. Phys. B75,  
112 (1974).

- H.S. Mani, J.C. Pati, S. Rajpoot, A.Salam, Phys. Lett. 72B, 75 (1977).
48. J. Ellis, M.K. Gaillard, D.V. Nanopoulos, Nucl. Phys. B106, 292 (1976).
49. H.D. Snyder, Ph. D. Thesis, Nevis Laboratories, Columbia University, 1979.
50. J.H. Cobb et al., Phys. Lett. 72B, 273 (1977).  
CCOR group, L.M. Lederman, private communication.
51. A review of the status of the quarkonium model as applied to both  $\psi$  and  $T$  families was given by K. Gottfried, Proc. International Symposium on Lepton and Photon Interactions at High Energies, Hamburg, Germany, 1977, p. 667.
52. E. Eichten, K. Gottfried, Phys. Lett. 66B, 286 (1977).
53. R.N. Cahn, S.D. Ellis, Phys. Rev. D16, 1484 (1977).  
P.B. James, "Expectations for Heavy Vector Meson Production in  $e^+e^-$  Annihilation," University of Missouri preprint (1976).
54. J. Ellis, M.K. Gaillard, D.V. Nanopoulos, S. Rudaz, Nucl. Phys. B131, 285 (1977).  
C.E. Carlson, R. Suaya, Phys. Rev. Lett. 39, 908 (1977).  
T. Hagiwara, Y. Kazama, E. Takasugi, Phys. Rev. Lett. 40, 76 (1978).  
F. Halzen, S. Matsuda, CERN Report No. TH-2354 (1977).  
D.B. Lichtenberg, J.G. Wills, J.T. Kiehl, Phys. Rev. Lett. 39, 1592 (1977).  
R.M. Barnett, European Conference on Particle Physics, Budapest, 1977.
55. C. Quigg, J.L. Rosner, Phys. Lett. 72B, 462 (1978).
56. C. Quigg, J.L. Rosner, Phys. Lett. 71B, 153 (1977).
57. H.B. Thacker, C. Quigg, J.L. Rosner, Fermilab-Pub-77/108-THY (1977); Fermilab-Pub-77/109 THY (1977).  
W. Celmaster, H. Georgi, M. Machacek, Phys. Rev. D17, 879 (1978); ibid, 886 (1978).

- W. Celmaster, F.S. Henyey, "The Quark-Antiquark Interaction at all Momentum Transfers," UCSD preprint No. 10P10-191 (1978).
- B. Margolis, R. Roskies, N. DeTakacsy, "Potential Models for Heavy Quarks and Asymptotic Freedom," IV European Antiproton Conference, Barr, France, June 1978.
- P. Ditsas, N.A. McDougall, R.G. Moorhouse, "Quarkonia from Charmonium and Renormalization Group Equations," University of Glasgow preprint (1978).
- P. Dignon, C.A. Piketty, Phys. Lett. 74B, 108 (1978).
58. S. Okubo, Phys. Lett. 5, 165 (1963).  
 G. Zweig, CERN report No. 8419/Th 412 (1964).  
 J. Iizuka, Prog. Theor. Phys. Suppl. No. 37-38, 21 (1966).
59. K. Ueno et al., "Properties of Proton Production of the T Family and Evidence for the T," submitted to Phys. Rev. Lett. (1978).
60. C.W. Darden et al., "Evidence for a Narrow Resonance at 10.01 GeV in Electron-Positron Annihilations," DESY preprint 78/44 (1978).  
 J.K. Bienlein et al., "Observation of a Narrow Resonance at 10.02 GeV in  $e^+e^-$  Annihilations," DESY preprint 78/45 (1978).
61. M. Kobayashi, T. Maskawa, Prog. Theor. Phys. 49, 652 (1973).
62. A.K. Mann, "New Vistas in Neutrino Physics," Orbis Scientiae 1976, Coral Gables, Florida, and references therein.
63. F. Eiselle, "Results of the CERN-Dortmund-Heidelberg-Saclay Neutrino Counter Experiment," Proc. SLAC Summer Institute on Particle Physics, 1977, p. 465.
64. M.L. Perl, "Comments on the  $\tau$  Heavy Lepton," V International Conference on Experimental Meson Spectroscopy, Northeastern University, Boston, Mass., 1977.  
 R. Brandelik et al., Phys. Lett. 73B, 109 (1978).
65. C.E. Carlson, R. Suaya, Phys. Rev. D14, 3115 (1976); Phys. Rev. D15, 1416 (1977); op. cit. ref. 54.  
 S.D. Ellis, M.B. Einhorn, C. Quigg, Phys. Rev. Lett. 36, 1263 (1976).
66. H.I. Miettinen, "Strong Interactions of Partons, Lecture III," Fermilab Academic Lecture Series, 1978.

67. B.C. Brown et al., op. cit. Ref. 6.
68. J.H. Cobb et al., Phys. Lett. 72B, 497 (1978).
69. H.D. Politzer, Nucl. Phys. B129, 301 (1977).
70. H. Georgi, Phys. Rev. D17, 3010 (1978).
71. K. Kajantie, R. Raitio, University of Helsinki preprint No. HU-TFT-77-21 (1977).  
C.S. Lam, T.M. Yan, Phys. Lett. 71B, 173 (1977).  
H. Fritzsch, P. Minkowski, Phys. Lett. 73B, 80 (1978).  
C.T. Sachrajda, Phys. Lett. 73B, 185 (1978).  
P. Kreiss, K. Schilcher, Phys. Lett. 74B, 243 (1978).  
K. Kajantie, J. Lindfors, R. Raitio, Phys. Lett. 74B, 384 (1978).  
G. Altarelli, G. Parisi, R. Petronzio, Phys. Lett. 76B, 356 (1978).  
J. Kubar-Audre, F.E. Paige, "Transverse Momentum of Lepton Pairs and Scaling Violations in Deep Inelastic Scattering," BNL preprint No. BNL-23530 (1978).  
E.L. Berger, "Tests of QCD in the Hadroproduction of Massive Lepton Pairs," ANL preprint No. ANL-HEP-PR-78-18 (1978).  
R.C. Hwa, "Recent Theoretical Developments in Lepton Pair Production," IX International Symposium on High Energy Multiparticle Dynamics, Tabor, Czechoslovakia, July 1978.  
S. Matsuda, "Parton Transverse Momenta," XIX International Conference on High Energy Physics, Tokyo, Japan, August 1978.  
R.C. Hwa, J. Wosiek, "Nonfactorizability of Inclusive Distributions in Perturbative QCD," Rutherford preprint No. RL-78-079 (1978).
72. T. Kirk, Fermilab internal memo TM-791-2000.0 (1978). We used the fit for  $Q^2 > 2$ .
73. W.B. Atwood, "Electron Scattering off Hydrogen and Deuterium at 50° and 60°" (Ph.D. Thesis), SLAC Report-185 (1975).
74. R.D. Field, R.P. Feynman, Phys. Rev. D15, 2590 (1977).
75. K. J. Anderson et al., "Hadronic Production of High-Mass Muon Pairs and the Measurement of the Pion Structure Function," XIX International Conference on High Energy Physics, Tokyo, Japan, 1978.

76. L.M. Lederman, "Lepton Production in Hadron Collisions," Proc. Int. Symp. on Lepton and Photon Interactions at High Energies, SLAC, 1975, p. 265.  
J.W. Cronin, "Hadron Induced Leptons and Photons," Proc. Int. Symp. on Lepton and Photon Interactions at High Energies, Hamburg, Germany, 1977, p. 579.
77. A.G. Clark et al., "Inclusive  $\pi^0$  Production from High Energy p-p Collisions at Very Large Transverse Momenta," CERN preprint (1978).
78. R.M. Sternheimer, Phys. Rev. 115, 137 (1959); R.M. Sternheimer, R.F. Peierls, Phys. Rev. B3, 3681 (1971).
79. C.N. Brown, T. Yamanouchi, private communication.